Seismic signatures of siliciclastic reservoirs as function of burial history – a Barents Sea example

Master thesis

Petter Næss Guldbrandsøy

Department of Earth Science

University of Bergen

Bergen, June 2017

Abstract

The Barents Sea is one of the most exciting areas regarding oil and gas exploration at the Norwegian Continental Shelf. Compared to the North Sea the area has a complex burial history, making the exploration challenging. One major challenge is the understanding of elastic properties and the coherent seismic signatures during the history. In this study, the seismic signatures are discussed. To be able to do this it is first necessary to establish a good geological model, and then use different rock physics models to look at elastic properties at various stages during history.

A published geological burial history for the Bjarmeland Platform is extended and used as a reference for the rock physics modeling. Different rock physics models have been used to predict the elastic properties for changes in pressures, temperatures, and for cementation and formation of cracks during the burial and uplift. Also, a fluid substitution model is used to predict saturation effects. The amplitude versus offset (AVO) modeling is done using simplistic methods for AVO-intercept and -gradient, based on the rock physics modeling.

The study shows that the major changes in elastic properties during a burial history are caused by cementation and fluid substitution. There are several minor changes as well, like increased pressure, temperature and uplift. Still, they are insignificant compared to the cementation and fluid substitution. Therefore, the most important part of the burial history, in this study, is the maximum burial depth in combination with the geothermal gradient. These components are important to understand if the reservoir has been cemented in the chemical compaction domain at some point in the history.

Seismic attributes are discussed using the calculated gradient and intercept for the elastic properties at various stages in the burial history. It is shown that the biggest changes in AVO are caused by the cementation and fluid substitution. Also, it has been demonstrated how cracks move the AVO-response in the opposite direction of the burial/cementation trend.

This study demonstrates how rock physics modeling can be used as a valuable tool for prospect risking and uplift estimates, especially in areas with a complex burial history. This is because the modeling can predict seismic signatures, solely based on a good geological burial history.

Acknowledgments

First, I want to thank Prof. Tor Arne Johansen and Dr. Erling Hugo Jensen for their excellent supervision, guidance, and encouragement during two years. The two last years have been very educational.

I also want to thank Ph.D. student Ronny Tømmerbakke and researcher Åsmund Drottning for much-appreciated help and time.

My fellow students deserve big thanks as well for making the time at University joyful, and I have made so many new friends. Thank you.

Finally, I want to thank my family and girlfriend Ingrid for always having my back and being a valuable support.

Table of Contents

Chapter 1: Introduction

1.1 Introduction

On a global scale, there are fewer oil and gas discoveries each year. To meet the world's increasing demand for oil and gas (Holditch and Chianelli, 2008), one needs to search for hydrocarbons in more complex and remote areas, and take a new look at older areas with new technology. Recent discoveries as Brasse and Snøhvit shows that it is still possible to make huge oil and gas discoveries in both old and new exploration areas. New and better interpretations are needed, and one vital area is the quantitative seismic interpretation. This field of expertise is important for exploration of hydrocarbons and might contribute to even more exploration success in the future.

A geophysicist's job is among other things to define reservoir rock properties; connecting seismic, well logs, cores, etc., with the goal to understand a reservoir as best as possible for the smallest cost possible. Therefore, it is important to develop the understanding and techniques of quantitative interpretation to achieve the goal of higher drilling success.

The quality of the reservoir is a vital part of the prospect evaluation and the focus of this thesis. The goal is to see how a sandstone reservoir changes during burial using a combination of burial history and rock physic modeling, and using AVO-modelling to see how the seismic signatures changes.

In this thesis, the reservoir rock properties are investigated for the burial history of the Stø formation in the Barents Sea. The two wells used as a reference is the Apollo well (7324/2-1) and the Atlantis well (7325/1-1).

1.2 The Barents Sea – the exploration history

The Barents Sea covers an area of approximately 1.3 million km^2 and is located north of Norway. The average depth in the area is about 230 meters (Loeng, 1991). The burial history is very complicated, and consists of several basins and highs (Henriksen et al., 2011b), see Figure 1.2. The exploration history of the Norwegian Barents Sea started in 1979. Then, it only took a year before the first well was drilled. The interest for the Barents Sea increased and was high until 1986. From 1986, most of the wells being drilled contained tiny amounts of gas or

brine. It led to a stop in further drilling between 1994-2000. In 2006, the situation was changed due to the oil discovery in the Goliat field. After this, there have been several significant discoveries; Wisting, Gotha, Alta, etc. Today the Barents Sea is more exciting than ever due to ever better quantitative seismic interpretation methods (NPD, 2017).

In the Norwegian Barents Sea, one of three wells has been discoveries. The problem is that many of the reservoirs only contain minor amounts of gas – so the typical structures are dry, having non-producible gas and residual oil saturation. One of the reasons for these non-producible wells is that many traps and cap rocks in the area have leaked at some point, and after the leakage, they have been refilled with small amounts of gas (Ohm et al., 2008).

1.3 Hoop fault complex – Apollo and Atlantis prospects.

The first well, 7324/2-1, is located at the Hoop fault complex (block 7324/7), see Figure 1.1. The primary goal for this well was to prove hydrocarbons in the Stø and Snadd formations. Statoil Petroleum AS started drilling the well 01.06.2014 and ended 18.06.2016. The well was drilled vertically down to 1050 meter below the sea surface (the ocean depth is 443 meters). The Stø formation was encountered at 849 meters and was proven to be good reservoir quality, but water saturated. The deeper Snadd Formation had some oil between 893 and 929 meters. The well was permanently plugged and left as a dry well (NPD, 2016a).

The second well, 7325/1-1, located at the Hoop fault complex as well (Figure 1.1). This well was drilled by Statoil Petroleum AS from 23.06.2014 to 21.07.2014 to investigate the possibility for hydrocarbons in the Kobbe formation, and deeper located Snadd- and Klappmyss formations. The Kobbe formation had traces of hydrocarbons, but the reservoir quality was poor. Snadd formation contained 55 meters of reservoir formation, where the top 10 meters where gas saturated. The well was drilled down at 2865 meter below the sea surface, and the ocean depth in the area is 487 meters. 21th of July 2014 it was left as a technical gas discovery (NPD, 2016b).

Both wells are drilled in PL615, see Figure 1.1C.

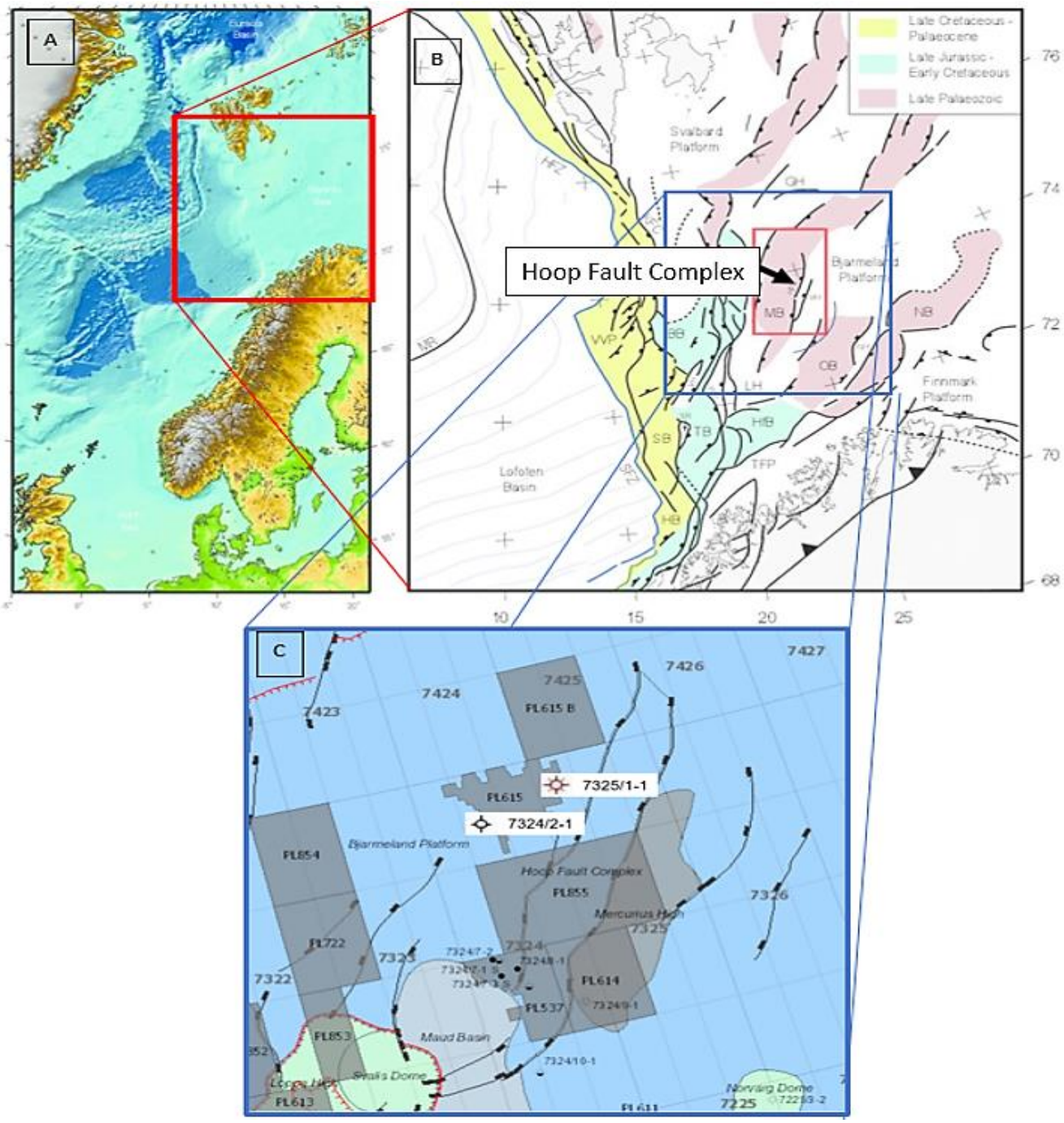

Figure 1.1 - Figure A and B is modified from Gabrielsen et al. (2016), and displays the location of the Hoop Fault complex. Figure C shows where well 7324/2-1 and 7325/1-1 is in the Barents Sea.

1.4 Research Objectives

The research objective of this thesis is to investigate how rock properties and seismic signatures in a sandstone reservoir changes during a burial history. In this study, an example from the Barents Sea is used as burial history. The Stø formation in the Barents Sea is used as the reference reservoir due to it excellent reservoir quality. The burial history in the Barents Sea is complicated, and the reservoirs might have been uplifted and compacted both mechanically and chemically since deposition.

For the calculation of rock properties, the burial history is divided into stages; each associated with a representative rock physics model. This also demonstrates how the burial history can be integrated into a prediction of the effective rock properties as they are observed today. AVO modeling will be done for each stage, to study and compare the seismic responses. This is done trying to understand how seismic signatures should behave during a burial history and might be applied to hydrocarbon exploration in remote areas with no or few wells.

Uncertainties and limitations of the models and results are discussed.

1.5 Database and methodology

The database for this study is datasets from the 7324/2-1 well (Apollo) and the 7325/1-1 well (Atlantis). The 7325/1-1 well has a proximity to the Apollo well, but due to the deeper targets, it has a less prominent role in this thesis. The wells are used for the uplift estimations, and the Apollo well is used as a reference well for the AVO and rock physics modeling of the in-situ period.

The rock physics and AVO modeling is done using different scripts in the MATLAB software.

A detailed description of methods and data used is given in chapter 3 and 4.

1.6 Description of chapters

The second chapter takes a closer look at the geological setting and burial history in the Barents Sea. It will also give a review of the petroleum system, an introduction to the relevant formations for the thesis and some of the exploration challenges in the area.

The third chapter presents the research methodologies and theoretical background for the burial history estimations, rock physics modeling and AVO-modelling.

The fourth chapter describes the application of the theories for the various modeling, and the database used. The chapter is divided into three sub-chapter; burial and uplift, rock physics modeling and AVO-modeling.

The results of the modeling are given in chapter five, and the discussion in chapter 6; both divided into the same three sub-chapters.

The most important conclusions are given in the summary in chapter 7.

Chapter 2: Geological settings in the Barents Sea

2.1 Structures and tectonic in the Norwegian Barents Sea

The Barents Sea covers an area of 1,3 million km^2 and has an average depth of 230 m (Loeng, 1991). The Barents Sea is one of the largest continental shelves on earth. The Norwegian part of the Barents Sea covers approximately 230.000 km^2, that is an area 1.5 times bigger than the Norwegian sector of the North Sea. At a global scale, there are several known petroleum basins in the same polar area as the Barents Sea – for example in Artic Canada, Alaska and Siberian (Doré, 1995). Also, there are several discoveries the last years (Snøhvit, Goliat and Wisting) in the Barents Sea confirming that the Norwegian Barents Sea has a great potential for hydrocarbons (NPD, 2017). The Norwegian Petroleum Directorate estimated that the undiscovered resources in the Barents Sea are almost 65 % of the total undiscovered resources on the Norwegian shelf (NPD, 2017).

Doré (1995) describes the Barents Sea as a "complex mosaic of platform areas and basins", formed by two major continental collisions and subsequently separated by continental separation. Since the first of the two collisions happened approximately 400 million years ago during the Caledonian orogeny, it has been affected by several phases of tectonic. These periods of stretching and compression in the area have made it to what it is today - a complex area of rift basins, platforms and structural highs as seen in Figure 2.1 (Johansen et al., 1992).

The Stø formation in the Barents Sea was deposited between Late Pliensbachian to Bajocian (approximately 190 Ma years ago), with a dominating lithology of mature and well-sorted sandstones (NPD, 2014). These sands were deposited in prograding coastal regimes, and have shale and siltstone intervals in the upper parts. During this period, the Barents Sea was a wide-ranging and shallow epicontinental basin (Glørstad-Clark et al., 2011). After the deposition, the Stø formation has experienced several burial and uplift events.

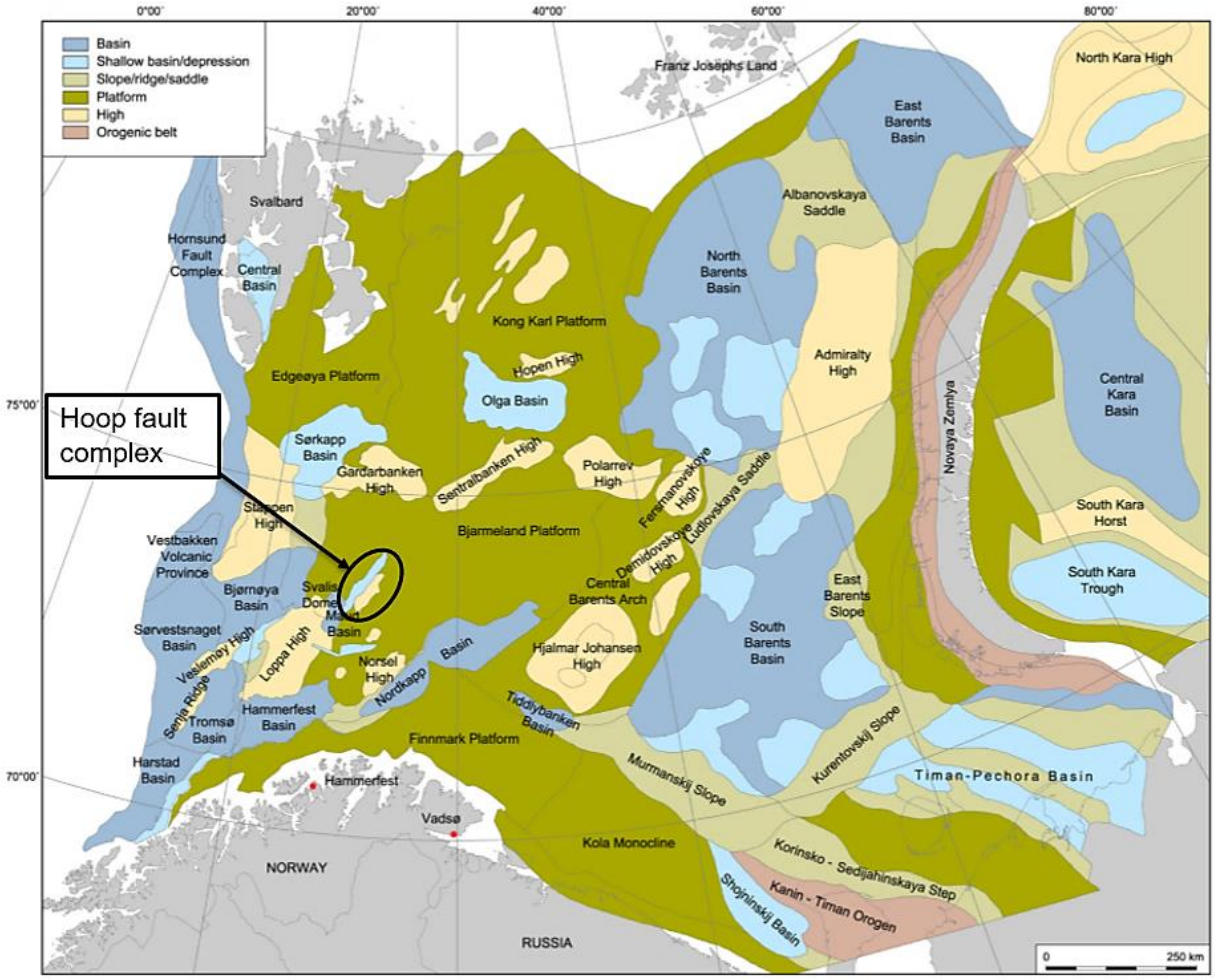

Figure 2.1 – The figure shows the structural elements in the Barents Sea, with basins, platforms and highs. The Hoop Area is marked with a circle (modified from Henriksen et al. (2011b)).

2.2 Hoop Fault Complex

Hoop fault complex is characterized by normal faults and is assumed to be a weakness zone. The Central Fault Complex was in Late Carboniferous to Permian time linked to the subsidence of Maud Basin. This created fault blocks and controlled the sedimentation pattern in the period, and these faults are what's been reactivated in later times (Gabrielsen et al., 2010).

Hoop Fault Complex cuts through the Bjarmeland (North) and the Loppa high (south), and according to Gabrielsen et al. (2010), the region can be divided into three parts; Northern part, Central part and Southern part. The Northern part consists of a large group of normal faults cutting the Bjarmeland Platform. The central part relates to the development of the Svalis dome and the subsidence of Maud basin. The southern part of the Complex is a narrow graben on the Loppa High (Gabrielsen et al., 1990).

2.3 Petroleum systems and exploration in the Barents Sea

"A petroleum system is a geologic system that encompasses the hydrocarbon source rock and all related oil and gas and which includes all of the geologic elements and processes that are essential if a hydrocarbon accumulation is to exist" (Magoon and Dow, 1994).

Having a well-functioning petroleum system is dependent on several factors that need to be in place at the right time. The source rock needs correct temperature and pressure, and the migration routes need to transport the hydrocarbons into a reservoir. The reservoir requires porosity and permeability to store hydrocarbons. On top of the reservoir, an impermeable rock is needed to prevent the hydrocarbons from further migration. Also, a trap is required (structural or stratigraphic) that accumulates oil and gas. All of these factors need to be in place at the correct time and work together to be able to produce a petroleum system (Magoon, 1988).

In the Barents Sea, there is many evidence of functional petroleum systems, for example, the Goliath and Wisting field. Several wells in the Barents Sea have hydrocarbon discoveries but fails as a petroleum system due to leakage during the Cenozoic uplift and erosion. This uplift and erosion has also resulted in completely and partly erosion of most of the Paleogene section and the entire Neogene section in the area (Vorren et al., 1991).

Most of the hydrocarbons found in the Barents Sea have been gas. This is most likely a result of the uplift as well – the uplift causes drop in pressure in the reservoir, and this results in a gas expansion. When the gas expands, the gas will eventually force the oil-water contact deeper, and result in oil reaching the spill point (Nyland et al., 1992).

Another challenge in the area is that the source rock is moved further up due to uplift. Both pressure and temperature decreases, and can potentially reduce, or even stop, the production of hydrocarbons.

According to Ohm et al. (2008), there is evidence for non-co-genetic gasses in wells in the Western Hammerfest Basin. This can be explained by different source rocks for hydrocarbons in the reservoirs. Isotopes show that there is gas present in reservoirs that have arrived the reservoir after the uplift in Cenozoic times. This implies that the uplift has not "frozen" all of the petroleum systems and that it still exists live petroleum systems in parts of the Barents Sea (Ohm et al., 2008).

Source rock

A source rock refers to a rock that under favorable conditions can be transformed into hydrocarbons. First, the source rock needs to contain organic materials that can be converted to oil or gas. Second, the temperature needs to be between 65 °C and 150 °C for the rock to be able to produce oil. If the temperature is less than 65 °C, the transformation will stop, and if the temperature exceeds 150 °C, the source rock can start to produce gas. Pressure and time are also necessary for hydrocarbon transformation – if a source rock has not been buried deep enough over a longer period, the oil does not form (Hyne, 2012).

In the Barents Sea, the Hekkingen Formation (Upper Jurassic shale) is the most significant source rock because of high total organic carbon (TOC), hydrocarbon generative potential and hydrogen index (HI) (Figure 2.2) (Ohm et al., 2008). The Hekkingen Formation contains a mix of organic sources, indicating a deep marine deposition. Also, the Barents Sea is what's called a multisource basin, which means that there are several types of source rocks. In addition to the Hekkingen Fm, the area also produces hydrocarbons in Fuglen, Nordmela, Tubåen, Snadd, Kobbe and Permian source rocks (Ohm et al., 2008).

The average source rock in the Barents Sea is more mature than the source rocks in the North Sea due to a higher temperature gradient in the Barents Sea (Ohm et al., 2008, Dallan et al., 1988). Even though there are a high maturity and vast amounts of source rocks in the area, the negative effects of uplift and erosion are important to consider when analyzing the potential in the Barents Sea.

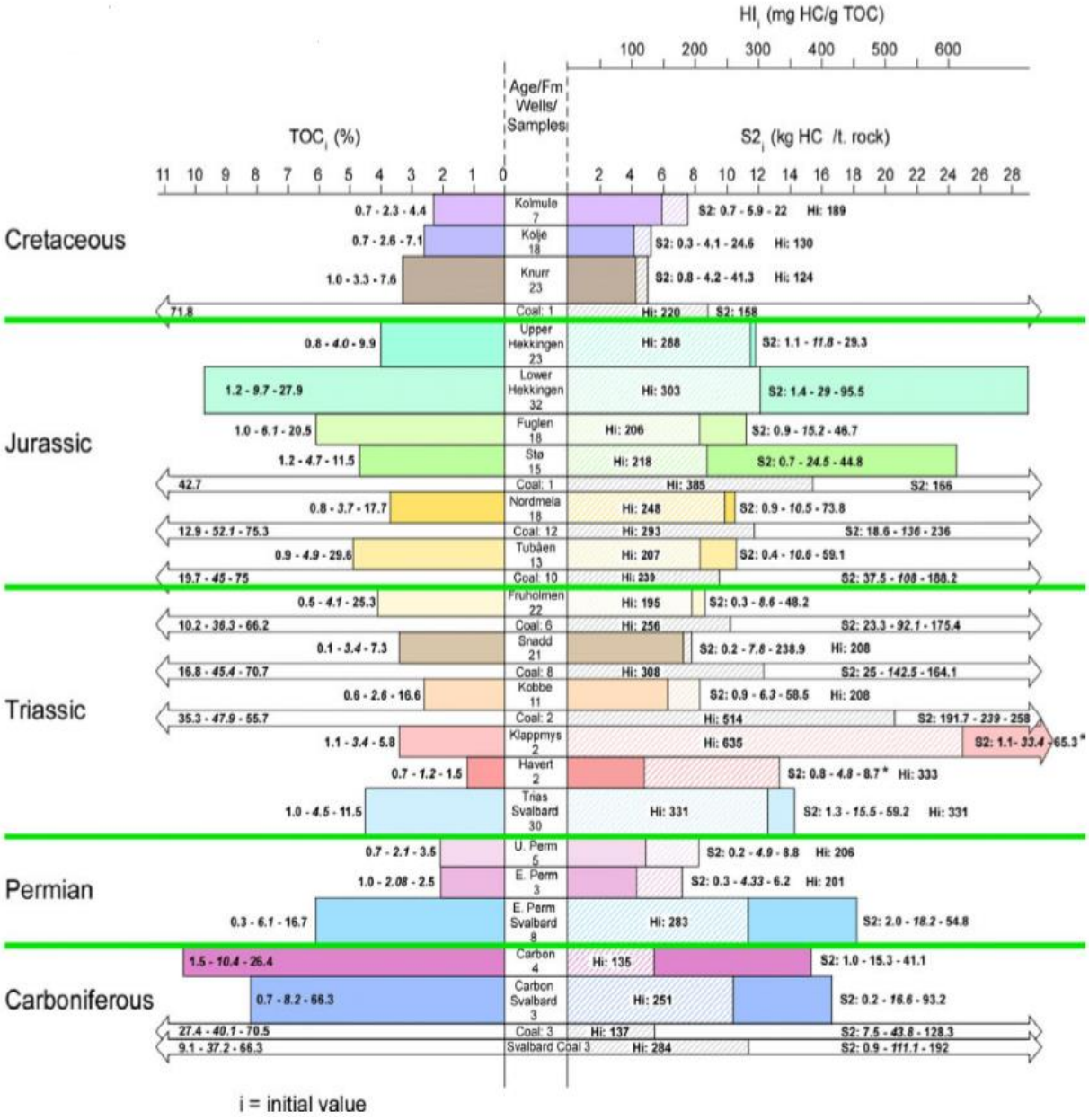

Figure 2.2 – The figure shows the source rock properties in the Barents Sea from Carboniferous to Cretaceous (Ohm et al., 2008).

Reservoir rock

A reservoir rock can be any rock that has high enough porosity and permeability to accumulate hydrocarbons. The two most important reservoir rocks in the world are siliciclastic (50-60 %) and carbonates (40 %). The properties in both reservoir types are determined by the depositional environment (textural and mineralogical composition) and burial history (Bjørlykke and Jahren, 2010).

The Triassic section consists of deltaic deposits formed as clinoform packages and large deltaic channel systems (Kjølhamar, 2015). The most important potential reservoir formations in the section are the Fruholmen formation. This formation can in some areas have a good sandstone quality in the top of the formation (NPD, 2014).

The Jurassic section is the most successful succession in the Barents Sea and the Hoop area regarding hydrocarbon exploration. Larsen et al. (1993) and Doré (1995) estimates that about 85% off hydrocarbons in the Barents Sea will be in this formation and that 90 % of the hydrocarbons are gas (Duran et al., 2013). There have been confirmed excellent reservoir properties in the area, and the Wisting well proved that there is oil in succession. The most significant formation in Jurassic is the Stø formation.

Migration in area

Migration is defined as movement of hydrocarbons from a source rock towards a reservoir and is buoyancy-dependent because hydrocarbons have a lower density than water (brine). Therefore, migration of hydrocarbons has always an upward trend. There are primarily two types of migration – primary and secondary. The primary migration is the process when hydrocarbons leave the source rock, and the secondary is the migration of hydrocarbons along a carrier bed towards a reservoir (Schowalter, 1979).

Migration in the Hoop area (and generally for uplifted areas) is difficult to understand completely. This is because of the insecurity regarding changes in the migration pathways from maximum burial to present day. Several episodes with uplifts, tilting, and erosion may have altered migration routes several times and could potentially have spilled hydrocarbons, or relocated them to unexpected areas (Zięba, 2016). Even though there are many uncertainties regarding migration routes in the Hoop area, it has undoubtedly been one or several effective migration routes. This is proved by among others the Wisting discovery.

Traps in area

To trap hydrocarbons, one needs geological structures that can close off further migration, like an upside-down bucket. There are two main types of traps; structural traps and stratigraphic traps (Broadhead, 2002). Structural traps are formed by deformation of rocks, for example, folding, faulting, and doming. Stratigraphic traps do not require deformation, but traps hydrocarbons by change in facies like sandstone enclosed in shale (Bjørlykke and Jahren, 2010). Both trap types need to be impermeable rocks, preventing the trap from leaking.

Triassic and late Permian reservoirs usually have both traps related to faulting and doming, and traps in the Jurassic fields in the Norwegian Barents Sea are structural traps (fault-bounded positive blocks) (Doré, 1995).

Cap rocks in area

A hydrocarbon seal consists of rocks with low enough permeability to prevent gas or oil flowing through. This impermeable rock can be the top, bottom, lateral and a fault that is closing off reservoir rocks and prevent hydrocarbons from migrating out of the reservoir. Several types of rocks can function as seal – shales, evaporites, very shaley sandstones, cemented sandstones, etc. The capacity of a seal is a function of the throat size of the pores, wettability and interfacial tension (Daniel and Kaldi, 2008).

The seal is a critical factor for hydrocarbon accumulation in a reservoir. Both seal capacity and the extent of the seal is crucial for the height of the oil column.

Most of the reservoirs in the Norwegian Barents Sea are sealed by overlying shales, including the Stø formation. The stø formation has the shaley Fuglen formation as a cap rock and is normally known as a good cap rock (NPD, 2014a).

2.4 Stratigraphy

The stratigraphy in the southwestern Barents Sea, and the Hoop Fault Complex, is controlled by several tectonic events that have affected the sedimentation in the area. These tectonic events can be divided into two tectonic phases during the Caledonian compression deformation and several tectonic events later (Gabrielsen et al., 1990).

The western Barents Sea has a metamorphic basement formed during the Caledonian orogeny when the Iapetus Ocean was closed. In later tectonics, it is possible to see the impact these structures have on the area in general. It is easy to find these NE-SW trends, as the Hoop Fault Complex.

The stratigraphy in the western Barents Sea can roughly be divided into three geological eras – Paleozoic, Mesozoic and Cenozoic:

1. The first one was the Paleozoic era characterized by several tectonic events. In late Devonian, there was many extension and compressional events (Gudlaugsson et al., 1998), followed by late Carboniferous and late Permian rifting.

2. In Mesozoic, the most important event was the subsidence and the formation of Sag basin during Middle Triassic to Middle Jurassic. From Late Jurassic until early Cretaceous the general trend in the Barents Sea was an uplift trend, except the southwestern Barents Sea where the subsidence continued. This resulted in significant amounts of deposits in the region until late Cretaceous (Glørstad-Clark et al., 2010)

3. During Cenozoic, rifting was the most dominating tectonic event and was connected to the opening of the Norwegian-Greenland Sea. After Miocene time (in Pliocene and Pleistocene) there was repeated glaciations that resulted in significant uplift, and this led to the erosions in Paleogene and Neogene (Tertiary time). In the Hoop Faults Complex these sediments are mostly eroded away (Faleide et al., 1996).

Using the Apollo Well (7324/2-1) as the reference well – the relevant groups and Formations encountered in the well are listed in Table 2.1. The most significant formation for this thesis is Fuglen, Stø, and Fruholmen (orange background in Table 2.1).

Top depth [m]	*Lithostratigraphic unit*
484	NORDLAND GP
484	NAUST FM
544	ADVENTDALEN GP
544	KOLMULE FM
694	KOLJE FM
737	KNURR FM
755	HEKKINGEN FM
757	FUGLEN FM
849	KAPP TOSCANA GP
849	STØ FM
871	FRUHOLMEN FM
894	SNADD FM

Table 2.1 – The Table shows the groups and formation that was entered during the drilling. It shows the depth where each group and formation was entered, and the formations used in this thesis are marked in orange (NPD, 2016a).

Adventdalen Group

The Adventdalen Group varies in thickness from 900m in the Bjørnøyrenna Fault Complex and down to the 300m north of the Troms-Finnmark Fault complex. On structural highs in the center of Hammerfest Basin, the thickness might be as low as 60 meters due to erosion. The Group consists of five formations – Kolmule, Kolje, Knurr, Hekkingen and Fuglen (Figure 2.3). For this thesis, the Fuglen formation is the most interesting because it is the cap rock for the Stø formation. Adventdalen Group consists mainly of dark marine mudstones with locally deltaic, and shelf sandstones are dominating the sequence (NPD, 2014). In well 7324/2-1 the thickness for this group is 305 meters.

Fuglen Formation

The Fuglen formation is 92 meters thick in the reference well, and consist of mudstone interbedded with limestone. It is deposited during high stand in marine environments and is an excellent cap rock in the Barents Sea (NPD, 2014, NPD, 2016a).

Kapp Toscana Group

The Kapp Toscana group consists of shales, siltstones, and sandstones. The group is subdivided into five formations: Snadd, Fruholmen, Tubåen, Nordmela and Stø (Figure 2.3). The thickness of the group is in general very thick (up to 2000 meters in the Barents Sea). The Stø formation is the most important formation in this thesis, due to the excellent reservoir quality (NPD, 2014b).

Stø Formation

This formation is the reference formation in the thesis and is 22 meters in the 7324/2-1 well, and is dominated by well-sorted and mature sandstones. Being deposited in a prograding coastal regime, the sandstone also contains some thin units of shale and siltstone in the upper part of the formation. In well 7324/2-1, the lower 14 meters is sandstone, and the upper 8 meters is shaley. This formation is in general thinnest in East, and increases in thickness westwards (NPD, 2014b, NPD, 2016a).

Fruholmen Formation

This formation consists of gray to dark shales and is mainly deposited as open marine shales. In the well, this formation is 23 meters (NPD, 2016a). The formation contains sandstones in the middle part, that is deposited in coastal and fluvial environments (Dallan et al., 1988).

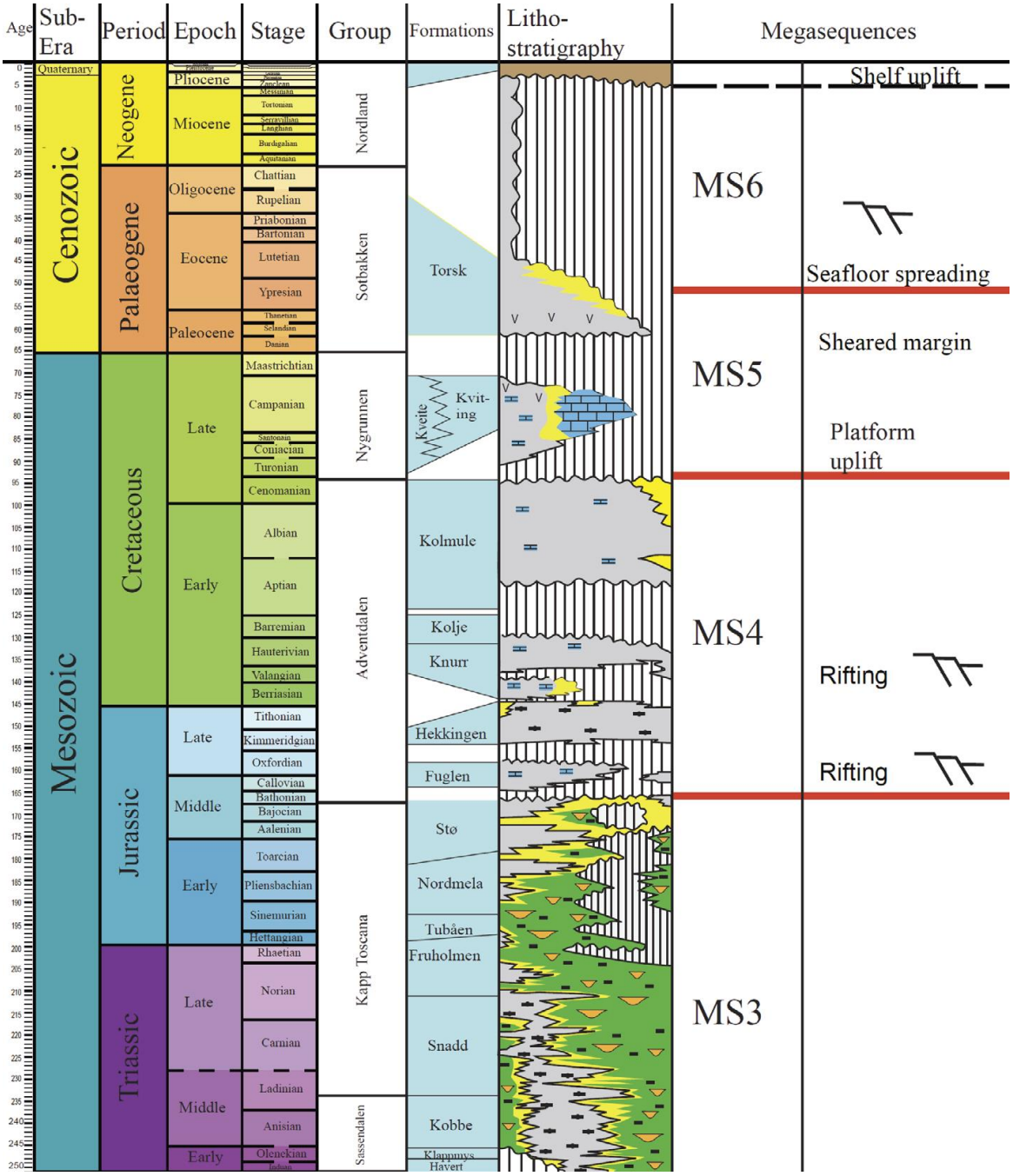

Figure 2.3 – The figure displays the lithostratigraphic from Triassic to Neogene (Glørstad-Clark et al., 2010).

2.5 Exploration challenges in the Barents Sea

There are several challenges regarding exploration in the Barents Sea. First, there are problems connected to infrastructure. Because of its remote position and long distances between hydrocarbon discoveries, it is at this point expensive to develop the discoveries made. Secondly, there are many challenges due to the significant amount of uplift and erosion during the Cenozoic. Uplift and erosion in an area do affect all the aspects of a petroleum system:

1. Source rock – When source rocks are uplifted the temperature decreases, and the hydrocarbon production will cease, or at least be reduced to a minimum after some time. This will particularly have a significant impact on reservoirs with a late trap formation and therefore are depending on a late charge (Henriksen et al., 2011b).
2. Reservoir – They are significantly porosity dependent, and the porosity is dependent on pressure and temperature. Therefore, the reservoir quality is mostly dependent on the depth (temperature) and time of burial. The uplift will still affect the reservoir quality because uplift makes the rocks expand and extensional fractures will occur. This might improve the permeability of the reservoir but will not have a significant impact on the porosity (Bjørlykke and Jahren, 2010).
3. Migration – Uplifted areas can have a significant different migration path at the maximum burial compared to today. The migration routes may also have changed many times during uplift periods (Henriksen et al., 2011b).
4. Trap – Stratigraphic, anticline and salt-related structural traps do have a good chance to withstand uplift effects. Traps that are fault-bounded are most exposed to the uplift and might be spilling oil during uplift periods. Another problem with spilling hydrocarbons due to uplift might be the fact that uplift makes the gas expand, forcing the oil below the spill point (Doré, 1995).
5. Seal – Seals on top of reservoirs, are exposed to the uplift effects. The uplift makes the seal expand (like the reservoirs) and creates extensional fractures. These fractures can compromise a prospect due to spill from the reservoir. This might be critical for a particular reservoir but might lead to the charging of other reservoirs (Doré, 1995).

As mentioned, the focus of this thesis is the sandstone reservoir (second point), and the next three chapters describe the methods and theories needed to model rock physics properties for the burial history of the Stø reservoir.

Chapter 3: Research methodologies and theoretical background

This chapter presents the background information and theories for the estimation of burial history, rock physics modeling and the AVO-modelling, respectively.

3.1 Burial history

The burial history includes both compaction and uplift and has a significant impact on rocks physical properties. Therefore, it is important to establish an estimated burial history when investigating rock properties in hydrocarbon exploration. This burial history can tell if the area of interest has been chemically compacted in the past, for how long time the area has been the different compaction regimes and how much uplift it has experienced.

In this section, theory for both chemical and mechanical compaction and uplift will be presented. In addition, the effects these have on rock properties.

It exists several descriptions of the burial history in the Barents Sea, and one of these estimates is presented by Ohm et al. (2008), Figure 3.1. This burial history describes various parts of the Barents Sea, and how these areas of the Barents Sea has evolved the last 100 Ma years.

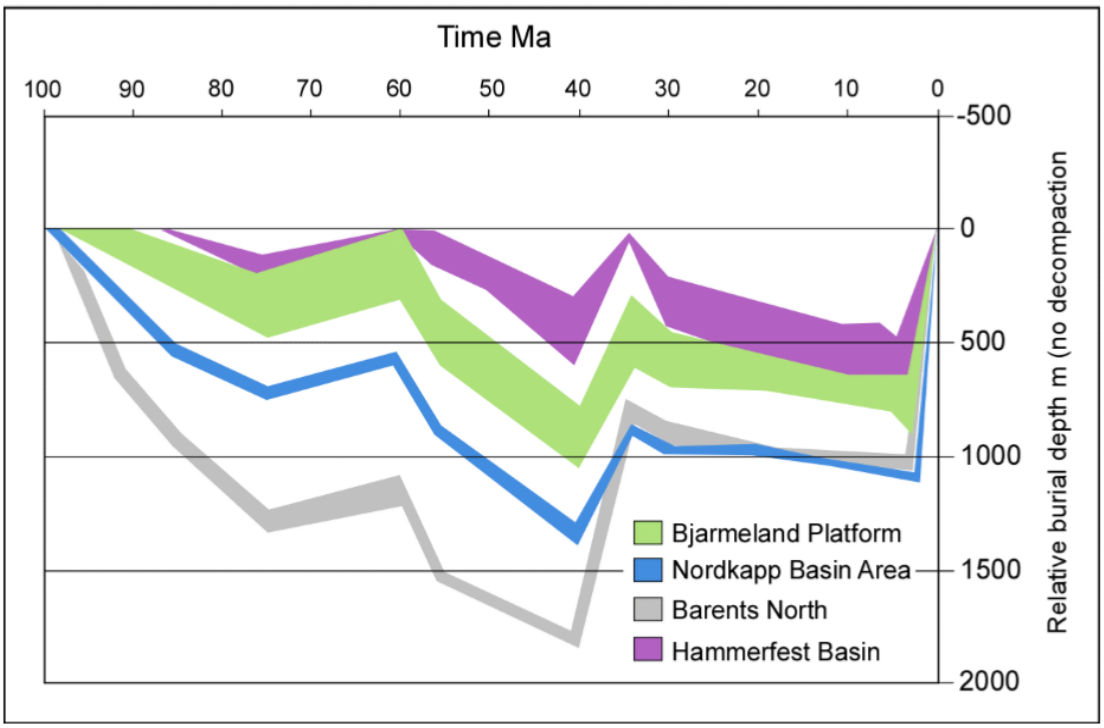

Figure 3.1 – The figure displays the burial history for different areas in the Barents Sea (Ohm et al., 2008). The Bjarmeland Platform is the area closes to the Hoop Fault Complex.

3.1.1 Various burial effects

Sedimentary rocks are by far the most common reservoir rocks outside the Middle East. It is therefore critical to understand burial processes – and its impact on sediments physical and chemical properties. Burial processes include chemical, physical and biological changes in sediments after deposition – transforming deposits into a sedimentary rock (Bjørlykke and Jahren, 2010).

A basin will be filled with unconsolidated sediments, and newer unconsolidated sediments will overlay the earlier infill. As this goes on these unconsolidated sediments will be buried deeper and be exposed to higher pressure and temperature. This burial process triggers the diagenetic processes and transforms the unconsolidated sediments into consolidated rocks, and drastically changes the rock properties (Bjørlykke and Jahren, 2010).

The most significant changes in rock properties due to compaction are velocity, permeability, porosity and the bulk and shear modulus. These features are closely related, and important for the reservoir quality. To get a good understanding for a reservoirs quality one needs to understand the two most important burial processes; mechanical and chemical compaction. Also, it is important to understand how uplift impacts the reservoir attributes (Bjørlykke and Jahren, 2010).

According to Marcussen et al. (2009), estimates of burial history is a crucial input for example for rock physics modeling, seismic interpretation, depth conversions and exhumation characterization.

Mechanical compaction

Once the sediments are deposited and the overburden increases, the mechanical compaction starts. This is the dominating factor for change in rock properties until the temperature reaches approximately 70 °C, and rock is in the chemical compaction domain (Mondol et al., 2007, Bjørlykke and Jahren, 2010). This process involves grains getting packed closer together, and is a result of rearranging and fracturing of sand grains and collapsing of platy mineral structures in shale due to the increased effective stress (Worden and Burley, 2003). The effective stress is defined as the overburden vertical stress minus the pore pressure in sediments. This stress is transmitted through the grain framework and drives the mechanical

compaction. When the stress builds up, the porosity in the sediment lowers and increases the mechanical stability (Bjørlykke et al., 2015).

Several factors influence mechanical compaction such as mineral composition; such as sorting and grain shape. These factors are closely linked to the transportation and mechanisms before deposition (Mondol et al., 2008, Mondol, 2009). This is important because well sorted coarse-grained sand is more compressible than fine-grained (Bjørlykke and Jahren, 2010), because the coarser grains are typically less mature than fine-grained sands, making them weaker for fracturing (Figure 3.2). The mechanical compaction for shale is more complicated as it depends on grain size, grain strength specific surface and surface charges (Bjørlykke and Jahren, 2010).

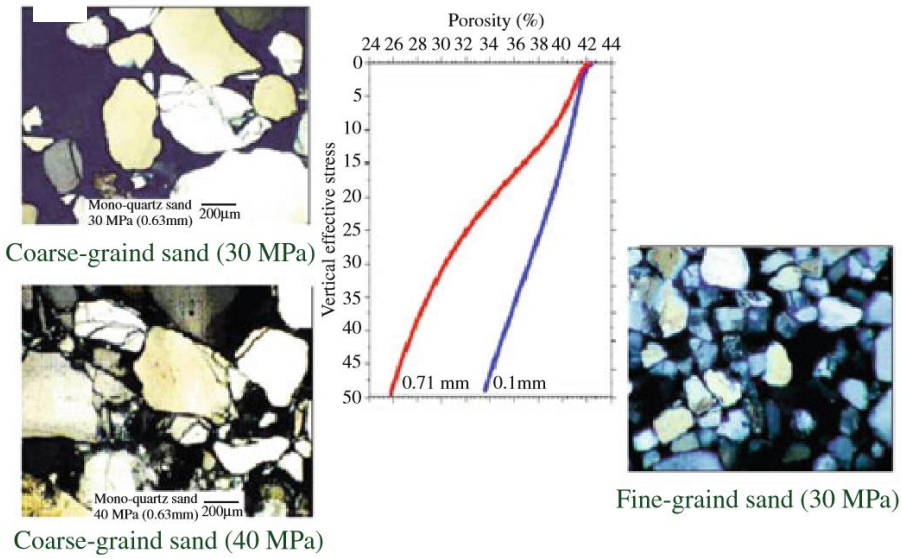

Figure 3.2 – The figure displays the effect of sand grain size on mechanical compaction (Bjørlykke and Jahren, 2010).

Chemical compaction

Chemical compaction includes dissolution of solids, precipitation, and cementation. These processes make the primary minerals more stable, and in equilibrium with changed thermodynamics due to a higher temperature.

When sediment reaches a temperature at 70–80 °C (usually at depths of 2,0-2,5 km) quartz can start to cement (Bjørlykke and Jahren, 2010). This is called the transition zone between mechanical and chemical compaction domain for sandstone. The transition zone is temperature dependent and varies in depth from area to area depending on the geothermal gradient. Once onset of quartz cement has started, the chemical compaction is the most significant diagenesis affecting rock properties. This is because quartz cementation strengthens the rocks faster than the overburden stress increase (Bjørlykke and Jahren, 2010).

After 2-4% quartz cement the mechanical compaction will be insignificant, further compaction will therefore mainly be due to chemical compaction. The porosity in well-sorted quartz arenites and feldspathic sandstones will be drastically reduced due to cementation of quartz, and the amount of quartz cement is a function of grain surface area available for quartz precipitation and a time-temperature integral (Walderhaug, 1994). For example, a high geothermal gradient and a slow burial will increase the amount of quartz cementation (Bjørlykke and Jahren, 2010).

Compaction, either mechanical or chemical, does overall drive towards lower porosity and increased density, bulk and shear modulus, and velocity (Figure 3.3).

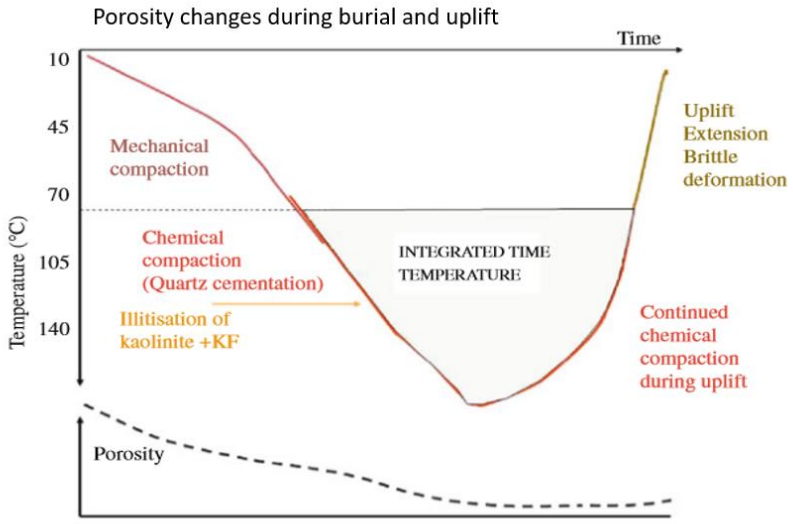

Figure 3.3 – The porosity evolution for various burial scenarios: mechanical and chemical compaction and uplift (Bjørlykke and Jahren (2010).

Uplift

Uplift refers to an event where the earth's surface gets a vertical elevation, and can, for example, occur due to isostasy or tectonic processes (Gornitz, 2008). Uplift is closely related to erosion processes, as the starts as soon as a landform is elevated higher than the wave base. From this point the erosion processes are active. For petroleum exploration, the important uplift is the net uplift; the difference between maximum burial depth and the current depth of the area of interest (NPD, 2014a). Net uplift is important because it gives an idea of the rock physics properties the area have experienced in the past (Doré, 1995).

As mentioned, the uplift is most likely the reason for several potential reservoirs being dry in the Barents Sea. This could be a combination of leaking seals due to the formation of cracks during uplift and that the lowered temperature allows the gas in the top of the reservoir to expand, forcing the gas-oil contact under the spill point (Nyland et al., 1992).

Uplift might increase the porosity of a reservoir slightly, due to cracks that occur during uplift. Lower temperature and pressure also decreases the bulk modulus and shear modulus (Narongsirikul et al., 2013a).

3.1.2 Estimation of shale fraction

The transition zone from mechanical to chemical compaction

The transition zone from mechanical to chemical compaction can be identified using different cross-plots using the well data as input:

- According to Storvoll et al. (2005) and Marcussen et al. (2010), 2-4% cementation increase the velocity significantly, and a velocity-depth plot can, therefore, be a good indicator. For the velocity-depth plot, it is important to recognize different velocity gradients to see if the velocity trend changes drastically over a particular depth.
- Porosity-shear modulus plot could give an idea of changes in porosity, that is not fluid dependent. There should be a significant increase in the shear modulus after chemical compaction has started, and the porosity should continuously decrease.

The gamma ray log is a very useful lithology indicator for quality control to check if the velocity is caused by lithological changes or not.

Volume of shale calculation

Gamma ray log measures natural radioactivity in rocks and can be used as a lithology identification tool (Hamada, 1996). This is because sandstone (and carbonate) have low radioactivity compared to shale. Therefore, it is possible to distinguish between shale and sandstones from gamma ray log. Gamma ray log can also be used to determine the volume of shale in porous reservoirs. The first step of the computation is the formula for gamma ray index (I_{GR}) (Atlas, 1982):

$$I_{GR} = \frac{GR_{log} - GR_{min}}{GR_{max} - GR_{min}}. \tag{3.1}$$

GR_{log} is the gamma ray reading of the formation. GR_{min} is the minimum gamma ray in the lag corresponding to clean (cleaner) sandstone and GR_{max} correspond to the maximum value in the gamma ray log, representing shale.

The gamma ray index is the first-order estimation of shale volume. This linear response can easily be used as $Vs_{hale} = I_{GR}$. The problem with this approach is that it is pessimistic and predicts a higher shale volume than a nonlinear approach. The nonlinear responses are based on geographic area, the age of formations and fitted to local information (Bassiouni, 1994).

There are presented many equations for non-linear responses, but in this thesis Clavier et al. (1971) equation is used:

$$V_{sh} = 1.7 - \sqrt{3.38 - (I_{GR} + 0.7)^2}. \tag{3.2}$$

In this study, Equation 3.1 is used for zones in the mechanical compaction regime, and Equation 3.2 is used for the chemical compaction zone.

Temperature Gradients

The transition from mechanical to chemical compaction is highly temperature-dependent (Bjørlykke and Jahren, 2010). The temperature gradient can, therefore, tell us where the cementation sets in and the reservoir properties change drastically. The temperature gradient can be found using the bottom hole temperature, the surface temperature and the depth of the well. The formula used for this is:

$$T_{gradient} = \frac{T_{bottom} - T_{top}}{Z_{bottom} - Z_{top}}, \tag{3.3}$$

here, T_{bottom} and T_{top} represent the temperature at the bottom and top of the well (in °C), and Z_{bottom} and Z_{top} represent the depth and top of the reservoir (in km).

3.2 Rock physics modeling

3.2.1 Introduction

This section will provide the theoretical framework used in this study for the rock physics modeling of a specific burial history.

Rock physics modeling is a method used for predictions of elastic properties of rock at different depths, with different mineralogy, microstructures, and fluids. The rock properties observed today, and their seismic signatures, are controlled by these factors. The rock physics properties

can change a lot during a burial history, and particularly in areas with a complicated burial history, such as the Barents Sea area. As discussed, when rocks experience an increased compaction, it leads to stiffer rocks, and when the rocks are being uplifted, it can lead to cracks and slightly increased porosity (Narongsirikul et al., 2013a, Lehocki and Avseth, 2015). The Barents Sea has experienced both compaction and uplift. This makes it harder to estimate how the rock properties are changing through time, and different rock physics models are needed to describe the elastic properties from deposition until today.

The modeling of elastic properties in this study is based on the burial history of the Stø Formation in the Apollo well in the Barents Sea (see Figure 3.4). In this study, the complex burial history is divided into various burial scenarios for further investigation, with the aim to understand the complete burial history's impact on the elastic properties observed today. The rock physics modeling in this thesis is done using Dvorkin and Nur (1996) friable sand theory and contact cement theory, in addition to Avseth et al. (2014) so-called Kite model.

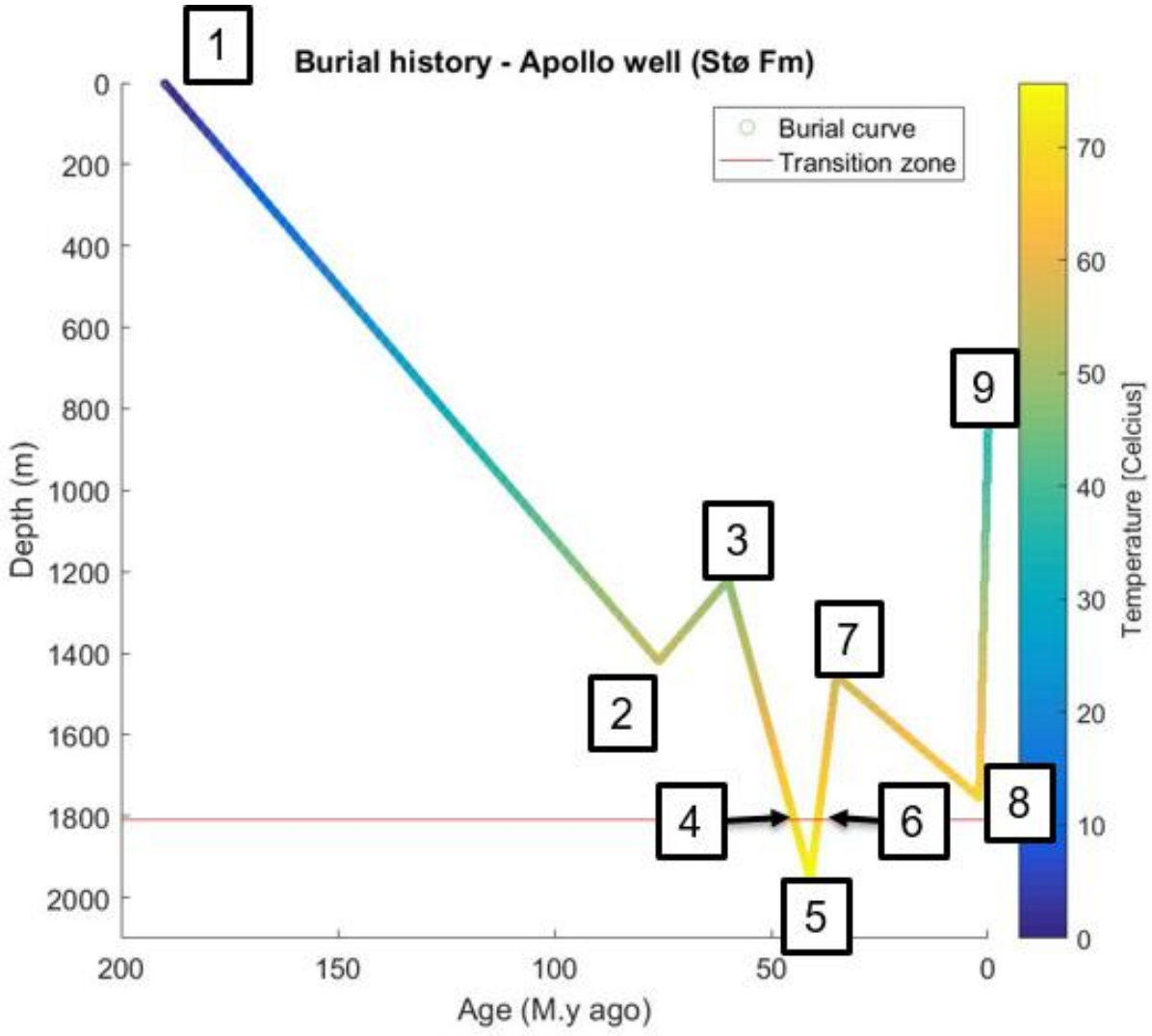

Figure 3.4 – The burial history for the Stø formation, from deposition (1) until today (9). The curve displays the burial depth versus time, and the numbers represents points for further modelling. The transition zone is marked, and the curve is color-coded for temperature.

3.2.2 Theoretical background

Reservoir parameters

Several parameters are used when characterizing a reservoir, and the most important are:

- *Fluid saturation* – term used for the type and amount of fluid in a rock. The three main types of fluids normally used are brine, gas, and oil.
- *Porosity describes* – the volume fraction of the rock the fluids may occupy.
- *Permeability* – describes how easily a fluid flows through rock and is important for the extracting of hydrocarbons from a reservoir.
- *Lithology* – is a common name for the different minerals forming the rock. This parameter is important for both reservoir and cap rock.
- *Pressure and temperature* – are normally depth dependent and are important for the effective rock properties, and can start the cementation of a reservoir.
- *Bulk modulus* – is a measurement of a medium resistance to volume changes as a response to change in pressure.
- *Shear modulus* – describes the resistance of a medium resistance to shear deformation.

P- and S-wave velocities

Pressure- and shear waves are elastic waves propagating within a medium. They deform the medium elastically and returns rocks to their original shape and position after the wave has passed. The velocities of these waves can provide valuable information for rock- and fluid properties and is found using the formula

$$V_P = \sqrt{\frac{K + \frac{4}{3}\mu}{\rho}}, \tag{3.4}$$

for P-waves and

$$V_S = \sqrt{\frac{\mu}{\rho}}, \tag{3.5}$$

for S-waves. K represents the bulk modulus, μ the shear modulus and ρ is the effective density, given by

$$\rho = V_1\rho_1 + V_2\rho_2 + \cdots V_M\rho_M = \sum_{j=1}^{M} \mathrm{V_j}\rho_j, \tag{3.6}$$

where V_M is the volume fraction of the various constituents in the rock, and ρ_M the corresponding density. For N constituents, the density can be expressed as the sum of ρ_j for each constituent, where the V_j is the volume fraction of the j^{th} constituent.

Effective pressure

The effective pressure at each depth is estimated using Terzaghi's principle (Skempton, 1960); the formula calculates the effective pressure when assuming pore pressure as hydrostatic:

$$P_{eff} = (\rho_{rock} - \rho_w)gz, \tag{3.7}$$

Where P_{eff} is the effective pressure at a given depth, z. ρ_{rock} is the average density for saturated rocks and ρ_w are the average water density. In this study, the ρ_{rock} is 2,0 g/cm^3 and ρ_w is 1,0 g/cm^3. The gravitational, g, is 9,81 m/s^2.

Saturation and properties of pore fluid

Reservoirs normally contain gas, oil, brine, or a mix of these fluids. The empirical relationship presented by Batzle and Wang (1992) and Han and Batzle (2000) is used for finding properties of the pore fluids is in this study. It predicts both density and bulk modulus as a function of fluid pressure and temperature in the reservoir, for a known fluid composition.

Gassmann's fluid substitution

Gassmann (1951) equation is used to predict changes in rock modulus as a result of a change in pore fluids when the bulk modulus of the dry rock, the pore fluid, and the solid matrix is known:

$$K_{sat} = K_{dry} + K_{mineral}\frac{\left(1 - \frac{K_{dry}}{K_{mineral}}\right)^2}{1 - \frac{K_{dry}}{K_{mineral}} + \Phi\left(\frac{K_{mineral}}{K_{fluid}} - 1\right)}, \tag{3.8}$$

and

$$\mu_{dry} = \mu_{sat}, \tag{3.9}$$

K_{sat}, K_{dry} and $K_{mineral}$ is the bulk modulus for the saturated rock frame, dry rock, and fluid saturated, respectively. The porosity of the rock is described by Φ, and the shear modulus μ is unchanged if the fluid changes in Gassmanns theory. The fluid bulk modulus K_{fluid} is calculated with the formula by Reuss model for fluid mixtures (Han and Batzle, 2004):

$$\frac{1}{K_{fluid}} = \frac{S_{water}}{K_{water}} + \frac{1 - S_{water}}{K_{gas}}, \tag{3.10}$$

Here, K_{gas} and K_{water} is the bulk modulus for gas and water, and S_{water} is the water saturation.

Several assumptions are needed when applying Gassmann's relations (Mavko et al., 2009):

- The mineral needs to be homogeneous (same shear and bulk modulus), and the pore space must be statistical isotropic.
- Gassmann's equation is only valid at sufficiently low frequencies (10-100Hz).
- The rock needs to be isotropic.
- There should be a connection between pores, and the pore fluid fills the entire pore space and is homogeneous.
- Gassmann's equation assumes that the bulk modulus for dry rock is not dependent of fluid substitution

Hashin-Shtrikman upper and lower bounds

This method is used for estimation of the effective modulus of an isotropic linear elastic composite when considering a two material composite (Hashin and Shtrikman, 1963). The two bounds are used to interpolate the moduli between the mineral point and the well-sorted end member. The upper and lower bounds is defined as

$$K_{HS}^{\pm} = K1 + \frac{f_2}{(K_2 - K_1)^{-1} + f_1\left(K_1 + \frac{4}{3}\mu_1\right)^{-1}}, \tag{3.11}$$

and

$$\mu_{HS}^{\pm} = \mu_1 \frac{f_2}{(\mu_2 - \mu_1)^{-1} + 2f_1(K_1 + 2\mu_1)/[5\mu_1\left(K_1 + \frac{4\mu_1}{3}\right)]}, \tag{3.12}$$

where K_1 and K_2 are the bulk modulus for two materials, 1 and 2. μ_1 and μ_2 are the shear modulus for the two materials, respectively. The fraction of each material is described by f_1 and f_2. See Figure 3.5. When the upper bound is used, index 1 represents the stiffer material forming the shell. The lower bound refers to index 1 being the softer material forming the shell. The upper bounds are used when quartz forms the shell around a core of clay, and the lower is used when clay forms the shell around quartz (Mavko et al., 2009).

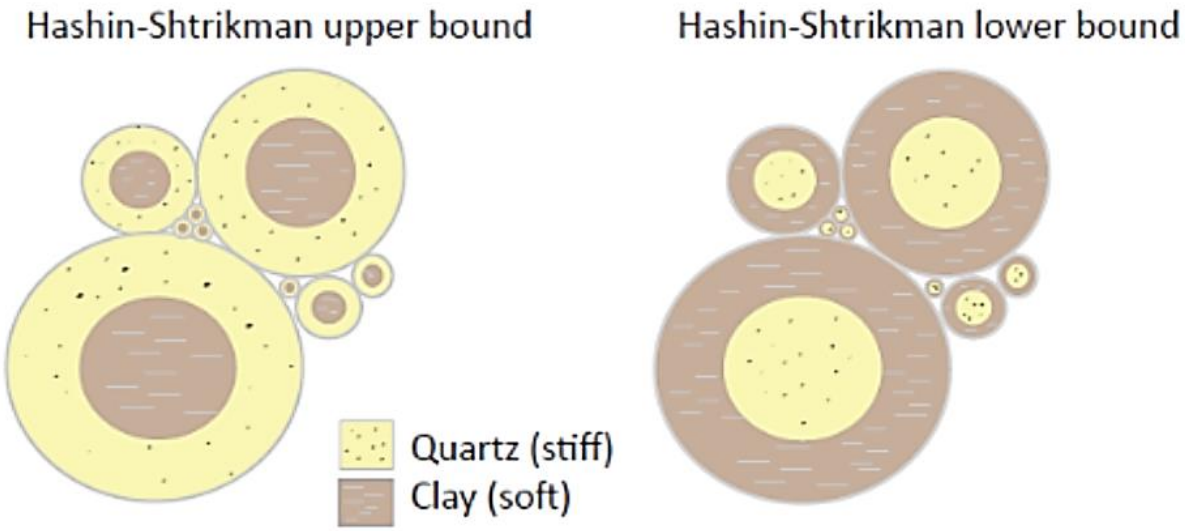

Figure 3.5 – The upper and lower bounds of the Hashin-Shtrikman bounds (Mavko et al., 2009).

Differential effective medium (DEM) modeling

DEM theory is an inclusion based theory for the low-porosity interval ($0 \leq \phi \leq \phi_{max,\ DEM}$). The DEM theory models a two-phase composition, by incrementally adding inclusions of one phase into the other. The elastic modulus for the DEM-theory can be found using the coupled system of ordinary differential equations (Berryman, 1992)

$$(1-y)\frac{d}{dy}[K^*(y)] = (K_2 - K^*)P^{(*2)}(y), \tag{3.13}$$

$$(1-y)\frac{d}{dy}[\mu^*(y)] = (\mu_2 - \mu^*)Q^{(*2)}(y). \tag{3.14}$$

The first phase is used as the host material (K_1 and μ_1), and have a bulk modulus $K_1 = K^*(y=0)$ and the shear modulus $\mu_1 = \mu^*(y=0)$. K_2 and μ_2 are the bulk and shear modulus of the second phase (the added inclusions). $P^{(*2)}(y)$ and $Q^{(*2)}(y)$ are geometrical factors, and are calculated from using them as the inclusions in a background medium with effective modulus K^* and μ^*.

Then the fluid effects are modeled using Gassmann (1951) fluid substitution.

Contact cement theory (CCT)

Dvorkin and Nur (1996) presented a model describing the relationship between velocity and porosity versus cement volume for high porosities. This model is best used when the grains are well sorted, and there is cement in the contact between the grains. The contact cement increases the stiffness of the sand for tiny amounts of cement, and as a result, the velocities increases even though the porosity change is small (Figure 3.6). In this thesis, their model is used to calculate bulk and shear modulus for the chemical compaction regime, where:

$$K_{CCT} = \frac{1}{6}n(1-\phi_{CCT})M_c S_n, \tag{3.15}$$

and

$$\mu_{CCT} = \frac{3}{5}K_{CCT} + \frac{3n}{20}(1-\phi_{CCT})\mu_C S_\tau, \tag{3.16}$$

where, K_{CCT} is the bulk modulus and μ_{CCT} is the shear modulus. The coordination number is represented with n, and ϕ_{CCT} is the critical porosity. S_n and S_τ is the normal and shear stiffness at the grain contacts. Further, ρ_c, Vp_c and Vs_c is the density and velocity (pressure and shear) for the cementing material. The compressional modulus, M_c, and shear modulus μ_c of the cementing material can be found from

$$M_c = \rho_c V_{pc}^2, \tag{3.17}$$

and

$$\mu_c = \rho_c V_{sc}^2, \tag{3.18}$$

here ρ_c, Vp_c and Vs_c is the density and velocity (pressure and shear) for the cementing material.

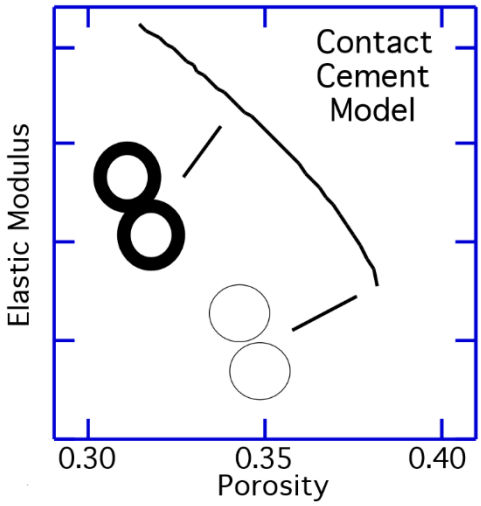

Figure 3.6 – Contact cement theory. The elastic modulus increases, and the porosity decreases due to cementation (Avseth et al., 2010).

The friable sand model

Dvorkin and Nur (1996) combined Hertz-Mindlin contact theory and a modified Hashin-Shtrikman lower bound (Hashin and Shtrikman, 1963) for the friable sand model. This model describes how the relationship between velocity and porosity changes as the sorting of unconsolidated sand deteriorates (Avseth et al., 2010). The formulas used in the friable sand model at critical porosity are given by

$$K_{HM} = \left(\frac{n^2(1-\phi_c)^2\mu^2}{18\pi^2(1-v)^2} * P\right)^{\frac{1}{3}}, \tag{3.19}$$

and

$$\mu_{HM} = \frac{5-4v}{5(2-v)}\left(\frac{3n^2(1-\phi_c)^2\mu^2}{2\pi^2(1-v)^2} * P\right)^{\frac{1}{3}}, \tag{3.20}$$

where the K_{HM} and μ_{HM} are the bulk and shear modulus for dry rock at critical porosity. P is the effective pressure, and n is the coordination number. ϕ_c, μ and v is respectively the critical porosity, shear modulus and Poisson's ratio for the mineral. n is the coordination number. Poisson's ratio can be expressed as

$$K_{dry} = \frac{3K-2\mu}{2(3K+\mu)}, \tag{3.21}$$

And the coordination number can be found from Murphy (1982) empirical equation

$$n = 20 - 34\phi + 14\phi^2, \tag{3.22}$$

Further, the dry bulk and shear modulus for the dry, friable sand mixture is calculated from

$$K_{dry} = \left(\frac{\frac{\phi}{\phi_c}}{K_{HM}+\frac{4}{3}\mu_{HM}} + \frac{1-\frac{\phi}{\phi_c}}{K+\frac{4}{3}\mu_{HM}}\right)^{-1} - \frac{4}{3} * \mu_{HM}, \tag{3.23}$$

and

$$\mu_{dry} = \left(\frac{\frac{\phi}{\phi_c}}{\mu_{HM} + z} + \frac{1 - \frac{\phi}{\phi_c}}{\mu + z} \right)^{-1} - z, \tag{3.24}$$

where

$$z = \frac{\mu_{HM}}{6} \left(\frac{9K_{HM} + 8\mu_{HM}}{K_{HM} + 2\mu_{HM}} \right), \tag{3.25}$$

here K_{dry} and μ_{dry} are the bulk and shear modulus for the dry unconsolidated sand. The mineral bulk modulus is denoted with *K*, and ϕ is the porosity. The pore pressure is assumed to be hydrostatic for the modelling.

Constant-cement model

This model was introduced by Avseth (2000) and is a model combining the contact-cement model and the friable-sand model. The constant-cement model is similar to the friable sand model except at the high-porosity end point, where the bulk and shear modulus is calculated from the contact-cement model. The dry-rock bulk (K_{dry}) and shear (μ_{dry}) modulus can then be calculated from

$$K_{dry} = \left[\frac{\frac{\phi}{\phi_b}}{K_b + \left(\frac{4}{3}\right)\mu_b} + \frac{1 - \frac{\phi}{\phi_b}}{K + \left(\frac{4}{3}\right)\mu_b} \right]^{-1} - \frac{4}{3}\mu_b, \tag{3.26}$$

and

$$\mu_{dry} = \left[\frac{\frac{\phi}{\phi_b}}{\mu_b + z} + \frac{1 - \frac{\phi}{\phi_b}}{\mu + z} \right]^{-1} - z, \tag{3.27}$$

Where

$$z = \frac{\mu_b}{6} \left(\frac{9K_b + 8\mu_b}{K_b + 2\mu_b} \right), \tag{3.28}$$

here, ϕ_b is the reduced porosity because of contact-cement deposition. K_b and μ_b are the dry-rock bulk and shear modulus calculated from ϕ_b. Further, the dry-rock bulk and shear modulus at smaller porosities ϕ are interpolated using lower bound.

Kite model

The so-called kite-model is presented by Avseth et al. (2014) for describing elastic properties of low-to-intermediate-porosity sandstones. The combination of granular medium contact theory and inclusion-based models can be used to make rock physics templates that include complicated burial histories Figure 3.7A and B (Avseth et al., 2014).

The modeling can be divided into three different modeling parts – Dvorkin and Nur (1996) contact cement theory, Berryman (1992) differential effective medium (DEM) and Hashin-Shtrikman bound (HSUB) (Hashin and Shtrikman, 1963). HSUB is used to find the upper limit of the elastic properties, and the DEM-model is used to include cracks. The various parts are described in detail above. This approach to the rock physics modeling covers the entire process from granular- to pore dominated textures. The model uses Gassmann's equation to model for different saturation effects.

The modeling assumes isotropic rocks. From this, the elastic stiffness tensor can be calculated from bulk (K) and shear (μ) modulus, and these parameters can be calculated from P- and S-wave velocity and density using the formulas for *Vp* and *Vs*.

The elastic modulus and the porosity are modeled in three stages; DEM, HSUB, and CCT. The DEM model is used for low-porosities, the CCT model is used for the high (critical) porosity interval, and the HSUB are used for the porosities in between DEM and CCT.

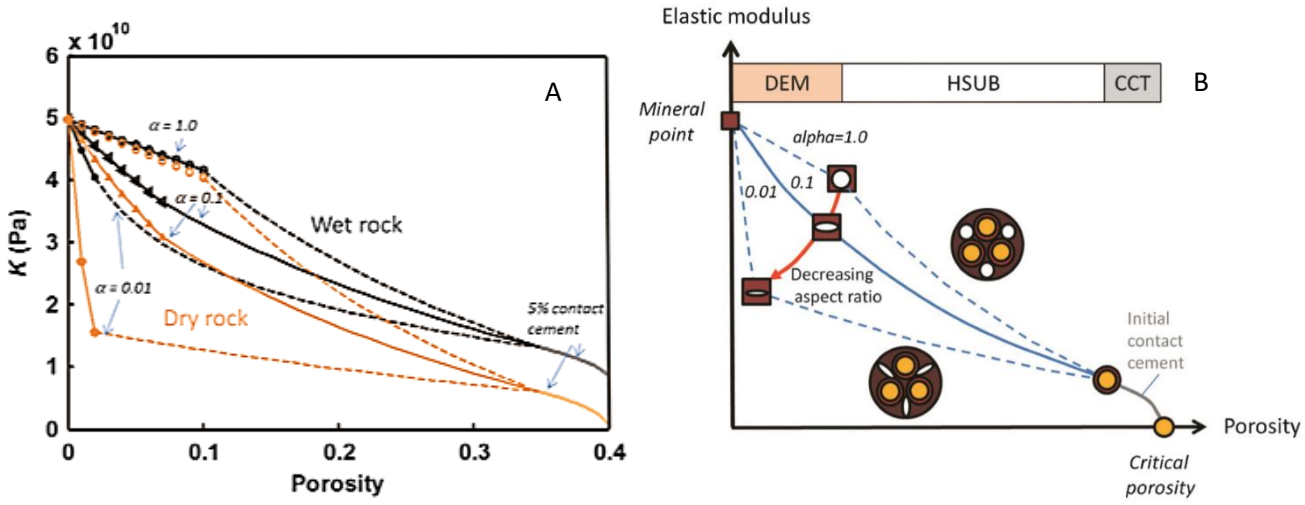

Figure 3.7 – Bulk modulus-porosity cross plot for dry rock versus brine saturated (A), and (B) the combination of DEM-modelling and CCT and the interpolation between the two points by Hashin-Shtrikman upper bound (Avseth et al., 2014).

3.3 AVO-modeling

3.3.1 Introduction

This chapter presents the theoretical background for generating AVO-responses for the different points in the burial history. Gassmann fluid substitution is an important model for AVO-modelling but is already presented in Chapter 3.2.

The idea behind AVO analysis is to estimate various rock parameters from the reflection amplitude as a function of offset. AVO is today widely used in hydrocarbon exploration to identify lithology and fluids. However, there are many pitfalls using AVO analysis that might result in "false" interpretations; for example lithology and overburden effects.

The first person who made a practical use of AVO was Ostrander (1984) when he proved that the amplitude varied with offset for a gas-filled reservoir capped by shale. He related this change to a decrease in Poisson's ratio in the gas-filled reservoir. The year after, Shuey (1985) made an approximation of Zoeppritz equations and proved that Poisson's ratio was the elastic constant most affected by offset-dependent reflectivity. This was the start of AVO analyses in the gas and oil industry (Avseth and Bachrach, 2005).

AVO modeling is a forward modeling method, and its primary use is to create a model of the earth and generate synthetic seismic for this model. This approach is used to find links between the petrophysical properties in the reservoir and the seismic properties. From this it is possible to compare the synthetic seismic to real data, to see if some similarities/differences could explain what real data contains. Therefore, it is important to find a compromise between the complexity of the earth model and the computation time when doing this forward modeling.

3.3.2 Theoretical background

Relationship between *Vp* and *Vs*

Vp, *Vs* and bulk density are the most important input parameters for AVO modeling. The *Vp*-*Vs* relation is also an important lithology indicator (Castagna and Backus, 1993). *Vp* and bulk density are normally measured when drilling wells today, but *Vs* is not always measured in older wells. Other times there might have been some problems during the measuring of these parameters. Therefore, one need to either calculate *Vs*-values for the well or

do a quality control if the measured *Vs*. There are several published *Vp*-*Vs* relationships from different authors (Han et al., 1986, Castagna et al., 1993). These relationships use the same approach; first, they establish an empirical relationship between *Vp*, *Vs*, and porosity for a reference pore fluid, and then uses Gassmann's relations to check the relationship for other fluids. The *Vp*-*Vs* method used in this thesis is the "mudrock line" (Castagna et al., 1985)

$$V_s = 0.8621V_p - 1.1724, \tag{3.29}$$

here the *Vp* is the compressional wave velocity, *Vs* is the shear wave velocity, and they are both measured in km/s. The method is chosen because of its accuracy and pure form.

Angle-dependent reflection coefficient

The acoustic impedance is an important parameter for calculating the reflection coefficient and is given by

$$Z = \rho * v, \tag{3.30}$$

and is defined as the product of density (ρ) and velocity (v). The difference in two layers for this parameter, is used to calculate the reflection coefficient at the intercept between them

$$R = \frac{Z_2 - Z_1}{Z_2 + Z_1}. \tag{3.31}$$

This reflection coefficient is only valid for the normal incident waves, and Z_1 and Z_2 represent the upper and lower layers.

At normal incidence, a P-wave hitting a surface creates reflected and transmitted waves. If the incidence angle is larger than zero it generates reflected S- and P-waves and transmitted S- and P-waves, as shown in Figure 3.8. Snell's law can describe both the transmitted and reflected waves across the interface:

$$\frac{\sin(\emptyset_1)}{\sin(\emptyset_2)} = \frac{V_{P2}}{V_{P1}}, \tag{3.32}$$

here, $\emptyset_1$ and $\emptyset_2$ represents the reflected and transmitted angles (Figure 3.8), and V_{P2} and V_{P1} is the velocity of the lower and upper layer.

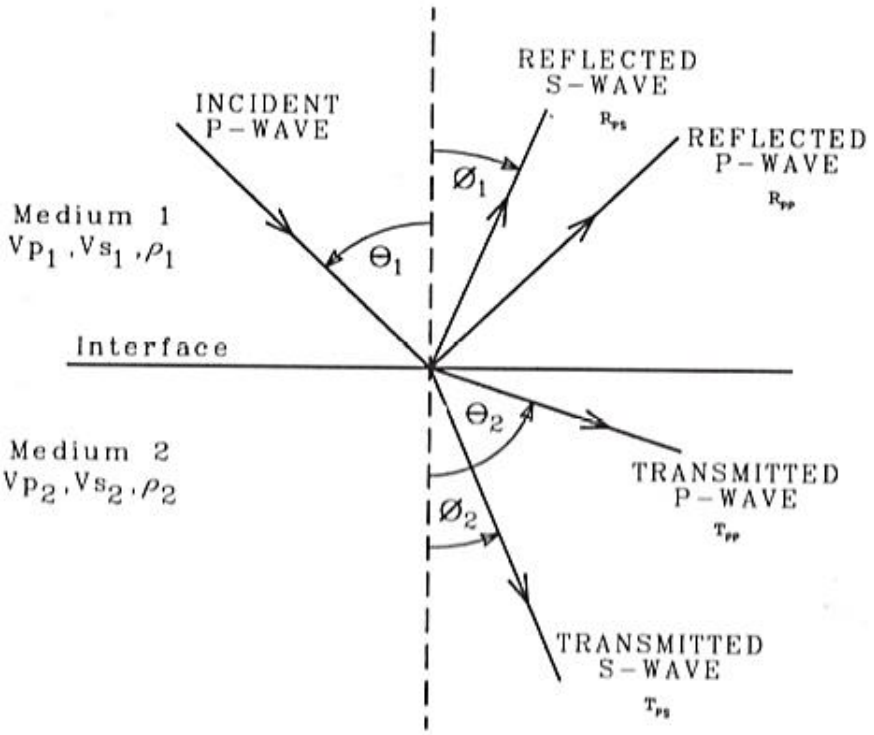

Figure 3.8 – Reflections and transmission at an interface between two layers with different elastic properties (Castagna and Backus (1993).

Zoeppritz (1919) was the first to describe the relationship between the incidence angle and reflection coefficient. He derived the formula from Snell's law by assuming isotropic layers. Furthermore, he "invoked continuity of displacement and stress at the reflecting interface as boundary conditions to solve for the reflection coefficients" as a function of incident angle and the elastic properties of media (Castagna and Backus, 1993). The equation he derived gives an analytical reflection coefficient and is very complicated. Because the complexity of the equation it is difficult to get any physical insight. For this reason, there has been done many approximations of the Zoeppritz equation – among others Bortfeld (1961), Wiggins et al. (1983), Shuey (1985) and Aki and Richards (2002).

Bortfeld (1961) linearized Zoeppritz equation. Aki and Richards followed this approach and derived a formula with simple parameters regarding the changes in density (ρ), *Vp* and *Vs* (Castagna and Backus, 1993). Then, Shuey (1985) did another approximation of the Aki and Richard's. He rearranged the equation, so that it could be expressed from three simple terms

$$R(\theta) = R(0) + Gsin^2(\theta) + F(tan^2\theta - sin^2\theta), \tag{3.33}$$

where

$$R(0) = \frac{1}{2}\left(\frac{\Delta V_P}{V_P} + \frac{\Delta\rho}{\rho}\right), \tag{3.34}$$

$$G = \frac{1}{2}\frac{\Delta V_P}{V_P} - 2\frac{V_S^2}{V_P^2}\left(\frac{\Delta\rho}{\rho} + 2\frac{\Delta V_S}{V_S}\right), \tag{3.35}$$

and

$$F = \frac{1}{2}\frac{\Delta V_P}{V_P}. \tag{3.36}$$

This approximation is divided into three parts, where $R(0)$ describes the normal incidence reflection coefficient. G is the dominating part for intermediate angles and the third term F is the dominating term when the critical angle is approached (Avseth and Bachrach, 2005). It is rarely done seismic surveys with ranges of angles greater than 30-40°, so the last term in Equation 3.33 is neglected in this study. Which leaves the Shuey's two-term AVO equation.

Application of AVO data

AVO is a good technic for finding amplitude anomalies as a result of gas-filled reservoirs. There is a wide range of AVO types, so Rutherford and Williams (1989) published a paper that classifies the different AVO-responses. They presented three different AVO effects typically faced during seismic exploration; class 1, class 2 and class 3. Later, Castagna and Swan (1997) added a fourth class to the classification scheme (see Figures 3.9, 3.10 and 3.11), and they are described as following:

I. AVO Class I – This class is plotted in the fourth quadrant because of its positive R (0) and negative gradients. The sand in this class has high impedance and a low *VP*/*VS*-ratio compared with the overlying cap rock. As seen in Figure 3.9, the reflection coefficient decreases with increased offset. Class 1 is commonly found in highly compacted sandstone, deposited in onshore environments (Rutherford and Williams, 1989).

II. AVO Class II – Class 2 is represented by sand with a weak reflection coefficient and a strong negative gradient, making them hard to see when dealing with seismic (dim spots) for small incidence angles. The weak reflection coefficient is a result of similar impedance in both the reservoir and cap rock. The sand in this class is common for both offshore- and onshore sands (Rutherford and Williams, 1989, Avseth and Bachrach, 2005).

III. AVO Class III – This sand has a lower impedance than the overlying shales. Resulting in a largely negative response for all offsets; normally associated with bright spots. The reflectivity decreases slightly with an increase in offset. These sands are usually related to marine environments (Rutherford and Williams, 1989, Avseth and Bachrach, 2005).

IV. AVO Class IV –This class represents soft gas-filled sands capped by a stiff rock. This gives a low impedance with a positive gradient as seen in Figure 3.9 and Figure 3.10.

V. AVO Class VI – This AVO-class is presented by Goodway et al. (2008), where it is used as a way to discriminate between GWC and mineralogical changes (Figures 3.11A and B). The method is relatively new and is an AVO-analysis of the GWC. It is placed in the 1st quadrant, with both a positive gradient and intercept. In "classical" AVO this class is not used or defined. The results are in the 1st quadrant because gas in the top of the reservoir makes the top stiffer than the brine-filled lower reservoir. From this, it should be possible to distinguish between mineralogical changes and fluid changes in the reservoir. This is becuase a GWC would change the *Vp*, but keep the *Vs* unchanged, while a mineralogical change would affect both *Vp* and *Vs*.

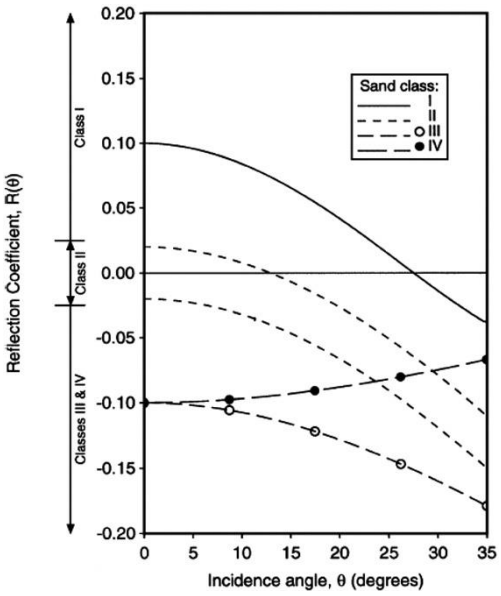

Figure 3.9 - Rutherford and Williams (1989) AVO-intercept classification scheme.

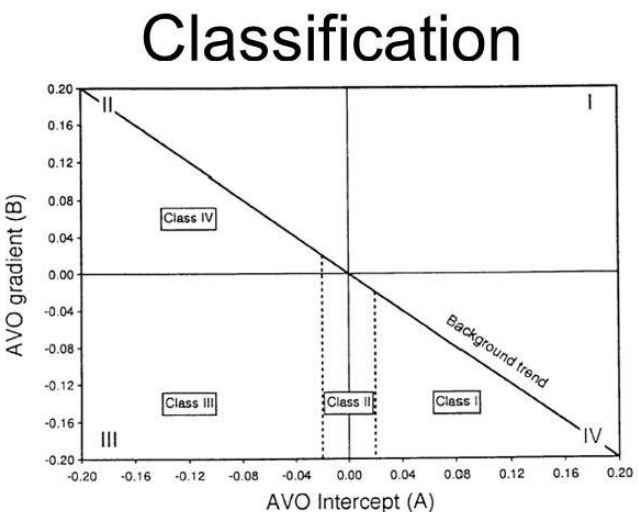

Figure 3.10 – Cross plot of AVO intercept and gradient used as a classification of gas sands (Rutherford and Williams, 1989).

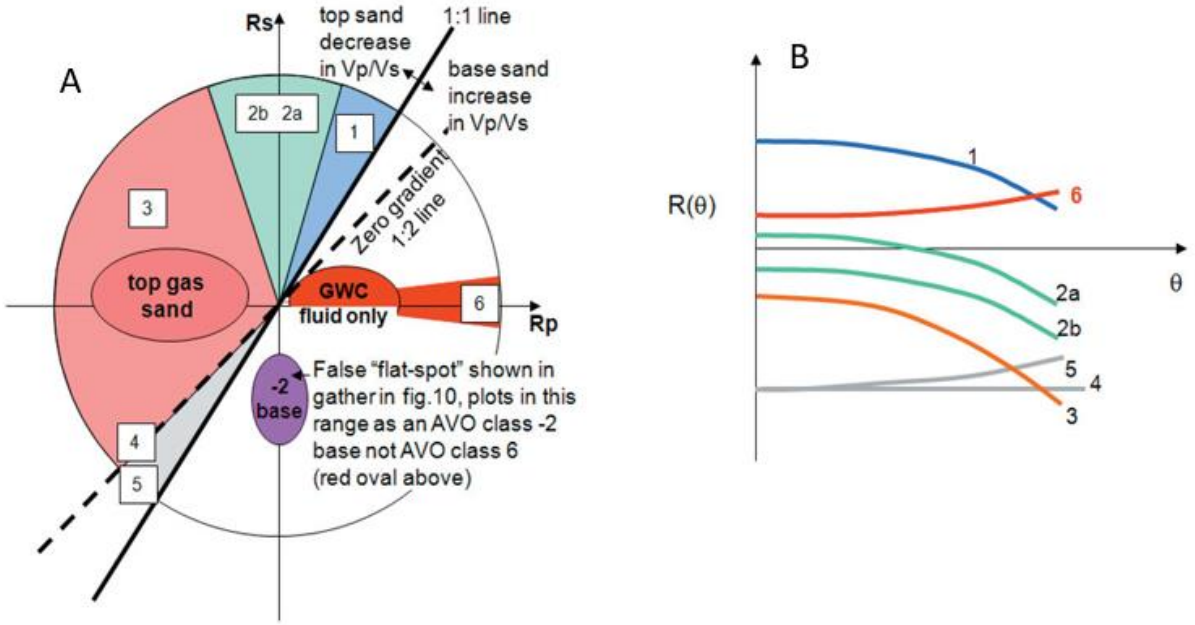

Figure 3.11 – A) shows Rp versus Rs and the AVO classes for gas sand. The 6th AVO class is for the GWC. B) displays the AVO curves for the different classes (Goodway et al., 2008).

Chapter 4: Application – a Barents Sea example

In this section, the application and database for burial effects, rock physics modeling, and AVO-modelling is presented, respectively. The database for the study is shown in each of the sub-chapter.

4.1 Burial and uplift effects

Uplift in the Barents Sea is a key factor for the understanding of reservoir properties in the area. The maximum burial depth is an important factor because it can tell if the area of interest has reached the chemical compaction regime. To make an estimate of the maximum burial and the amount of uplift it is useful to compare the well data to experimental *Vp*-depth trends. For this thesis, the experimental compaction curves from Japsen (2006) and Storvoll et al. (2005) is used. Steps used for uplift estimation:

1. Calculate the transition zone from mechanical to chemical compaction regime using the different theories in chapter 3, for example, the *Vp*-depth trend and porosity-shear modulus trend.
2. Sort the well data for shale to find the velocity data for pure shale (volume of shale bigger than 75 % is used) to compare with the different compaction trend lines for shale. This is to see if the sandstones have a higher velocity than the trendlines because of a deeper burial in the past. Moving the velocities to fit the trendlines, could give a good estimate of the net uplift.
3. It is also important to find the temperature gradient, for the calculation of the transition zone at the 70 °C point.

The reference well in this study is the 7324/2-1-well for the Apollo prospect and is chosen because the primary target for the well was the Stø formation and the reservoir was water wet (NPD, 2016a). In this well, the Stø formation was encountered at 849 meters depth. The reservoir had clean sandstones from 857 meters and down to the top of Fruholmen formation at 871 meters. This well does also have direct measurements for several important rock physics parameters, such as the shear wave velocity.

4.2 Rock physics modeling

For the rock physics modeling in this thesis, it is used various theories and approaches. The physical properties of fluids and minerals used in the modeling are presented in Table 4.1. The density and bulk modulus for brine and gas are estimated using the Batzle and Wang (1992) and Han and Batzle (2004) model.

Depths for each point in the burial history, for the Stø formation, is found (NPD, 2014) and Ohm et al. (2008) burial history for the Barents Sea. Using today's depth as a reference and estimate the burial history from this point results in the burial history in Figure 4.1A. Porosity estimations for each of the depths in the mechanical compaction domain are found using empirical relationships between porosity and burial depth. For the uplift domains, it has been modeled an increase in porosity due to cracks. In the chemical domain, there is added a porosity decrease at 3 % due to cementation, Figure 4.1B. The rock physics modeling has been done using 100 % brine saturation and 100 % gas saturation, to give a better understanding of the extremes of fluid substitution.

Table 4.1 – Physical properties of fluids and minerals used in the rock physics modeling.

Mineral/fluid	*Density (g/cm^3)*	*Bulk moduli (GPa)*	*Shear moduli (GPa)*
Quartz	2.65	37.0	44
Clay	2.60	21	7
Brine	1.01	2.78	-
Gas	0.16	0.035	-

To best describe the changes during the burial history, the complete burial history has been divided into different burial scenarios (Figure 4.1A):

1. Period A – From burial depth 2 to uplifted point 3.
2. Period B – From the uplifted point 3 down to point 4 before cementation.
3. Period C – From the uplifted point 3 to point 5.
4. Period D – From point 4 to point 6, before and after chemical compaction.
5. Period E – From maximum burial depth (5) to today’s depth (9).

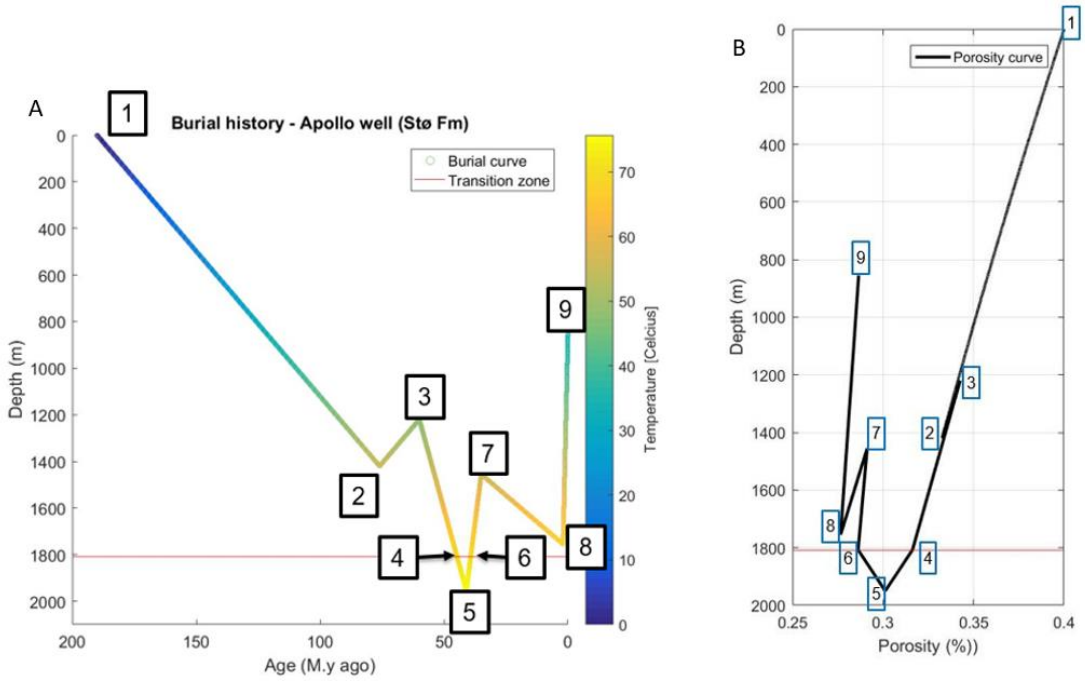

Figure 4.1 – (A) is the burial curve for the Stø formation, and (B) is the coherent porosity evolution for the sandstone.

Well, 7324/2-1 is used for the rock physics modeling as well, and the Stø formation is used for depths from 857-871 meters (marked orange in Figure 4.2) due to the further investigation of sandstone formations. From the well logs, it is also possible to see that there is an increase in both *Vp* and density at approximately 863 meters. Due to calibration for the Apollo well it has been added a shale volume fraction of 2 % in the modeling.

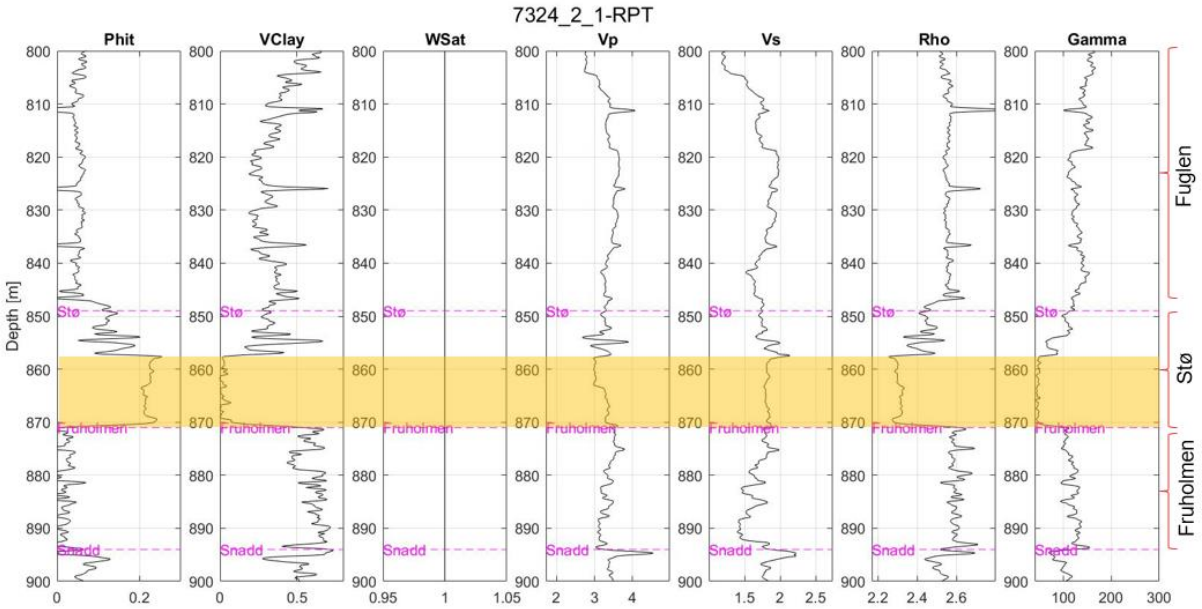

Figure 4.2 – Composite log plot for the 7324/2-1 well. This section displays the changes from 800 to 900 meters depth (covering the Stø formation, colored orange).

Several input parameters changes during the burial history and they need to be defined for the modeling. These parameters are displayed in Table 4.2, and explained below:

- Critical porosity is defined as the upper limit the rock can have in a certain setting (Yin et al., 1993).
- Pore pressure for each period is calculated from Terzaghi's principle (Skempton, 1960).
- The temperature is found from the geothermal gradient in the Apollo well.
- Relaxation number is a calibration parameter that is set to 0,3 for every period. The relaxation number is used to prevent the modeling from overpredicting the stiffness of the rock properties.
- Coordination number is a measurement of the number of average contact points per grain (Avseth et al., 2014). For each period, this number has been calculated from (Murphy, 1982).
- The uplifted periods have been modeled using the kite-model where it is possible to implement cracklike pores. The aspect ratio is a method for adding cracklike pore structures in the sand, for cracklike pores one uses aspect ratio at 0,01, and then the $\phi_{max,\ DEM} = 0{,}02$.
- The aspect concentration describes how many percentages of the cracks that have the given aspect ratio and is put to 1,0 in the uplift periods.
- $\Delta\phi_{CCT}$ is a measurement of the volume fraction of cement. This volume is calibrated to be 0,002 for the cemented points in the burial history.

The different rock physics models used for the different periods varies due to geological processes like cementation and uplift:

Point 2 at 1420 meters depth describes the first event; from deposition to approximately 1420 meter's depth in the mechanical compaction regime. The model used is Dvorkin and Nur (1996) friable sand model. This model is used because the compaction at this point in the history is mechanical driven and the sand is unconsolidated.

The third point represents the sandstone at 1220 meters, after a 200 meters uplift from point 2. Modeling of this position is done using a modified kite model, where the CCT-model for low porosity is replaced with Hertz-Mindlin contact theory. This modification is done because the sandstone is uncemented at this point in the burial history, and the CCT-model assumes cementation. The kite model is used to implement cracklike pores in the sandstone at

uplift, although it is debatable whether the sandstone is too loose to experience cracks. The relatively high temperature and pressure at point 2 combined with burial for over 100 Ma years, it is assumed here that the sandstone experience cracks when uplifted. The critical porosity is increased 1,1% due to the uplift due to the cracks.

Point 4 models the elastic properties from deposition and down to 1808 meters using the friable sand model. This is done without considering point 3 and the uplift. At this point, the sandstone has only been exposed to an increase in both pressure and temperature, and the friable sand model is chosen here as well.

The maximum burial at 1950 meters depth (point 5) is modeled using the constant-cement theory. This model is used because the sandstone at this point is in the chemical compaction domain, and the cementation has started. The cementation reduces the critical porosity further and is in this period reduced by 1,5% from point 4 to point 5.

Point 6 is also in the chemical compaction domain, and the constant-cement theory is used here. This point is uplifted from point 5 but is still in the chemical compaction regime. That means that the uplift does not cause cracks, due to the relatively high temperature (Ehrenberg, 1990, Walderhaug, 1994). So, the difference between this point and point 5 is some reduction in critical porosity, temperature and pore pressure, and an increased coordination number (see Table 4.2).

The last point (9) represents today's depth at 857 meters depth. Here the kite model is used as described by Avseth et al. (2014). The CCT-model includes the cemented part, and aspect ratio adds cracklike pores in the sandstone. The porosity is modeled to be the same as for point 6, due to a small uplift and burial (point 7 and 8).

Point 7 and 8 are only used for porosity estimations; they are not modeled for elastic properties because they are not re-cemented. This is because the Stø formation is above the chemical compaction regime after the sixth point.

Table 4.2 – The Table displays the different points for the rock physics modeling. It shows the depths for each point, the model used, and the various input parameters used.

Parameter	*Point 2*	*Point 3*	*Point 4*	*Point 5*	*Point 6*	*Point 9*
Depth	1420 m	1220 m	1808 m	1950 m	1808 m	857 m
Model used	Friable sand model	Kite + Hertz-Mindlin	Friable sand model	CCT	CCT	Kite model
Critical porosity	33,2 %	34,3 %	31,6 %	30,1 %	28,6	28,6 %
Pore pressure	14,2 Mpa	12,2 Mpa	18,1 Mpa	19,5 Mpa	18,1 Mpa	8,49 Mpa
Temperature	55 °C	47 °C	70 °C	75,5 °C	70 °C	33,2 °C
Coordination number	9.9885	9.7214	10,4157	10,5760	11,5596	11,2610
Aspect ratio	-	0,01	-	-	-	0,01
Aspect concentration	-	1,0	-	-	-	1,0
$\phi_{max,DEM}$	-	0,02	-	-	-	0,02
$\Delta\phi_{CCT}$	-	-	-	0,002	0,002	0,002

Rock physics templates

A rock physics template has been modeled for the defined periods. They are presented in a *Vp*/*Vs* versus acoustic impedance (AI) cross plot, as seen in Figure 4.3. These types of plots were introduced by Ødegaard and Avseth (2003), and are widely used today for lithology, porosity, and pore fluid interpretation.

From Figure 4.3, it is possible to see that brine saturated sands have a high *Vp*/*Vs* ratio at high porosity, due to the low shear modulus. Increased burial decreases the *Vp*/*Vs* ratio rapidly, and the AI increases as grains gets packed together and cemented. Also, both AI and *Vp*/*Vs* decreases when the gas saturation increases.

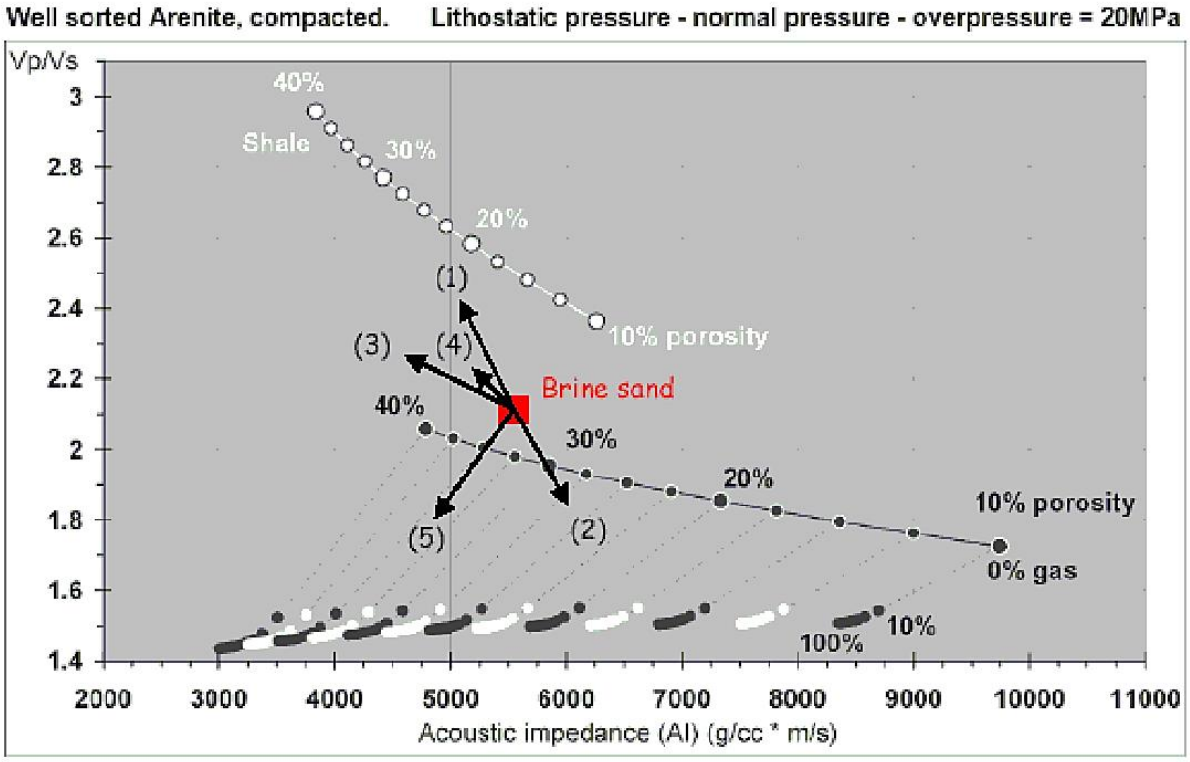

Figure 4.3 – Cross plot of the *Vp*/*Vs* versus acoustic impedance for brine sand. There are five different trends presented by Avseth et al. (2010): (1) increasing shale volume, (2) increased cementation, (3) increased porosity, (4) increased burial, and (5) increased gas saturation. In addition, the results from this thesis shows that cracks trend line for brine sands moves in the direction of the blue arrow.

4.3 AVO-modelling

The database for the AVO-modelling is the elastic properties for each defined period in Chapter 4.1. The AVO-modelling is done for each point to see how the seismic signatures change for the sandstone reservoir during the burial history. Also, it has been done AVO-analysis of the in-situ period in the reservoir, and an AVO-analysis for the gas-water contact in the reservoir (Figure 4.4).

For the various parts of the burial history, the porosity of the reservoir is found using the porosity-curve for each period, and calibrated for the in-situ reservoir. This gives the *Vp*, *Vs*, and density presented in Table 4.3 for the different periods with 100 % gas- and 100 % brine fill. The top layer for the AVO-model is the shaley Fuglen formation, and the *Vp*, *Vs*, and density are found from the well data. The shaley cap rock is assumed to be a low-porosity shale, and should, therefore, experience minor changes during the burial history. Keeping it constant is a simplification, but makes it easier to observe variations in the sandstone reservoir. The AVO-modelling is done for 100 % brine and 100 % gas saturated sandstones. Avseth et al. (2010) made a schematic figure for AVO responses for cemented and uncemented sandstone, with different saturations (Figure 4.5). These trends are used to check the validity of the trends in this study.

For the modeling of today's situation, the AVO results are based on the well data. Where it has been used *Vp*, *Vs*, and density for the Fuglen formation as cap rock, and the *Vp*, *Vs* and density for the Stø formation with 1 % gas and 99 % brine.

For the AVO-modelling in this study, Shuey's approximation is used for all the scenarios. The approximation is chosen because it is the overall most used approximation, and is valid for incidence angles up to 30 degrees (Feng and Bancroft, 2006). Therefore, the modeling has only been done for incidence angles up to 30 degrees.

The AVO-analysis of the gas-water-contact (Figure 4.4), uses input from the 7324/2-1-well. This is done for the in-situ period with 1 % gas in the top of the reservoir and then compared to different higher saturations (for 50 % and 100 % gas saturation), to see if it is possible to distinguish between low gas saturations and higher saturations. Shuey's approximation is used here as well. The AVO-modelling of the

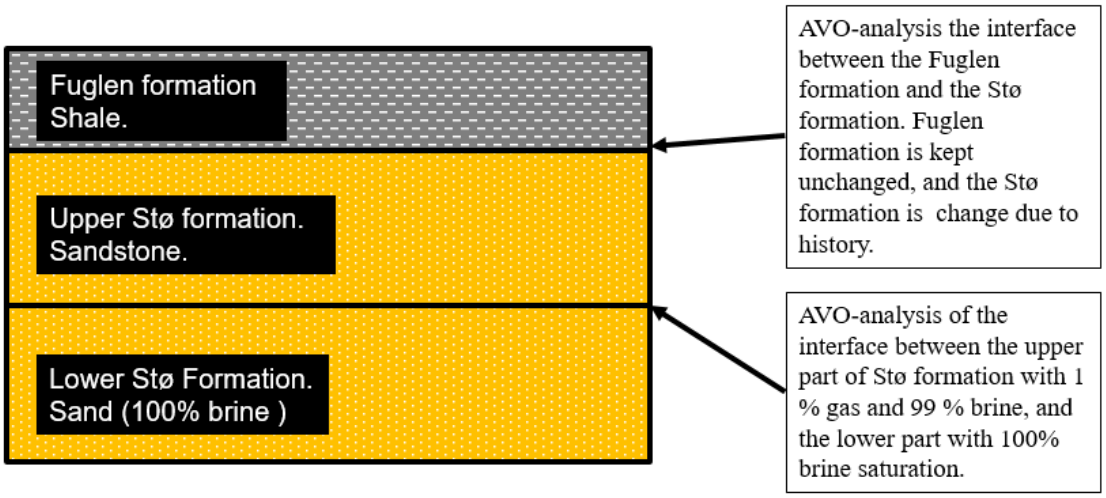

Figure 4.4 – The different interfaces used for the AVO modeling, between the cap rock and top reservoir and the GWC.

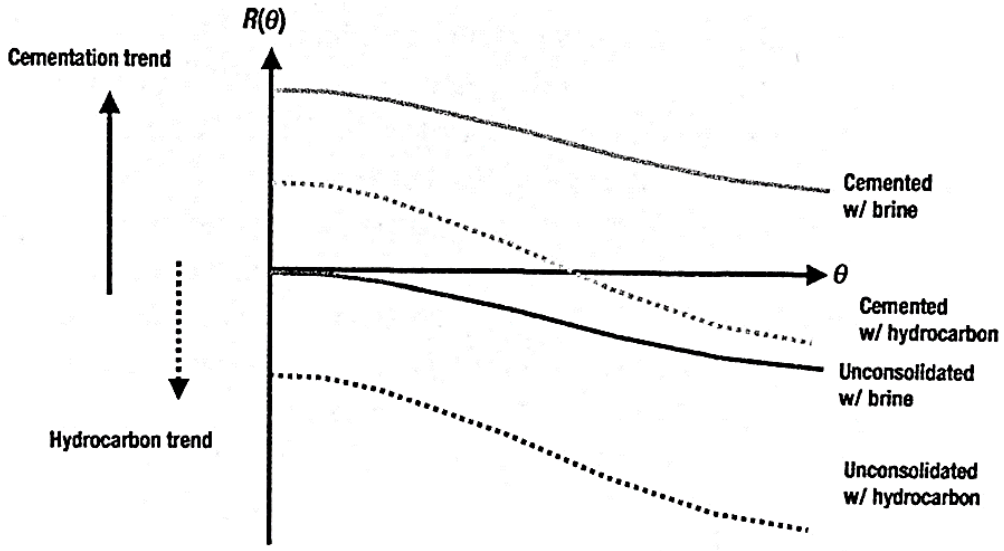

Figure 4.5 – AVO trends when comparing uncemented and cemented sandstones, with brine and gas saturation (Avseth et al., 2010). Here, R(Θ) is the intercept and Θ is the gradient.

Table 4.3 – Table of input for the AVO-modelling. The porosity, *Vp*, *Vs* and density for each of the periods are displayed.

		100% brine filled sandstone			*100% gas-filled sandstone*			*Top layer (shale)*		
Parameters	**Por. (%)**	***Vp* (km/s)**	***Vs* (km/s)**	**Density (g/cm^3)**	***Vp* (km/s)**	***Vs* (km/s)**	**Density (g/cm^3)**	***Vp* (km/s)**	***Vs* (km/s)**	**Density (g/cm^3)**
Point 2 (1420m)	26,6	2,51	1,10	2.23	1,76	1,04	1.99	3,35	1,73	2.54
Point 3 (1220m)	27,7	2,45	0,99	2.22	1,68	1,06	1.96	3,35	1,73	2.54
Point 4 (1808m)	25,0	2,60	1,11	2.26	1,87	1,17	2.04	3,35	1,73	2.54
Point 5 (1950m)	24,0	3,35	1,85	2.27	3,08	1,94	2.06	3,35	1,73	2.54
Point 6 (1808m)	22,5	3,40	1,88	2.3	3,12	1,97	2.1	3,35	1,73	2.54
Point 9 (855m)	22,5	3,28	1,80	2.29	2,96	1,90	2.06	3,35	1,73	2.54

Chapter 5: Results

This chapter is divided into three sub-chapters, where the first part presents burial and uplift results. The second part, the rock physics modeling results, and the last part displays the results for the AVO-modelling.

5.1 Burial and uplift effects

5.1.1 General trends for the Apollo well

Several well log properties are closely linked together and have general depth dependent trends (when having a constant pore and fluid pressure). For instance; the density, *Vp*, and *Vs* increases, while the porosity decreases, with depth.

Figures 5.1A and b display how various parameters change in the well. From left to right; the porosity, volume clay, water saturation, pressure wave velocity, shear wave velocity, density and gamma ray are shown, respectively. These logs are direct measurements from the well log, except for the porosity and saturation. The porosity log is calculated from the density log, and the saturation log is set to 100 % water saturation due to the "dry well-announcement" from NPD (2016a). In Figure 5.1A the complete well is displayed, and Figure 5.1B is zoomed in on the orange area in Figure 5.1A to better display the Stø formation. The relevant formations for this thesis are labeled in the logs.

In the Figures 5.1A and B, there is a general trend for increasing *Vp* with depth, and the density increases slightly. There are some anomalies from these trends, and these may be due to a local change in lithology, fluids and/or pressure. The gamma ray log is used to see if anomalies can be related to lithological changes. The well displays relatively low velocities for smaller depths. There is also a change in the velocity gradient at approximately 700 meters depth. The change in velocity gradient is not lithology dependent, due to the stable trend for gamma ray over the area. Therefore, one could potentially connect the change to the transition zone. The *Vp*-gradient below the transition zone is lower than the one above. Just below the transition zone, the gamma ray log increases, and the *Vp* decreases for approximately 2 meters. This is probably due to the Hekkingen formation, the source rock in the area consisting of mostly shale (NPD, 2014).

The gamma ray log shows a slightly decreasing trend in the well but varies still a bit randomly due to variations in lithology. Although, it does reveal several lithological features like the Hekkingen Formation (approximately at 750 meters depth), with an anomalously high gamma ray response. It also shows a very low response for the Stø formation, because of the clean sandstone in the formation. This correlates well with the small volume of clay in the Stø formation and the relatively high porosity.

The general density for the log is around 2,5 g/cm^3. For the Stø formation, the density has an anomalous low response due to the lower density for sandstones than for shales.

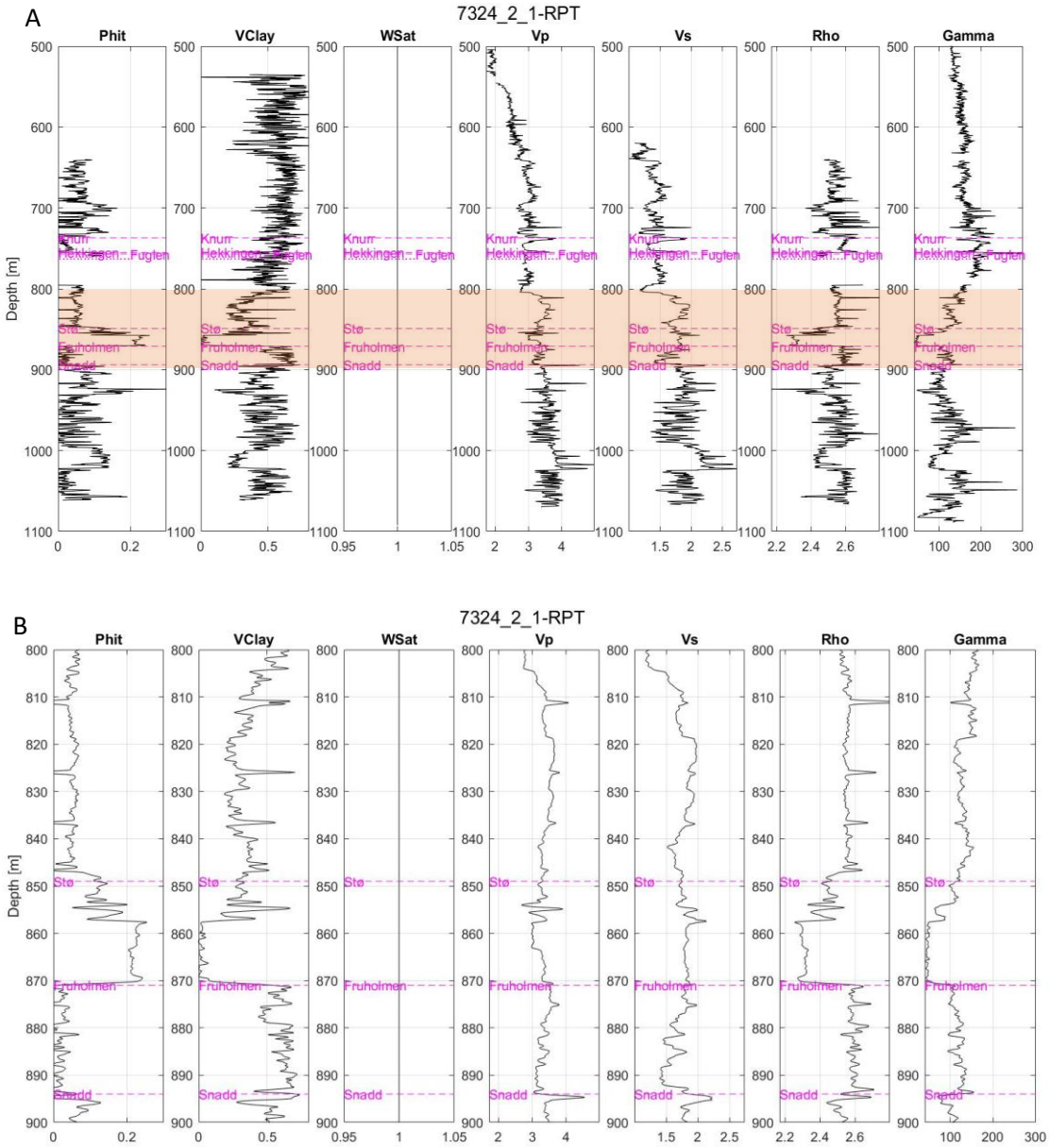

Figure 5.1 – (A) displays the complete 7324/2-1 well log, and (B) displays the orange area in the complete well (from 800-900 meters depth).

5.1.2 *Vp*-depth trends for the 7324/2-1 well

The general trend in the well is an increase in *Vp* with depth. There is a clear change in velocity gradient in the well at around 700 m below seafloor (BSF) (Figure 5.2). This change could be related to the transition zone between mechanical and chemical compaction. The transition from the 1st to the 2nd trend line corresponds to the maximum burial depth (point 5 in the burial history), leaving the transition zone.

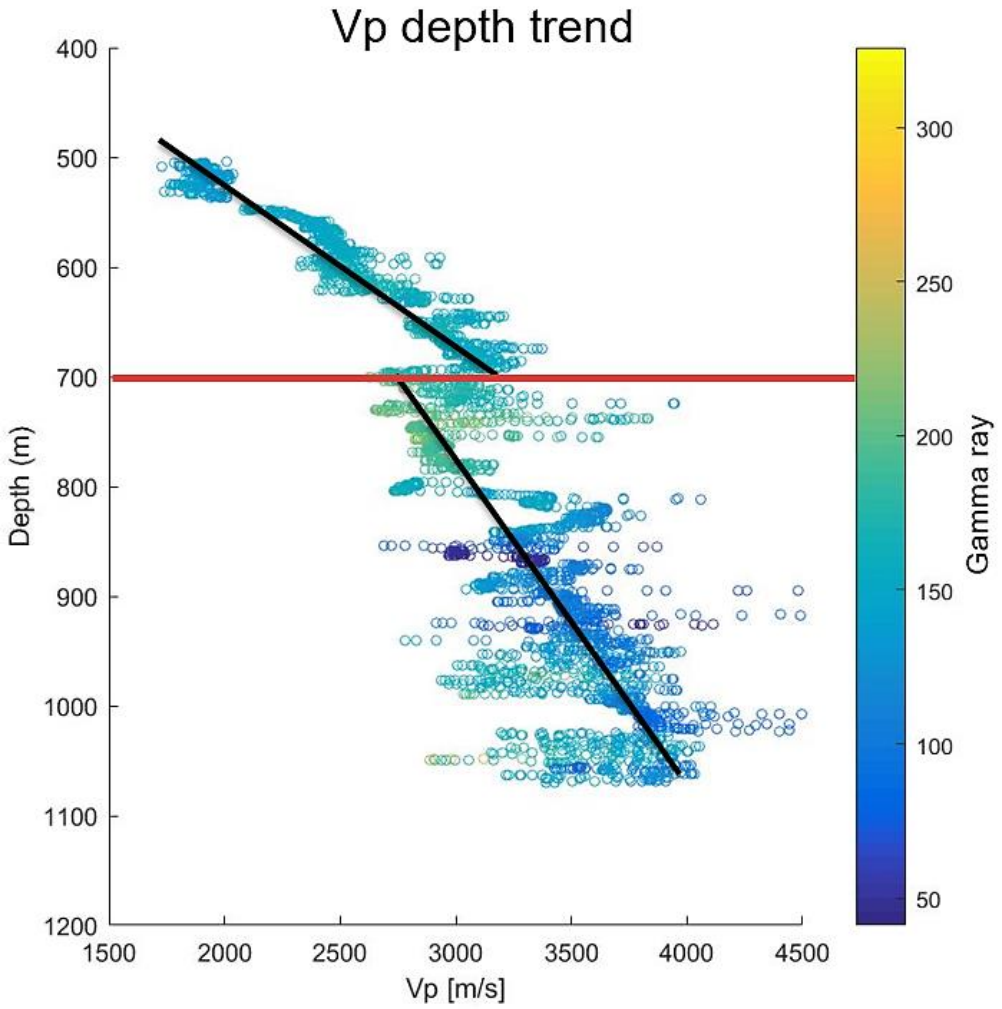

Figure 5.2 – Cross-plot for *Vp* versus depth for the 7324/2-1 well. The figure displays two different trendlines, and the well data are plotted with gamma ray response as color.

5.1.3 Transition zone: from mechanical to chemical compaction

From chapter 5.1.2 one can define an approximate transition zone at 700 m BSF. This is based on the change in velocity gradient, that is not lithology dependent.

For further investigation of the transition zone, a shear modulus versus porosity cross plot has been made (Figure 5.3) for the well data were pure sand is filtered out (for volume of shale > 30 %). The cross-plot shows two different clusters, where the blue circle gives the depths down to approximately 700 meters and the yellow is for depths larger than 700 meters. From this, it is possible to sort out the shallow (<700 meters) trends and the deeper trends (>700 meters). This shows a change in trends between the cemented part (yellow circle) and the uncemented part (blue circle) of the well.

The transition from mechanical to chemical compaction at 700 meters correlates with Figure 5.2. A closer look at Figure 5.3 does also reveal that the transition happens when the porosity has been reduced to approximately 35 %, and the shear modulus is around 6 GPa. Another observation is that the porosity decreases continuously in both the mechanical and chemical regime, and the shear modulus increases most in the chemical compaction regime.

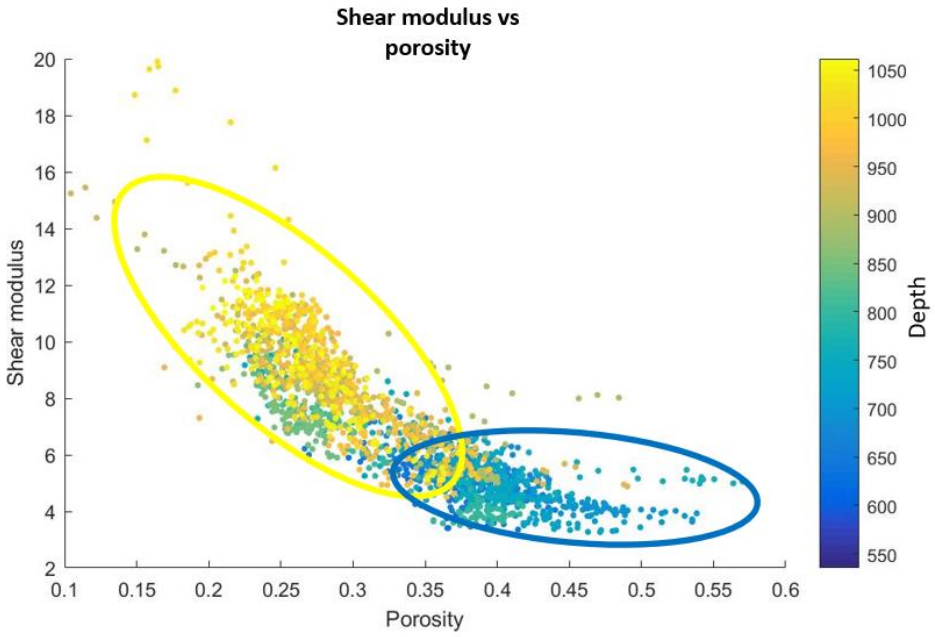

Figure 5.3 – Cross-plot for porosity versus shear modulus for the well data. It is possible to see two different trends, marked with circles. The blue circle represents the data to approximately 700 meters and the yellow depths deeper than approximately 900 meters. The color-coding is the depth.

5.1.4 Temperature gradient

For the Apollo well, the bottom hole temperature is at 29 °C at a depth of 1090 m (NPD, 2016a). The seafloor temperature is approximately 3 °C; this gives a geothermal gradient of 38,7 °C/km in the area around the well. The bottom hole temperature registered in the well is often lower than the real temperature due to the cooling drilling mud. Still, the result shows an adequate agreement with other studies in the Barents Sea. The temperature at 700 meters is at 27.9 °C. The transition from mechanical to the chemical regime (70 °C) should start at approximately 1808 meters depth, based on the geothermal gradient.

5.1.5 Uplift estimation

The *Vp*-depth plot in Figure 5.4 is plotted for shale velocities (volume of shale > 75%) and then compared to different empirical curves. Figure 5.4A shows the shale velocity in the well without uplift corrections, and the deviation between the experimental velocity trends and real data is significant. This difference can potentially be explained by uplift (Japsen and Chalmers, 2000, Henriksen et al., 2011a). The amount of uplift can be estimated measuring the distance the well data needs to be moved to fit the experimental curves (Figure 5.4B). In this study, the points need to be moved down approximately 1100 meters before the trendline starts to fit the empirical curves. This gives an estimated net uplift of 1100 meters.

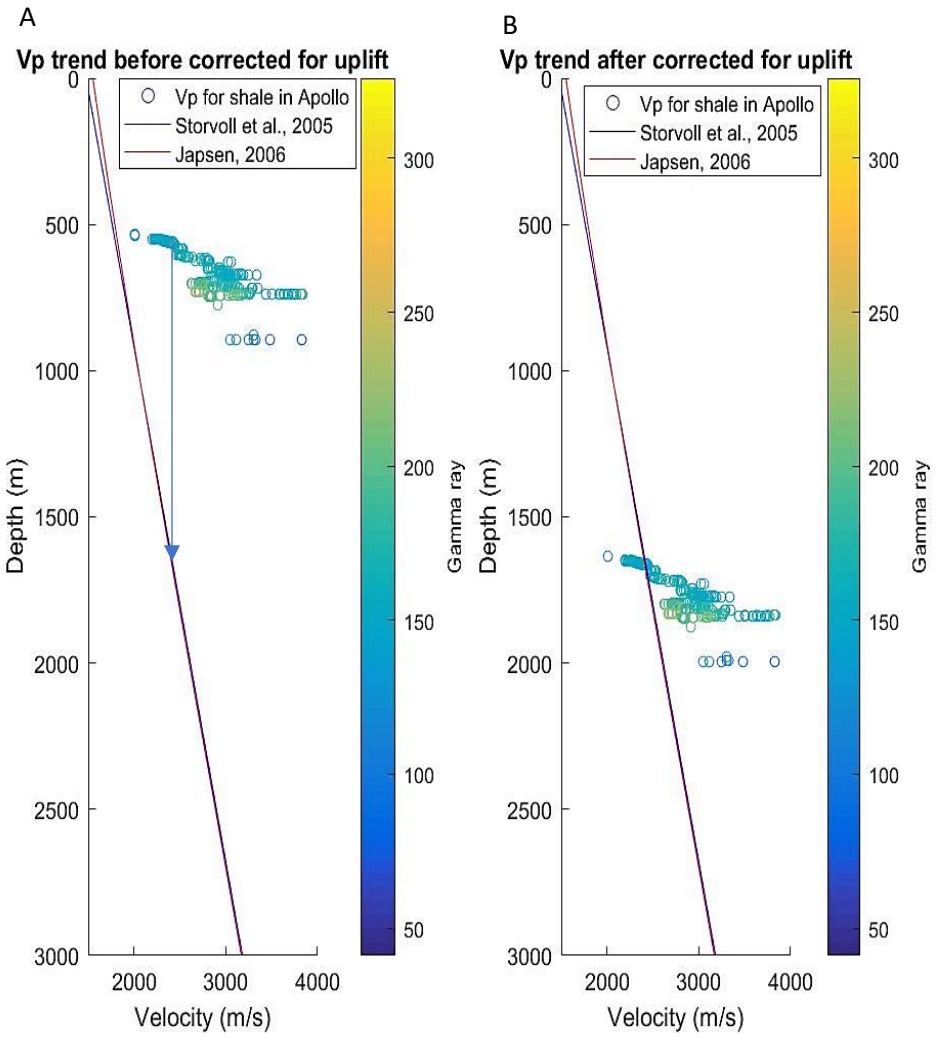

Figure 5.4 – Velocity-depth cross plot of shale (>75 %) in well 7324/2-1 before (A) and after (B) uplift correction.

5.2 Rock physics modeling

This section is present discussions for each of the various vertical displacement periods. In addition, the model for point 9 is compared to the well data for 7324/2-1.

5.2.1 Period A

Figure 5.5 shows the results for the rock physics modeling for point 2 (at 1420 meter's depth) and point 3 (at 1220 meter's depth), giving an idea of change in properties of the sandstone during this uplift period. The red lines represent the uplifted model for both brine and gas saturation, and the black lines show the same for point 2 (before uplift).

At zero porosity, the two periods have the same values for both bulk and shear modulus and the velocity models. In the modeling, the mineral point at zero porosity is assumed to be unaffected by burial history because there is no fluids present and the mineral composition is equal for both periods. At the critical porosity point, the different results have similar values for both brine and gas saturations.

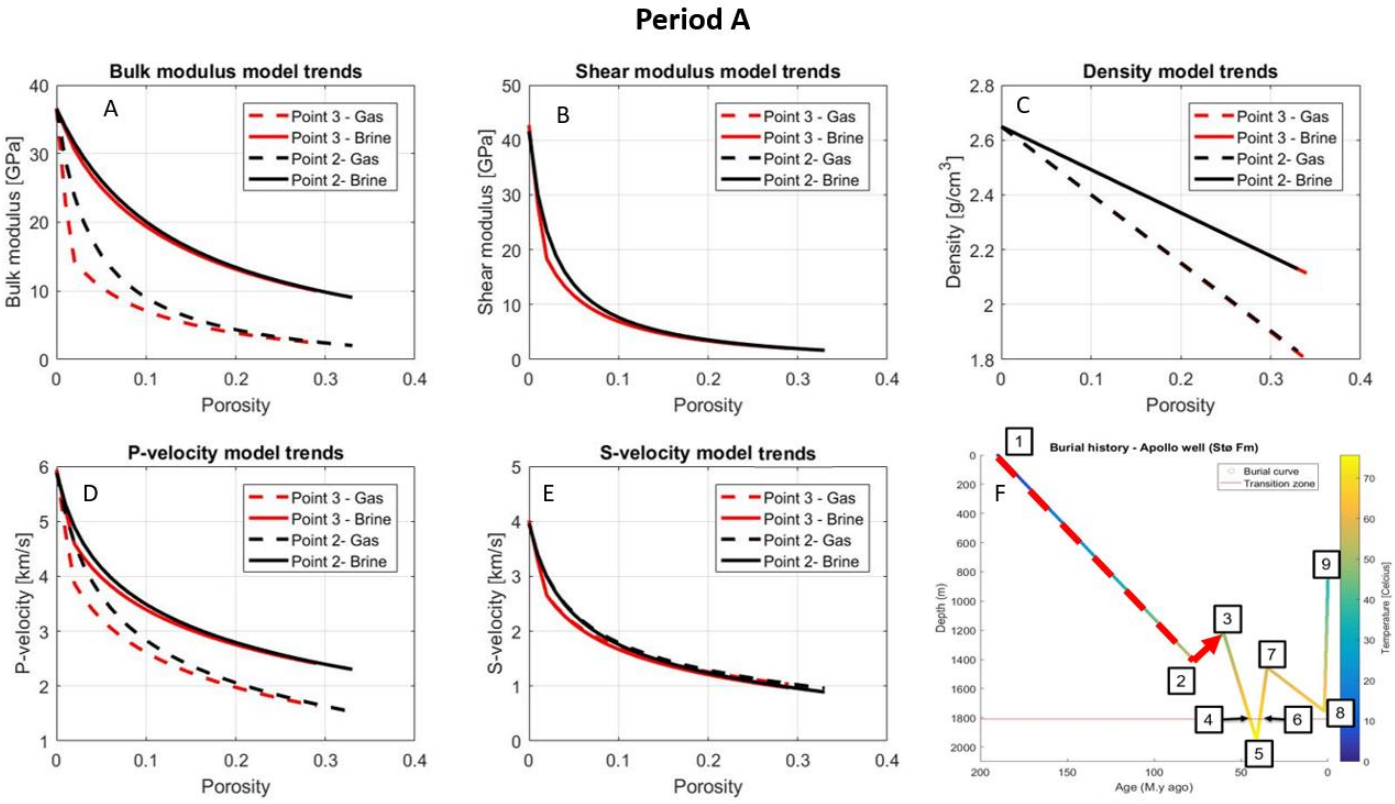

Figure 5.5 – Rock physics modelling for the 2nd and 3rd point in the burial model. The red lines represent the 2nd point, and the black lines are the 3rd point. The solid lines are brine saturation, and the dashed lines are gas saturation. The different plots describe the (A) bulk modulus, (B) shear modulus, (C) the density, (D) Vp, (E) Vs and (F) the burial history.

The bulk modulus is higher for point 2 than for point 3. One reason for lower values for the uplifted point is the modeling of the formation of cracks in this study. These cracks lead to a weakened structure of sandstones. Also, the temperature and pressure will be slightly lower at 1220 meters depth, leading to the lower bulk modulus. The bulk modulus shows that the sandstones are most fluid sensitive for low porosities, and at higher porosities the fluid effect is almost neglectable.

Fluids do not have a shear modulus, and the shear modulus is therefore fluid independent. That is the reason for only two distinct trends observable in Figure 5.5A, one for point 2 and one for point 3. The difference between these points is the lower shear modulus for the uplifted point, due to the weakened shear strength caused by cracks and lower temperature and pressure. There is also a slightly lower *Vs* for the uplifted period because of the lower shear modulus.

Density as a function of porosity shows the same for both points. Still, the uplift would make the density slightly lower, but this cannot be seen in the plot due to the changes in density as well.

The pressure wave velocities show many of the same trends as the bulk modulus. The velocity is slower for the sandstone that has experienced uplifted and cracking. Gas saturated sandstones have lower velocities than the brine filled for both periods. As for the bulk modulus, the difference for gas saturated sandstone is bigger than for brine saturated.

5.2.2 Period B

Period B gives an overview of changes in sandstones properties for point 3 and 4, Figure 5.6. The red lines represent point 3, and the black lines point 4. Dashed lines are gas filled sandstone, and solid lines are brine filled.

For the mineral point and the critical porosity, the two different depths have similar trends for bulk modulus, shear modulus, *Vp*, and *Vs*. This is caused by the use of friable sand theory at critical porosity, and for the mineral point the values represent the pure mineral.

The increased bulk modulus at point 4 is caused by the increase in temperature and pressure. The trendlines show that the bulk modulus has a larger fluid sensitivity at point 3 than point 4.

Shear modulus does not change significantly compared to the further burial in mechanical compaction domain (point). For lower porosities, the difference is observable, where point 3 is a bit softer than point 4, but it is still an insignificant change.

The density is unchanged, due to the same mineralogical composition for both burial depths. The fluid substitution is the reason for the two different density trends in Figure 5.6.

Pressure wave velocity shows much of the same pattern as the bulk modulus; higher velocities for the deepest buried point for both brine- and gas saturation. Further, the difference between the gas saturated periods is bigger than for the brine filled.

Shear wave velocity displays a small difference between the two burial depths, and there is practically no difference between gas and brine saturation. Point 3 has a bit lower velocity than the deeper buried point 5.

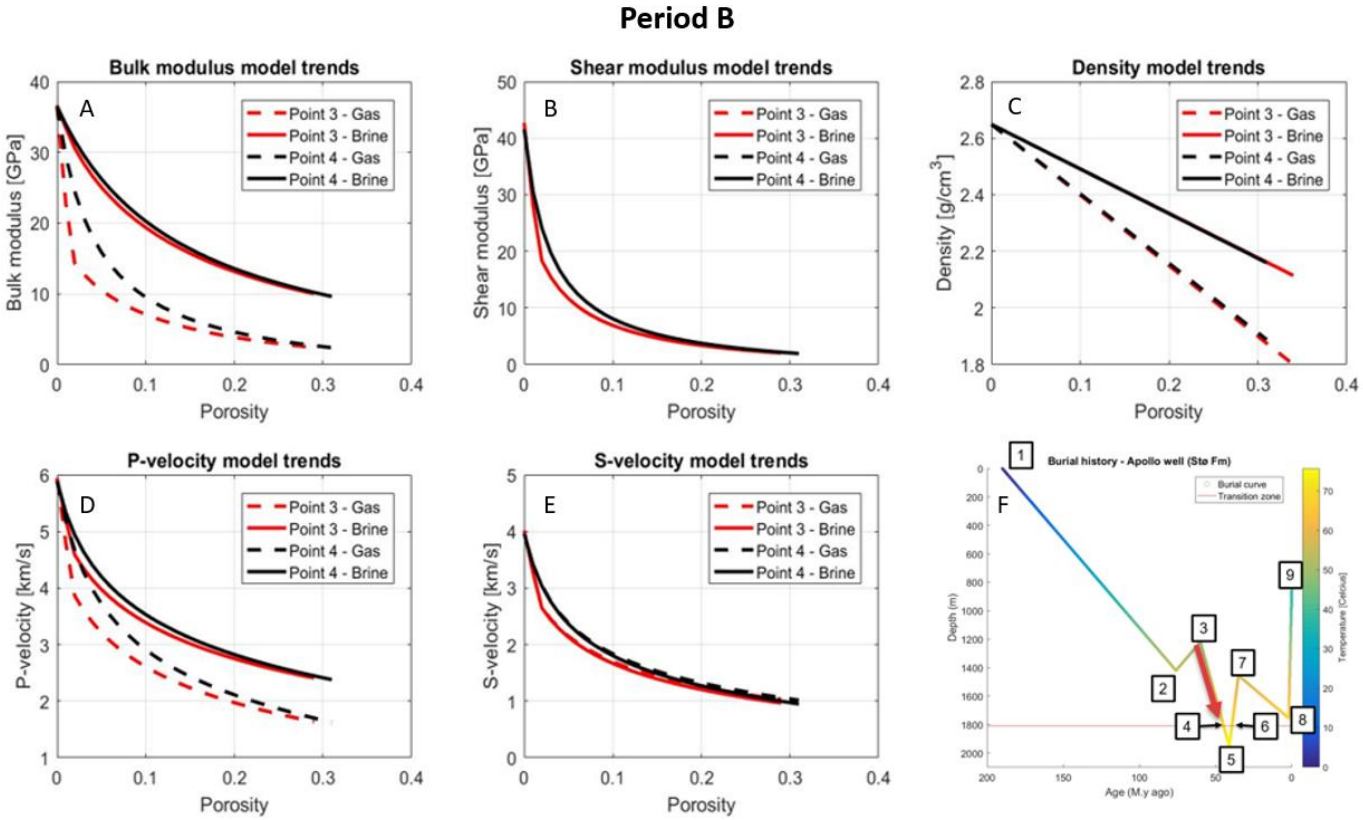

Figure 5.6 – Rock physics modelling for the 3rd and 4th point in the burial model. The red lines represent the 3rd point, and the black lines are the 4th point. The solid lines are brine saturation, and the dashed lines are gas saturation. The different plots describe the (A) bulk modulus, (B) shear modulus, (C) the density, (D) Vp, (E) Vs and (F) the burial history.

5.2.3 Period C

The next step in the burial history is to investigate the change in rock properties from point 3 at 1220 meters to the maximum burial depth at 1950 meters (point 5). From point 3 the sandstone is further compacted in both mechanical and chemical compaction domain. The red lines in Figure 5.7 represent the third point and the black lines point 5.

The bulk modulus for the sandstone at 1950 meters is higher than the one at 1220 meters, for both saturations. This can be explained by an increased stiffness due to increased pressure and temperature, in addition to the onset of cementation below the transition zone (1808 meters depth). For the periods, the difference between the two gas saturations is bigger than the one for brine saturation.

The same trends can be seen for the shear modulus; the sandstone at 1950 meters is stiffer than the one at 1220 meter. The shear modulus is not affected by fluid substitution, and the stiffening of the shear modulus for the deepest period is caused by increased pressure and temperature and onset of cementation. This makes the sandstone stiffer by reinforcing the grain contacts (Avseth et al., 2000, Avseth et al., 2014).

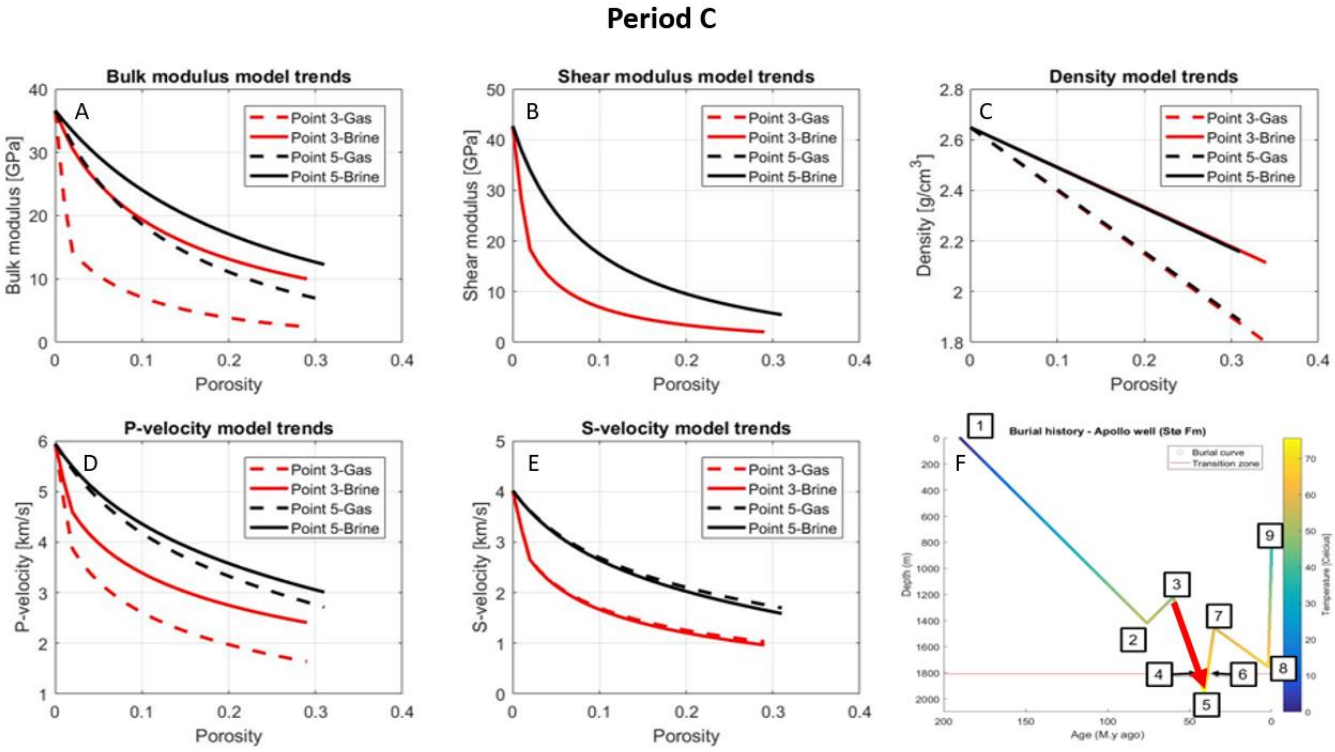

Figure 5.7 – Rock physics modelling for the 3rd and the 5th point in the burial model. The red lines represent the 3rd point, and the black lines are the 5th point. The solid lines are brine saturation, and the dashed lines are gas saturation. The different plots describe the (A) bulk modulus, (B) shear modulus, (C) the density, (D) Vp, (E) Vs and (F) the burial history.

The density trends for the periods are almost the same. This is because the density is mostly dependent on the mineral type and fluid type.

The *Vp* is still highest for the sandstone at 1950 meters (as a direct consequence of the same trends for the bulk modulus) for both gas and brine saturation. From Figure 5.7, it is also easy to see that both change in fluid and burial depth, results in great changes in the velocity.

For the *Vs*, it is observable that the velocity is higher for the deepest period, and that the *Vs* is slightly fluid sensitive.

5.2.4 Period D

Here, the two periods at 1808 meter's depth (point 4 versus 6), one before chemical compaction sets in and one after the chemical compaction is investigated. This is done to see the effects of chemical compaction for sandstones in the Stø formation. In both points, the pressure and temperature are the same, making it easy to see how the cementation changes the rock properties of the sandstone.

Figure 5.8 shows the rock properties before cementation in red and the rock properties after cementation in black. The dashed line represents the gas saturated sandstone, and the solid is brine saturated.

Bulk modulus for the two periods shows that the cemented sandstone is stiffer than the one before cementation. This change is caused by the further decreases in porosity and cement filling in pore space.

The same trends can be observed for the shear modulus. There are two trends because the shear modulus is not sensitive for fluids, giving the same response for the brine and gas saturated periods.

The density for that same porosities is equal for both periods, due to the same mineral and fluids.

Pressure wave velocity shows similar trends; the velocities are higher for the cemented sandstone. This is a direct consequence of the stiffening of the sandstones due to cement, as for the bulk modulus. *Vp* is fluid sensitive for both periods, but more sensitive for fluid substitution before the chemical compaction starts.

The shear wave velocity shows a trend where the cemented period has a higher velocity than the uncemented. Further, gas saturated sandstone has a higher velocity than the brine saturated.

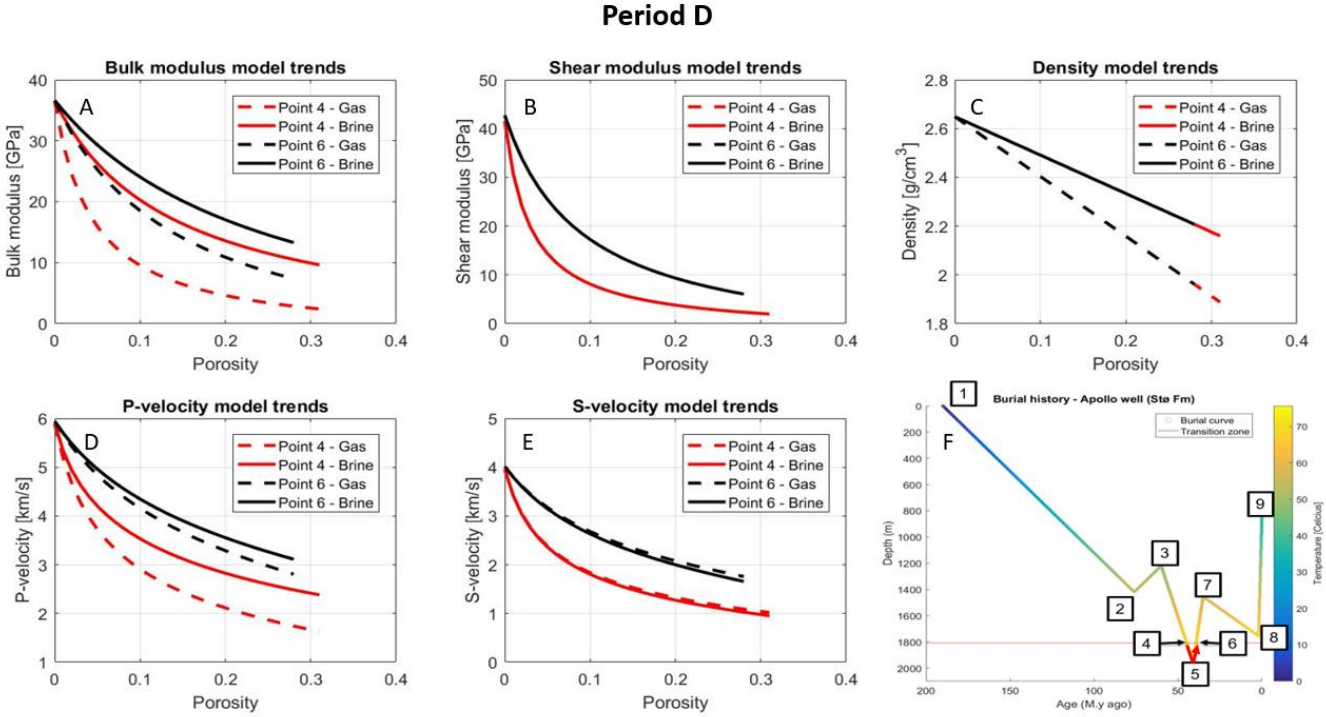

Figure 5.8 – Rock physics modeling for the 4th and 6th point in the burial model. The red lines represent the 4th point, and the black lines are the 6th point. The solid lines are brine saturation, and the dashed lines are gas saturation. The different plots describe the (A) bulk modulus, (B) shear modulus, (C) the density, (D) Vp, (E) Vs and (F) the burial history.

5.2.5 Period E

The results for the maximum burial depth (5) and today's depth (9) are displayed here. Figure 5.9 displays the rock properties for the two depths. The red lines represent the maximum burial depth, and the black represents point 9 at today's depth. Dashed lines are the gas saturated sandstone, and solid lines are the brine saturated.

For this period, the uplifted sandstones have a lower bulk modulus than point 9, for both gas and brine saturation. For lower porosities, there are significant changes in bulk modulus due to both burial effects and fluid substitution. The change in bulk modulus for higher porosities is caused by burial effects.

Shear modulus shows two distinct trends, where the change is due to burial history and unchanged due to fluid substitution. Here, the uplifted sandstones have a lower shear strength.

The density is approximately the same for both periods, due to the same minerals and fluids.

The P-wave velocity is lower for the uplifted point for lower porosities, for both gas and brine saturation. For higher porosities, the velocity trends tend to overlay each other. For both period 5 and 9, the gas saturated sandstone has a lower velocity than the brine filled.

The same trends are observable for the S-wave velocity; the uplifted sandstone in point 9 has a lower velocity than the maximum buried. The gas-saturated sandstones tend to have a higher velocity for the cemented point.

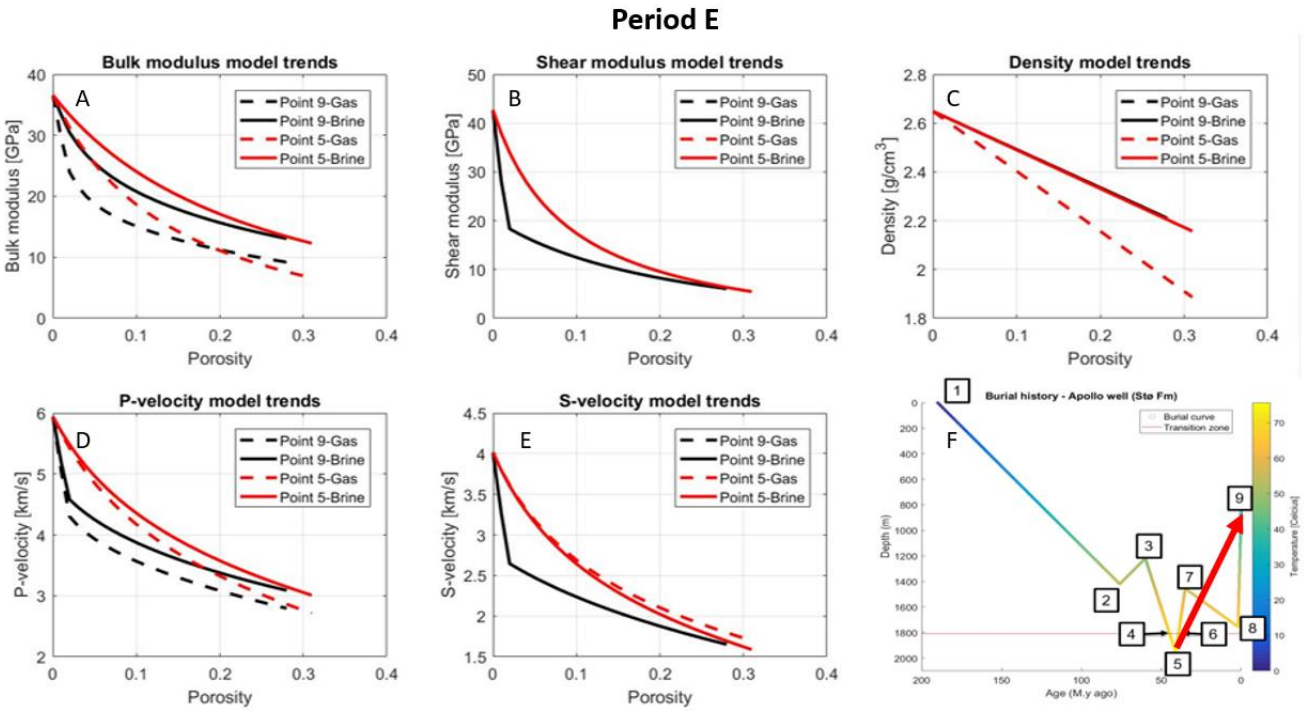

Figure 5.9 – Rock physics modelling for the 5th and 9th point in the burial model. The red lines represent the 5th point, and the black lines are the 9th point. The solid lines are brine saturation, and the dashed lines are gas saturation. The well data is displayed as dots, colored for the depths. The color bar is numbered for depths in the well, over the Stø Formation. The different plots describe the (A) bulk modulus, (B) shear modulus, (C) the density, (D) Vp, (E) Vs and (F) the burial history.

5.2.6 Rock physics models versus the Stø formation in well 7324/2-1

The rock physics model for today's depth for 100 % gas and brine saturation was first compared to the Stø formation (Figure 5.10). Here the dots represent the real data, and the color-coding gives the depth of the reservoir. The dashed line shows the response for 100% gas saturation, and the solid lines the 100% brine saturated.

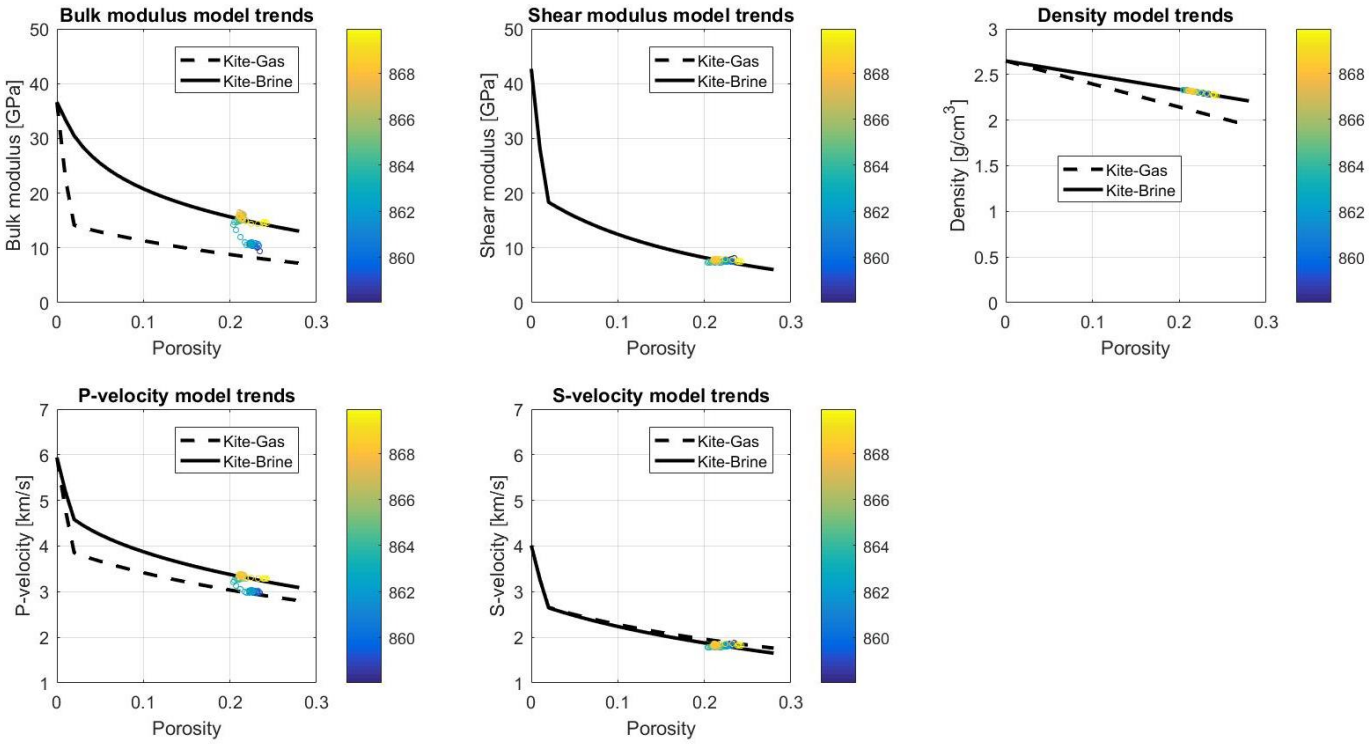

Figure 5.10 – The rock physics modelling in point 9 compared to the well data for the Stø formation. Here the dashed line represents the 100% gas saturation, and the solid line represents the 100 % brine saturated. The well data is displayed as dots, colored for the depths. The color bar is numbered for depths in the well, over the Stø Formation.

For the brine saturation, the model fits the well data for the lower part of the reservoir. For the top of the reservoir, the gas saturation at 100% makes the model a bit softer for the bulk modulus and density than the real data. The resistivity log (Figure 1 in the Appendix) and NPD (2016a) states that the formation is water saturated, or contains small amounts of gas. Therefore, the modeling was redone – keeping the 100% brine saturation for the lower part of the reservoir but reduce the amount of gas in the top portion to only 1% gas (99 % brine). This was done using a homogeneous fluid mixing, to comply with the assumptions for Gassmann's equation. The results in Figure 5.11, shows a close agreement with well data. Also, Figure 5.12 displays a good match between the model and the data for the upper and lower part of the reservoir. From this, the reservoir could potentially have a GWC at approximately 863 meters depth.

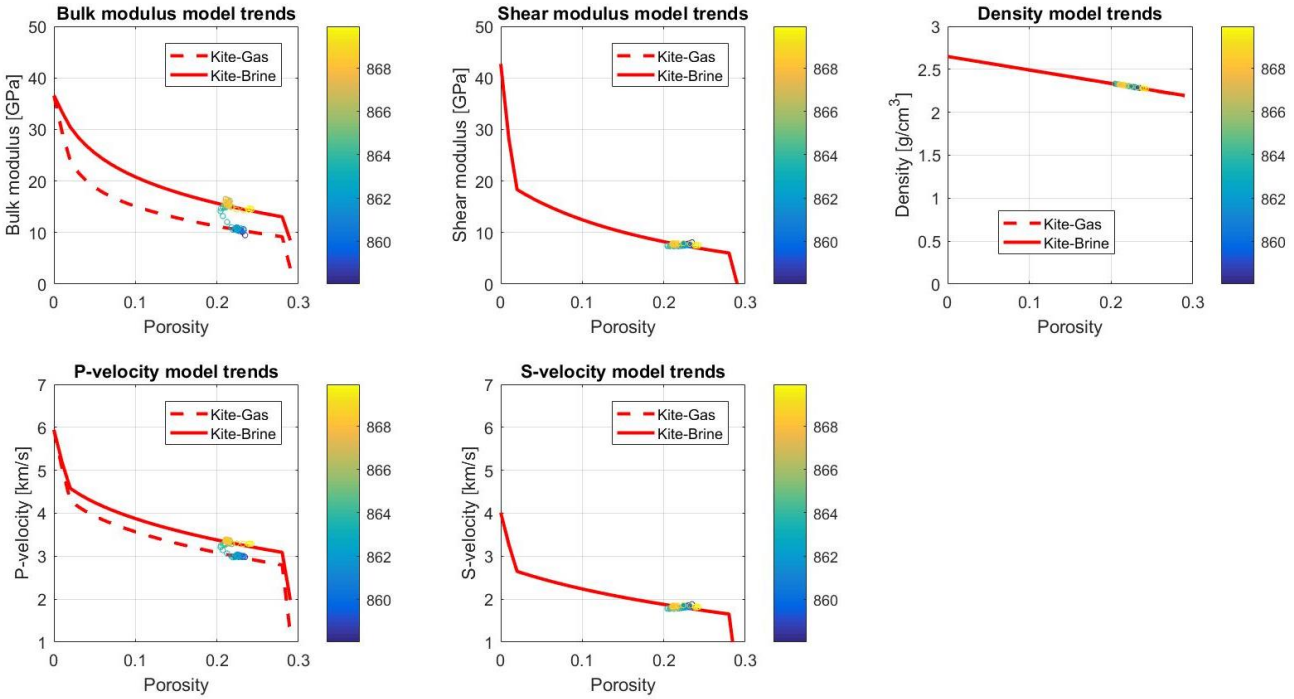

Figure 5.11 – The rock physics modelling in point 9 compared to the well data for the Stø formation. Here the dashed line represents the 1 % gas saturation (99 % brine), and the solid line represents the 100 % brine saturated. The well data is displayed as dots, colored for the depths. The color bar is number for depths in the well, over the Stø Formation.

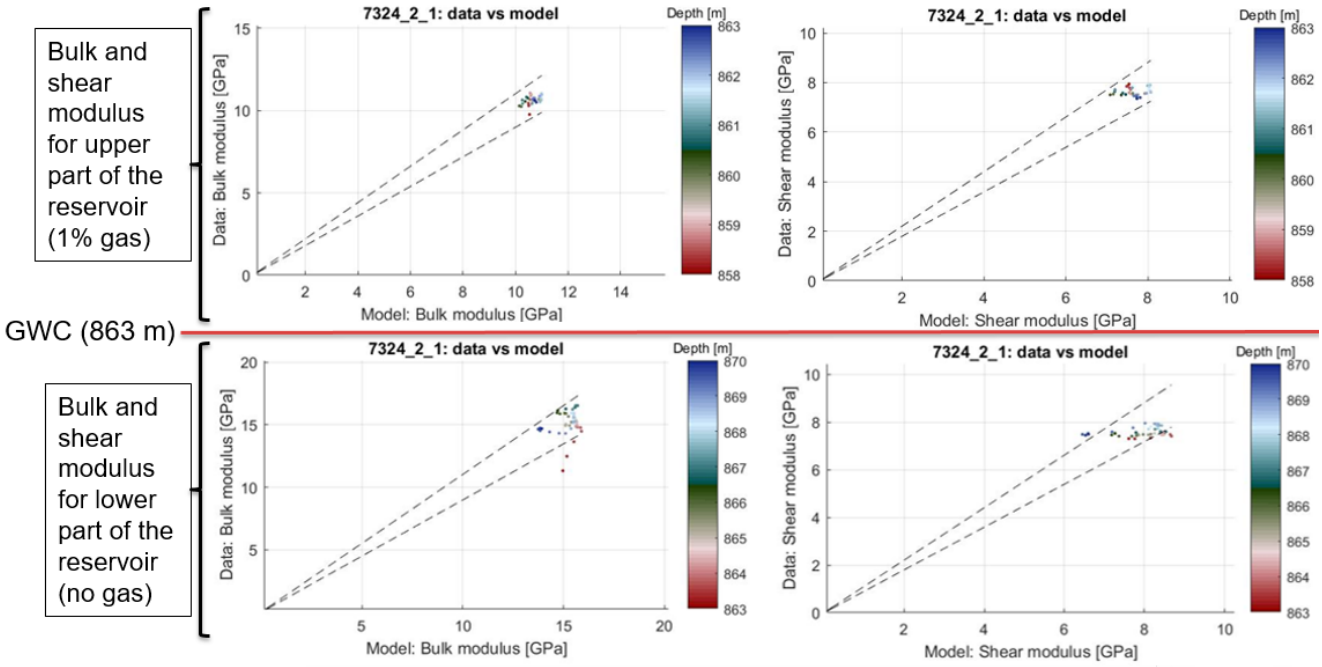

Figure 5.12 – Cross plot for data versus model. The upper results are for the bulk and shear modulus above the GWC. The lower results are for the bulk and shear modulus below the GWC.

5.2.7 *Vp*/*Vs* trends versus acoustic impedance

Figure 5.13, displays a rock physics template for the Stø formation during the burial history as a *Vp*/*Vs*-trends versus the acoustic impedance. This model describes the sandstone as a function of changes in pressure, mineralogy, porosity and fluid. In the figure, the results can be divided into four different quadrants:

- The first quadrant holds uncemented sandstone with 100 % brine saturation.
- The second quadrant holds cemented sandstones with 100 % brine saturation.
- The third quadrant holds cemented sandstones with 100 % gas saturation.
- The fourth quadrant holds uncemented sandstones with 100 % gas saturation.

The different quadrants show that cement increases the acoustic impedance for both saturations. Increased gas saturation decreases the *Vp*/*Vs*-ratio, giving the gas-filled sandstone an overall lower ratio than the brine-filled.

The brine-filled cemented, sandstones have a lower *Vp*/*Vs*-ratio and higher acoustic impedance than the uncemented brine-filled.

The cemented gas saturated sandstone has a higher acoustic impedance than the uncemented gas-filled points, but the *Vp*/*Vs*-ratio is unchanged.

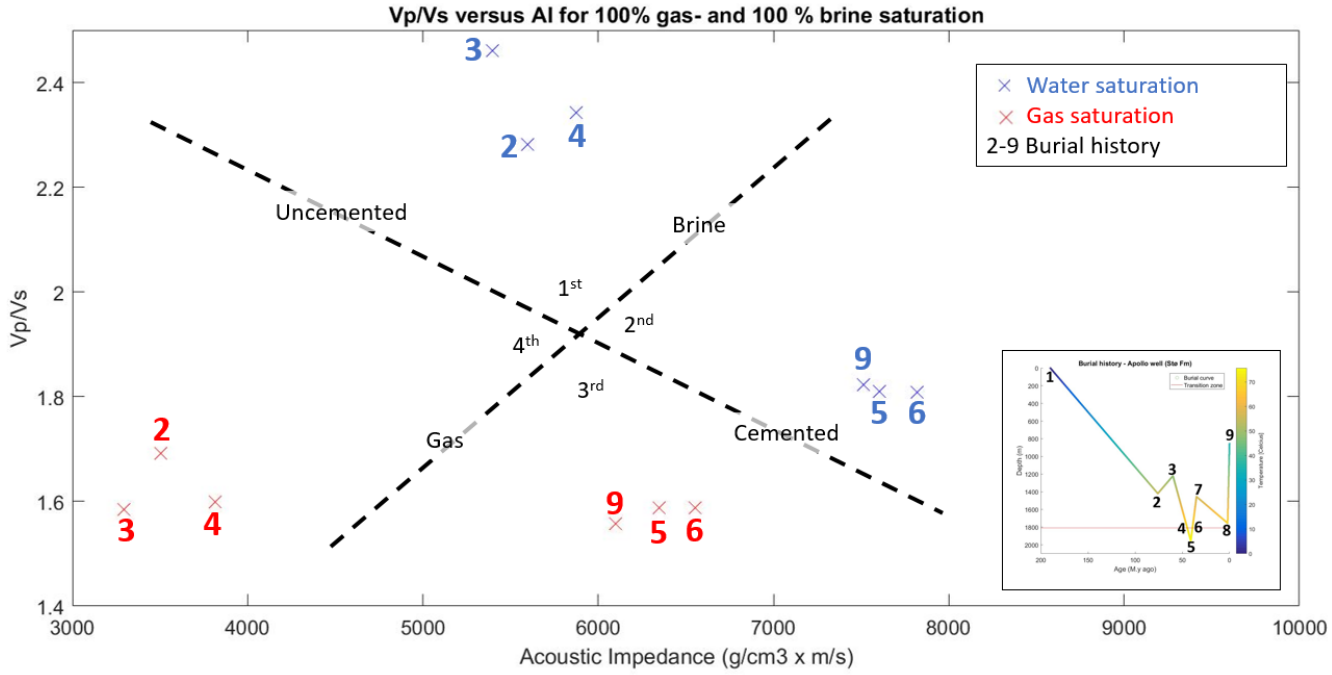

Figure 5.13 - Cross plot for *Vp*/*Vs* versus AI for the burial history for the Stø formation. Showing how the Stø formation changes during burial, the results can be divided into four different quadrants. First and second quadrant holds the uncemented and cemented sandstone with brine saturation, respectively. The third quadrant represents the gas-filled, cemented, sandstones and the fourth, gas-filled, uncemented, sandstones.

5.3 AVO-modelling

5.3.1 AVO-responses for Stø Formation

The AVO-responses for the Stø formation during the burial history is described in Figure 5.14. The AVO-modeling is done using a fix cap-rock with properties from the in-situ cap-rock (Fuglen formation). From the figure, it is possible to see several big (primary effects) and smaller (secondary effects) changes:

Primary effects:

- Fluid substitution has a greater impact on the intercept than the gradient, particularly for the uncemented sandstones. An increased amount of gas shifts the intercept to lower values for both cemented and uncemented sandstones, and this effect is greatest for uncemented sandstones.
- Cementation has a significant impact on both intercept and gradient; the gradient moves towards lower values and the intercept towards higher values.

Secondary effects:

- Inside each quadrant, increased temperature and pressure moves the trends for all points towards a higher value for the intercept and lower values for the gradient. This is the same trend as cementation but at a smaller scale.
- Uplift effects move the gradient and intercept in the opposite direction of the cementation and increased burial inside the quadrants. The intercept shifts to lower values, and the gradient towards higher values.

Further, the figure displays the in-situ period for today's reservoir- and cap-rock properties. The resulting point is in the second quadrant of the modeling. The AVO-response for today's situation has approximately the same gradient as the brine-filled, cemented periods. However, the intercept is more negative and have roughly the same intercept as the gas-filled, cemented periods. That gives a gradient response like a brine-filled sandstone and an intercept response as a gas-filled sandstone.

The AVO-response for the GWC is also presented in Figure 5.14 (three circles). These responses are calculated from the intercept between the brine-filled lower part of the reservoir

and the upper gas-filled. The *Vp*, *Vs*, and density for the upper part are found for gas saturation of 1 %, 50 %, and 100 %. The responses are all in the upper right corner of the gradient-intercept figure, due to positive gradient and intercept. This places the results in the 1st quadrant. From these responses, it should be possible to estimate separate the 1 % gas- and 100 % gas saturations in the top reservoir. The AVO-responses in the 1st quadrant is classified as AVO-class VI. The figure displays how the increased amount of gas shifts the response towards higher values for the intercept and gradient.

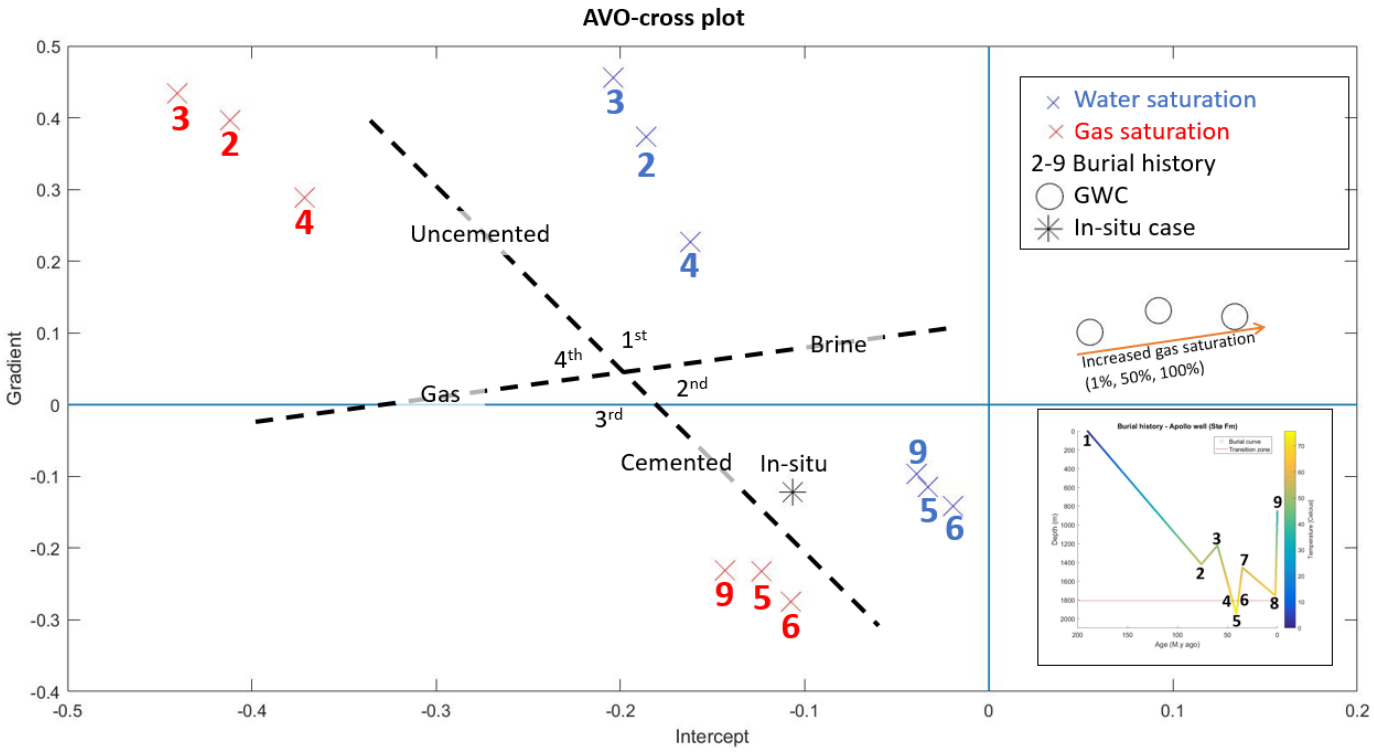

Figure 5.14 – Here, the AVO-responses are displayed in an intercept-gradient cross plot. The numbers represent various stages in the burial history, and the red numbers are gas-filled periods and blue are brine-filled. The AVO-response for the in-situ period in the Stø formation is presented as well (star). In addition, the AVO-response for the GWC is displayed with three circles.

Chapter 6: Discussion

As shown in chapter 5, two major factors are affecting the results; cementation and fluid substitution. This chapter will discuss the three key assumptions which the results are based on – the geological model, elastic properties and seismic signatures. More precisely, the reliability of the geological model and the validity of the elastic properties and seismic signatures will be examined.

6.1 Geological model

Geological modeling is not fluid dependent, therefore only cementation will be discussed in this section. Yet there are numerous uncertainties regarding cementation for the geological burial curve, for example assumptions on what have happened in the past, such as time of deposition, rate of burial and the geothermal gradient (Bjørlykke and Jahren, 2010). This also applies to this study. In this section, the primary discussion focus on the uncertainty associated with the reliability of the burial curve.

The results show that the reservoir has been cemented, and this is based on estimates for the maximum burial depth and the geothermal gradient (Avseth and Lehocki, 2016, Dræge et al., 2014). Without reliable estimates for these two components, it is difficult to determine if the reservoir has been in the chemical compaction regime.

There are three main objections for the maximum burial estimate in this study; the shale data used for the *Vp*-depth is not pure shale (shale volume > 75 %), the small data coverage, and that the area of reference for the trend lines might have a different temperature and pressure than the area investigated (Baig et al., 2016). Although these are important factors, the results from the two uplift estimates in this study combined with the close agreement for the Bjarmeland Platform burial curve (Ohm et al., 2008), indicates that the maximum burial estimate is reasonable.

There are two main uncertainties linked to the fixed geothermal gradient at 38,7 °C used in this study; the accuracy of the temperature and time-independence. Although the gradient used is above the average in the Barents Sea (Laberg et al., 1998), and there is uncertainty connected to the use of bottom hole temperature, the results show that it is not unreasonable to believe that the geothermal gradient at 38,7 °C it is correct. Regarding time-independence (Palumbo et al.,

1999), there is a weakness with the geological model in this study because it is not sensitive to temperature changes over time. Although, the analyses of the transition zone between mechanical and chemical compaction domain combined with the uplift estimate, indicates that the fixed gradient is reasonable for the understanding of the onset of cementation.

As with all geological models, assumptions regarding porosity estimates need to be discussed (Walderhaug, 1996). There are several problems associated with the porosity modeling, such as the assumption of spherical grains with a perfect sorting and that the chemical compaction regime is given a fixed amount of cementation and porosity. Although there are several uncertainties, it has in this study been modeled a critical porosity that includes the in-situ data from well 7324/2-1.

In summary, there are several uncertainties regarding the geological model in this study. Nevertheless, the results show that the model is reasonably good for estimation of the cementation processes in the in the area around the reference well in the Stø Formation.

6.2 Elastic properties

Elastic properties depend among others on the reliability of the geological model and is discussed in the previously section. In this section, the discussion focuses on the changes in bulk modulus, shear modulus and the *Vp*/*Vs* versus AI due to cementation and fluid substitution during a burial history.

Changes in bulk modulus

Once the cement starts to form in the sandstone the bulk modulus increases for all porosities (Figure 2 in Appendix shows changes in bulk modulus during burial). This stiffening of the sandstone is caused by cement filling the pore space and reinforce the grain contacts; in agreement with published articles (Avseth et al., 2000, Zhang and Bentley, 2003, Avseth et al., 2014).

As expected, the results show that fluid substitution (gas and brine) changes the bulk modulus substantially (Smith et al., 2003). This change is caused by the lower bulk modulus for gas than for brine. Gassmann's equation (Equation 3.8) states that the fluid saturated bulk modulus increases when the bulk modulus of the fluid increases (and minerals are unchanged).

Although it provides a minor change in the bulk modulus, uplift is an interesting event. The uplift can result in the formation of cracks in the sandstone, resulting in a lowering of the bulk modulus (Avseth et al., 2014). Both the gas- and brine-saturated sandstone shows a close agreement with Figure 3.7A presented by Avseth et al. (2014).

Changes in shear modulus

The sandstones get stiffer when cemented, and the shear modulus increases (Figure 3 in the Appendix displays changes in shear modulus during burial). This is caused by the cementation in the pore space and reinforcement of the grain contacts (Avseth et al., 2000, Zhang and Bentley, 2003, Dræge et al., 2006, Avseth et al., 2014).

The uplift shows a decrease in shear modulus for lower porosities, in agreement with Avseth et al. (2014). This reduction is caused by the lower temperature and pressure, in addition to the formation of cracks. The biggest impact for the elastic parameters is found for lower porosities due to increased influence of cracks with decreasing porosity.

Vp/*Vs* versus acoustic impedance during burial history

The *Vp*/*Vs* versus acoustic impedance results can be divided into four different quadrants (Figure 5.13). These quadrants separates the cemented and uncemented sandstones, and the gas- and brine saturation.

The onset of cementation in the sandstones shows an increase in acoustic impedance for both gas- and brine-saturated sandstones, in agreement with Avseth et al. (2010). This trend is primarily caused by an increase in *Vp*, as a result of the cementation.

For the onset of cementation, the *Vp*/*Vs*-trend differs for the two saturations; the brine-filled sandstones have a decreasing *Vp*/*Vs*-ratio, while the gas-filled sandstone is nearly unchanged. The reduction for the brine-filled cases is caused by a greater relatively increase in the *Vs* than the *Vp* when cementation starts. While the gas-filled sandstones are almost unchanged due to the same relatively increase for both *Vp* and *Vs*. These results show close agreement with the trends published by Avseth et al. (2010).

For the fluid saturation each of the gas-filled points has a lower *Vp*/*Vs*-ratio and acoustic impedance compared to the corresponding brine-filled points. This is an expected response and agrees with Avseth et al. (2010) (Figure 4.3). This decrease in the *Vp*/*Vs*-ratio is caused by the decrease in *Vp* and increase in *Vs* when brine is replaced by gas (Hamada, 2004). The reduction in acoustic impedance for gas-filled sandstone is caused by a decrease in *Vp* and density (Avseth et al., 2010).

This shows that the cementation and fluid saturation also shifts the results in this study in agreement Avseth et al. (2010).

In each of the quadrants, there are minor changes compared to cementation and fluid substitution, but some interesting trends can be seen agrees with Avseth et al. (2010):

- In the brine-filled sandstone, uplift and the formation of cracks shift the results towards a higher *Vp*/*Vs* and a lower acoustic impedance. This result is similar to the one for decreasing effective pressure presented by Avseth et al. (2010), but the cracks can potentially make this response greater.
- The cracks have a bigger impact on uncemented sandstone than cemented sandstone. The uplift before cementation increases the porosity and decreases elastic properties more than the uplift cemented sandstones. This is because the uplift for uncemented sandstones relieve the pressure on the grain contacts in addition to the cracks, while the

cemented only experience the formation of cracks because the grain contacts are cemented (Narongsirikul et al., 2013a).

- The trend for cracks in gas-filled sandstone shows a shift towards a lower *Vp*/*Vs* and a lower acoustic impedance. This is caused by a lower pressure and temperature, in addition to the increased porosity (increased amount of gas), resulting in a lower *Vp* and higher *Vs* in agreement with.

Uncertainties for the modeling of elastic properties

There are uncertainties to the modelling of elastic properties because it relates on perfect sorting and spherical grains. Though, few sandstone reservoirs have these perfect conditions, and it might affect the results (Bachrach and Avseth, 2008). These parameters have been calibrated to the well data in 7324/2-1, and is assumed to be acceptable due to a good match between model and well data.

The modeling also assumes an isotropic sandstone, and that microcracks and fractures are randomly oriented. These parameters are not taken into account in this study, but could for example be found from a regional stress history for the area (Doré et al., 2002). This is an interesting area for further work.

There are two uplift events in the burial history that potentially can cause uncertainties. The first uplift event occurs before cementation starts and is in this study modeled with the formation of cracks because it is assumed that the sandstone has been buried deeply, and long enough, to make the sand consolidated (Vernik, 2016). The second uplift in the chemical compaction regime (>70 °C) is also debatable. In this study, this process is assumed to occur without formation of cracks in agreement with Bjørlykke and Jahren (2010).

The amount of cement in the reservoir is fixed in the chemical compaction domain, and might give the early cementation period a too high cement volume. Although, the well-calibration shows a low cement volume and is assumed to be adequate for this study.

Although there are several uncertainties regarding the rock physics modeling, the data and model show a close agreement in Figure 5.12, for both upper and lower part of the reservoir. This proves that it is possible to model sandstone properties of a reservoir today if the geological history is known. Also, it confirms that the modeling of elastic properties in this study provides a realistic description of the properties in the Stø Formation.

6.3 Seismic signatures

In the previous sections, the reliability of the geological model and the validity of the elastic properties have been examined. In this section, the validity of the seismic signatures will be discussed. More precis, the discussion will focus on how the seismic signatures change for siliciclastic reservoirs as a function of the burial history, and compare it with the in-situ case for the Stø Formation in well 7324/2-1. In addition, the AVO-response for the GWC is calculated to see if it is possible to separate low and high gas saturation in a reservoir.

Changes in seismic signatures for the burial history

In the results, the cementation shifts the AVO-responses towards a lower gradient and a higher intercept, for both gas and brine saturation. This response confirms that the cementation increases the seismic velocities in the reservoir (Lehocki and Avseth, 2015), and is in agreement with Avseth et al. (2010) where the cemented sandstones have a larger intercept than uncemented sandstones.

A second major factor for the AVO-responses is the fluid substitution. The results display how changes in saturation displace the AVO-responses for cemented and uncemented sandstone. The uncemented sandstones shifts towards a higher intercept when brine saturated and the gradient are virtually unchanged compared to gas saturation. While the cemented sandstones shift towards a higher intercept and gradient when the gas saturation increases. Increased intercept can be explained by higher *Vp* for brine-filled sandstones than gas-filled (Castagna et al., 1998).

These observations are in agreement with (Avseth et al., 2010), where the lowest intercept is observed for the gas-filled uncemented sandstones. The brine-filled unconsolidated sands are higher but close to the cemented gas-filled period. The highest intercept is found for the cemented, gas-filled sandstone.

There are some minor, general trends as well:

- The first and fourth quadrant displays that increased pressure and temperature shifts the results towards a higher intercept and lower gradient. This is due to the increased *Vp*, *Vs* and density. Also, the uplift counteracts the increased burial, because of the decrease in *Vp*, *Vs*, and density as a response to the lowered temperature, pressure and formation of cracks (Narongsirikul et al., 2013b).

- The second and third quadrant shows the same trends, where increased cementation drives the results towards a lower gradient and higher intercept. The uplift events shift the results in the opposite direction.

For these changes, the uncemented points have a greater displacement than the cemented. This can be explained by the fact that the uncemented sandstone benefits more from the release in pressure and temperature because the grains are not cemented.

The in-situ AVO-response for the Stø Formation is also shown and is classified as AVO-class III, being a relatively soft sandstone with high fluid sensitivity (Castagna et al., 1998, Avseth et al., 2010). This result has a response in the cemented area, between the brine- and gas-saturated periods. This confirms that the reservoir is cemented. The fluid saturation is a bit more complex. However, it is clear that the reservoir neither is 100% brine- or gas-filled. Comparison of the in-situ period and the 100 % gas-filled period shows that the in-situ has a higher intercept and gradient. This is caused by the higher *Vp* and lower *Vs* for the in-situ, due to the smaller amount of gas. The 100 % brine-filled period shows an insignificant higher gradient and a lower intercept than the in-situ period because the small amount of gas in the in-situ decreases the *Vp* more than the *Vs* increases. This is in agreement with a reservoir containing a small amount of gas.

Seismic signatures for the GWC

In this study, the AVO-response for the GWC has also been modeled. This response shows how the intercept changes due to different percentages of gas saturation in the reservoir and shows that an increase in gas saturation shifts the AVO-responses towards a higher intercept. This is caused by the reduction in *Vp* in the upper part of the reservoir as a response to the increasing percentage of gas. Still, this method is not widely used and was included in this study to see if it was possible to distinguish between high and low gas-saturations.

Uncertainties for the AVO-modelling

The biggest concern regarding the AVO-results is that they are based on the rock physics modeling and geological history, as already discussed, and might affect the accuracy of AVO-modeling.

Another difficulty associated with AVO-modelling in this thesis is that the cap rock is fixed. This gives an uncertainty, since the cap rock is inaccurate for several periods, giving a slightly erroneous seismic signature. Although, it makes the investigation of changes in the sandstone reservoir easier to observe and the trends in the results give a good match with published articles (Lehocki and Avseth, 2015, Avseth and Lehocki, 2016).

The intercept is calculated using Shuey's approximation and should give valid results for incidence angles up to 30 degrees. Still, there are more accurate methods, especially regarding the gradient. The gradient in this study is calculated simplistic from the deviation between zero-offset intercept and the intercept at 30 degrees.

All trends show a good agreement with existing models (Lehocki and Avseth, 2015, Avseth and Lehocki, 2016). Also, the AVO-response for the in-situ period gives a good match to the modeled point 9. The large deviations for cemented and uncemented sandstones with different saturation agree with published data (Dræge et al., 2006, AlMustafa and Bakhorji, 2011). Proving that the AVO-results in this thesis is sufficient for a description of how general trends in seismic signatures for sandstone reservoirs alters during a burial history.

Chapter 7: Conclusions

In this thesis, the effect of burial history on the effective rock properties and seismic signatures for a sandstone reservoir have been studied. This has been done based on the burial history in the Barents Sea and well log data from 7324/2-1. It has been used several different theories to calculate the dry rock properties, and Gassmann's equation was used to find the saturation effects. Further, Shuey's approximation was used to calculate the seismic signatures.

It has been shown that the major factors controlling the elastic properties and seismic signatures during a burial history are cementation and fluid substitution. From this, the main findings in this study are:

- The geological history is crucial for the modeling of elastic properties and seismic signatures, due to the importance of input from the history. While the most important part of the burial history is the transition zone from mechanical to chemical compaction regime. Both the results for elastic properties and seismic signatures confirms this by showing a big displacement of results when comparing uncemented and cemented periods.
- Fluid substitution has a substantial impact on the pressure wave velocity (*Vp*) and the *Vp*/*Vs*-ratio. When gas replaces brine, the *Vp* decreases, and the *Vs* increases slightly. This separates the gas- and brine-filled sandstones for both elastic properties and seismic signatures. It is also shown that the fluid substitution has a bigger impact on uncemented sandstones than the cemented. Still, the results show that intercept-gradient plots easily could separate between different saturations.
- There are also minor trends during the burial history. Burial increases pressure and temperature, shifting seismic signatures towards a higher intercept and lower gradient. Uplift reduces pressure and temperature and might result in the formation of cracks. This even shifts the results for seismic signatures in the opposite direction of burial.
- From the seismic signatures found in this study, it should be possible to distinguish between cemented and uncemented sandstones. Also, the brine- and gas saturated sandstones should be distinguishable.

As shown, one can model elastic properties for different steps during a burial history, both for chemical and mechanical compaction and for uplifts. When honoring the various parts of a burial history, it is possible to model a nearly perfect match to a given well data. This

quantitative seismic interpretation technique has an huge potential for hydrocarbon exploration in remote areas with a complex burial history. In this study, rock physics modeling in combination with a geological model has given a nearly perfect match with the reference well. The modeling is easy to adapt to different burial models, and a more detailed model than the one used in this study could constrain the results even further. This could potentially make it possible to predict seismic signatures for any reservoir in the world, with a unique burial history.

Further work

- The porosity evolution should be further investigated, to get a more precise rock physics modeling.
- Compare the burial history modeled in this study to real data for different depths. For wells all over the world, to check the validity of the model for the various steps used in this thesis.
- Modeling the complete burial history for the cap rock (shale), to see how the cap rock compares to the sandstone reservoir during a burial history, for a more realistic understanding of AVO-responses.

References:

AKI, K. & RICHARDS, P. G. 2002. *Quantitative seismology*.

ALMUSTAFA, H. & BAKHORJI, A. 2011. Rock physics AVO depth trends: Implications for exploration in Saudi Arabia. *SEG Technical Program Expanded Abstracts 2011.* Society of Exploration Geophysicists.

ATLAS, D. 1982. Well logging and interpretation techniques. *The course for home study. Dresser Atlas Publ*.

AVSETH, P. & BACHRACH, R. 2005. Seismic properties of unconsolidated sands: Tangential stiffness, Vp/Vs ratios and diagenesis. *SEG Technical Program Expanded Abstracts 2005.* Society of Exploration Geophysicists.

AVSETH, P., DVORKIN, J., MAVKO, G. & RYKKJE, J. 2000. Rock physics diagnostic of North Sea sands: Link between microstructure and seismic properties. *Geophysical Research Letters,* 27**,** 2761-2764.

AVSETH, P., JOHANSEN, T. A., BAKHORJI, A. & MUSTAFA, H. M. 2014. Rock-physics modeling guided by depositional and burial history in low-to-intermediate-porosity sandstones. *GEOPHYSICS,* 79**,** D115-D121.

AVSETH, P. & LEHOCKI, I. 2016. Combining burial history and rock-physics modeling to constrain AVO analysis during exploration. *The Leading Edge,* 35**,** 528-534.

AVSETH, P., MUKERJI, T. & MAVKO, G. 2010. *Quantitative seismic interpretation: Applying rock physics tools to reduce interpretation risk*, Cambridge university press.

AVSETH, P. Å. 2000. *Combining rock physics and sedimentology for seismic reservoir characterization of North Sea turbidite systems.* Stanford University.

BACHRACH, R. & AVSETH, P. 2008. Rock physics modeling of unconsolidated sands: Accounting for nonuniform contacts and heterogeneous stress fields in the effective media approximation with applications to hydrocarbon exploration. *Geophysics,* 73**,** E197-E209.

BAIG, I., FALEIDE, J. I., JAHREN, J. & MONDOL, N. H. 2016. Cenozoic exhumation on the southwestern Barents Shelf: Estimates and uncertainties constrained from compaction and thermal maturity analyses. *Marine and Petroleum Geology,* 73**,** 105-130.

BASSIOUNI, Z. 1994. *Theory, measurement, and interpretation of well logs*, Henry L. Doherty Memorial Fund of AIME, Society of Petroleum Engineers.

BATZLE, M. & WANG, Z. 1992. Seismic properties of pore fluids. *Geophysics,* 57**,** 1396-1408.

BERRYMAN, J. G. 1992. Single-scattering approximations for coefficients in Biot's equations of poroelasticity. *The Journal of the Acoustical Society of America,* 91**,** 551-571.

BJØRLYKKE, K., HØEG, K. & MONDOL, N. H. 2015. Introduction to Geomechanics: stress and strain in sedimentary basins. *Petroleum Geoscience.* Springer.

BJØRLYKKE, K. & JAHREN, J. 2010. *Sandstones and sandstone reservoirs*, Springer.

BORTFELD, R. 1961. Approximations to the reflection and transmission coefficients of plane longitudinal and transverse waves. *Geophysical Prospecting,* 9**,** 485-502.

BROADHEAD, R. 2002. The origin of oil and gas. *NEW MEXICO'S ENERGY, PRESENT AND FUTURE***,** 41.

CASTAGNA, J., BATZLE, M. & KAN, T. 1993. Rock physics—The link between rock properties and AVO response. *Offset-dependent reflectivity—Theory and practice of AVO analysis: SEG,* 8**,** 135-171.

CASTAGNA, J. P. & BACKUS, M. M. 1993. *Offset-dependent reflectivity—Theory and practice of AVO analysis*, Society of Exploration Geophysicists.

CASTAGNA, J. P., BATZLE, M. L. & EASTWOOD, R. L. 1985. Relationships between compressional-wave and shear-wave velocities in clastic silicate rocks. *Geophysics,* 50**,** 571-581.

CASTAGNA, J. P. & SWAN, H. W. 1997. Principles of AVO crossplotting. *The leading edge,* 16**,** 337-344.

CASTAGNA, J. P., SWAN, H. W. & FOSTER, D. J. 1998. Framework for AVO gradient and intercept interpretation. *Geophysics,* 63**,** 948-956.

CLAVIER, C., HOYLE, W. & MEUNIER, D. 1971. Quantitative interpretation of thermal neutron decay time logs: part I. Fundamentals and techniques. *Journal of Petroleum Technology,* 23**,** 743-755.

DALLAN, A., WORSLEY, D. & OFSTAD, K. 1988. A lithostratigraphic scheme for the Mesozoic and Cenozoic succession offshore mid- and northern Norway. *NPD-Bulletin No 4*.

DANIEL, R. & KALDI, J. 2008. Evaluating seal capacity of caprocks and intraformational barriers for the geosequestration of CO2.

DORÉ, A. 1995. Barents Sea geology, petroleum resources and commercial potential. *Arctic***,** 207-221.

DORÉ, A., CORCORAN, D. & SCOTCHMAN, I. 2002. Prediction of the hydrocarbon system in exhumed basins, and application to the NW European margin. *Geological Society, London, Special Publications,* 196**,** 401-429.

DRÆGE, A., DUFFAUT, K., WIIK, T. & HOKSTAD, K. 2014. Linking rock physics and basin history—Filling gaps between wells in frontier basins. *The Leading Edge,* 33**,** 240-246.

DRÆGE, A., JOHANSEN, T. A., BREVIK, I. & DRÆGE, C. T. 2006. A strategy for modelling the diagenetic evolution of seismic properties in sandstones. *Petroleum Geoscience,* 12**,** 309-323.

DURAN, E. R., DI PRIMIO, R., ANKA, Z., STODDART, D. & HORSFIELD, B. 2013. Petroleum system analysis of the Hammerfest Basin (southwestern Barents Sea): Comparison of basin modelling and geochemical data. *Organic geochemistry,* 63**,** 105-121.

DVORKIN, J. & NUR, A. 1996. Elasticity of high-porosity sandstones: Theory for two North Sea data sets. *Geophysics,* 61**,** 1363-1370.

EHRENBERG, S. 1990. Relationship between diagenesis and reservoir quality in sandstones of the Garn formation, Haltenbanken, mid-Norwegian Continental shelf (1). *AAPG bulletin,* 74**,** 1538-1558.

FALEIDE, J. I., SOLHEIM, A., FIEDLER, A., HJELSTUEN, B. O., ANDERSEN, E. S. & VANNESTE, K. 1996. Late Cenozoic evolution of the western Barents Sea-Svalbard continental margin. *Global and Planetary Change,* 12**,** 53-74.

FENG, H. & BANCROFT, J. C. 2006. AVO principles, processing and inversion.

GABRIELSEN, R. H., FAERSETH, R. B. & JENSEN, L. N. 1990. *Structural Elements of the Norwegian Continental Shelf. Pt. 1. The Barents Sea Region*, Norwegian Petroleum Directorate.

GABRIELSEN, R. H., FALEIDE, J. I., PASCAL, C., BRAATHEN, A., NYSTUEN, J. P., ETZELMULLER, B. & O'DONNELL, S. 2010. Latest Caledonian to Present tectonomorphological development of southern Norway. *Marine and Petroleum Geology,* 27**,** 709-723.

GABRIELSEN, R. H., SOKOUTIS, D., WILLINGSHOFER, E. & FALEIDE, J. I. 2016. Fault linkage across weak layers during extension: an experimental approach with reference to the Hoop Fault Complex of the SW Barents Sea. *Petroleum Geoscience,* 22**,** 123-135.

GASSMANN, F. 1951. Elastic waves through a packing of spheres. *Geophysics,* 16**,** 673-685.

GLØRSTAD-CLARK, E., BIRKELAND, E., NYSTUEN, J., FALEIDE, J. & MIDTKANDAL, I. 2011. Triassic platform-margin deltas in the western Barents Sea. *Marine and Petroleum Geology,* 28**,** 1294-1314.

GLØRSTAD-CLARK, E., FALEIDE, J. I., LUNDSCHIEN, B. A. & NYSTUEN, J. P. 2010. Triassic seismic sequence stratigraphy and paleogeography of the western Barents Sea area. *Marine and Petroleum Geology,* 27**,** 1448-1475.

GOODWAY, B., SZELEWSKI, C., OVERELL, S., CORBETT, N. & SKRYPNEK, T. 2008. Calibrated AVO and LMR analysis using a new DHI flat-spot AVO class 6 fluid contact to mitigate reservoir risk at Stonehouse, offshore Nova Scotia.

GORNITZ, V. 2008. *Encyclopedia of paleoclimatology and ancient environments*, Springer Science & Business Media.

GUDLAUGSSON, S., FALEIDE, J., JOHANSEN, S. & BREIVIK, A. 1998. Late Palaeozoic structural development of the south-western Barents Sea. *Marine and Petroleum Geology,* 15**,** 73-102.

HAMADA, G. An Integrated Approach to Determine Shale Volume and Hydrocarbon Potential in Shaly Sand. SCA paper 9548, presented at SCA Intl. Symposium, 1996. 12-14.

HAMADA, G. 2004. Reservoir fluids identification using Vp/Vs ratio? *Oil & Gas Science and Technology,* 59**,** 649-654.

HAN, D.-H. & BATZLE, M. 2000. Velocity, density and modulus of hydrocarbon fluids—Data measurement. *SEG Technical Program Expanded Abstracts 2000.* Society of Exploration Geophysicists.

HAN, D.-H. & BATZLE, M. L. 2004. Gassmann's equation and fluid-saturation effects on seismic velocities. *Geophysics,* 69**,** 398-405.

HAN, D.-H., NUR, A. & MORGAN, D. 1986. Effects of porosity and clay content on wave velocities in sandstones. *Geophysics,* 51**,** 2093-2107.

HASHIN, Z. & SHTRIKMAN, S. 1963. A variational approach to the theory of the elastic behaviour of multiphase materials. *Journal of the Mechanics and Physics of Solids,* 11**,** 127-140.

HENRIKSEN, E., BJØRNSETH, H., HALS, T., HEIDE, T., KIRYUKHINA, T., KLØVJAN, O., LARSSEN, G., RYSETH, A., RØNNING, K. & SOLLID, K. 2011a. Uplift and erosion of the greater Barents Sea: impact on prospectivity and petroleum systems. *Geological Society, London, Memoirs,* 35**,** 271-281.

HENRIKSEN, E., RYSETH, A., LARSSEN, G., HEIDE, T., RØNNING, K., SOLLID, K. & STOUPAKOVA, A. 2011b. Tectonostratigraphy of the greater Barents Sea: implications for petroleum systems. *Geological Society, London, Memoirs,* 35**,** 163-195.

HOLDITCH, S. A. & CHIANELLI, R. R. 2008. Factors that will influence oil and gas supply and demand in the 21st century. *MRS bulletin,* 33**,** 317-323.

HYNE, N. J. 2012. *Nontechnical guide to petroleum geology, exploration, drilling, and production*, PennWell Books.

JAPSEN, P. 2006. Velocity-depth trends in Mesozoic and Cenozoic sediments from the Norwegian Shelf: Discussion. *AAPG Bulletin,* 90**,** 1141-1143.

JAPSEN, P. & CHALMERS, J. A. 2000. Neogene uplift and tectonics around the North Atlantic: overview. *Global and Planetary Change,* 24**,** 165-173.

JOHANSEN, S., OSTISTY, B., BIRKELAND, Ø., FEDOROVSKY, Y., MARTIROSJAN, V., CHRISTENSEN, O. B., CHEREDEEV, S., IGNATENKO, E. & MARGULIS, L. 1992. Hydrocarbon potential in the Barents Sea region: play distribution and potential. *Arctic Geology and Petroleum Potential, Norwegian Petroleum Society (NPF), Special Publication,* 2**,** 273-320.

KJØLHAMAR, B. 2015. The Hoop Area: New testing ground for geophysical technologies. *TGS*.

LABERG, J. S., ANDREASSEN, K. & KNUTSEN, S.-M. 1998. Inferred gas hydrate on the Barents Sea shelf — a model for its formation and a volume estimate. *Geo-Marine Letters,* 18**,** 26-33.

LARSEN, R., FJAERAN, T. & SKARPNES, O. 1993. Hydrocarbon potential of the Norwegian Barents Sea based on recent well results.

LEHOCKI, I. & AVSETH, P. AVO Modeling and Analysis Constrained by Burial History: Barents Sea Demonstrations. Third EAGE Workshop on Rock Physics, 2015.

LOENG, H. 1991. Features of the physical oceanographic conditions of the Barents Sea. *Polar research,* 10**,** 5-18.

MAGOON, L. B. 1988. The petroleum system—a classification scheme for research, exploration, and resource assessment. *Petroleum systems of the United States: US Geological Survey Bulletin,* 1870**,** 2-15.

MAGOON, L. B. & DOW, W. G. 1994. The Petroleum System: Chapter 1: Part I. Introduction.

MARCUSSEN, O., THYBERG, B. I., PELTONEN, C., JAHREN, J., BJORLYKKE, K. & FALEIDE, J. I. 2009. Physical properties of Cenozoic mudstones from the northern North Sea: Impact of clay mineralogy on compaction trends. *AAPG Bulletin,* 93**,** 127-150.

MARCUSSEN, Ø., MAAST, T. E., MONDOL, N. H., JAHREN, J. & BJØRLYKKE, K. 2010. Changes in physical properties of a reservoir sandstone as a function of burial depth–The Etive Formation, northern North Sea. *Marine and Petroleum Geology,* 27**,** 1725-1735.

MAVKO, G., MUKERJI, T. & DVORKIN, J. 2009. *The rock physics handbook: Tools for seismic analysis of porous media*, Cambridge university press.

MONDOL, N. H. 2009. Porosity and permeability development in mechanically compacted silt-kaolinite mixtures. *SEG Technical Program Expanded Abstracts 2009.* Society of Exploration Geophysicists.

MONDOL, N. H., BJØRLYKKE, K. & JAHREN, J. 2008. Experimental compaction of clays: relationship between permeability and petrophysical properties in mudstones. *Petroleum Geoscience,* 14**,** 319-337.

MONDOL, N. H., BJØRLYKKE, K., JAHREN, J. & HØEG, K. 2007. Experimental mechanical compaction of clay mineral aggregates—Changes in physical properties of mudstones during burial. *Marine and Petroleum Geology,* 24**,** 289-311.

MURPHY, W. F. 1982. *Effects of microstructure and pore fluids on the acoustic properties of granular sedimentary materials*, Stanford University, Department of Geophysics.

NARONGSIRIKUL, S., JAHREN, J. & MONDOL, N. H. 2013a. Possible application of friable sand model for shallow mechanically compacted overconsolidated sands. *SEG Technical Program Expanded Abstracts 2013.*

NARONGSIRIKUL, S., MONDOL, N. & JAHREN, J. Density/porosity versus velocity of overconsolidated sands derived from experimental compaction. 75th EAGE Conference & Exhibition incorporating SPE EUROPEC 2013, 2013b.

NPD. 2014. *Barents Sea* [Online]. Available: http://www.npd.no/Global/Norsk/3-Publikasjoner/Rapporter/CO2-samleatlas/Chapter-6.pdf [Accessed August 2016].

NPD. 2014a. *Geology of the Barents Sea* [Online]. Available: http://www.npd.no/en/Publications/Reports/Compiled-CO2-atlas/6-The-Barents-Sea/61-Geology-of-the-Barents-Sea/The-Adventdalen-Group [Accessed September 2016].

NPD. 2014b. *The Kapp Toscana Group - Realgrunnen Subgroup* [Online]. Available: http://www.npd.no/en/Publications/Reports/Compiled-CO2-atlas/6-The-Barents-Sea/61-Geology-of-the-Barents-Sea/The-Kapp-Toscana-Group-Realgrunnen-Subgroup/ [Accessed 2016 September].

NPD. 2016a. *7324/2-1 well page* [Online]. Available: http://factpages.npd.no/ReportServer?/FactPages/PageView/wellbore_exploration&rs:Command=Render&rc:Toolbar=false&rc:Parameters=f&NpdId=7481&IpAddress=129.177.94.75&CultureCode=nb-no [Accessed August 2016].

NPD. 2016b. *7325/1-1* [Online]. Available: http://factpages.npd.no/ReportServer?/FactPages/PageView/wellbore_exploration&rs:Command=Render&rc:Toolbar=false&rc:Parameters=f&NpdId=7501&IpAddress=129.177.94.75&CultureCode=en [Accessed August 2016].

NPD. 2017. *Doubling the resource estimate for the Barents Sea* [Online]. Available: http://www.npd.no/en/news/News/2017/Doubling-the-resource-estimate-for-the-Barents-Sea/ [Accessed May 2017].

NYLAND, B., JENSEN, L., SKAGEN, J., SKARPNES, O. & VORREN, T. 1992. Tertiary uplift and erosion in the Barents Sea: magnitude, timing and consequences. *Structural and tectonic modelling and its application to petroleum geology, Norwegian Petroleum Society (NPF) Special Publication,* 1**,** 153-162.

OHM, S. E., KARLSEN, D. A. & AUSTIN, T. 2008. Geochemically driven exploration models in uplifted areas: Examples from the Norwegian Barents Sea. *AAPG bulletin,* 92**,** 1191-1223.

OSTRANDER, W. 1984. Plane-wave reflection coefficients for gas sands at nonnormal angles of incidence. *Geophysics,* 49**,** 1637-1648.

PALUMBO, F., MAIN, I. G. & ZITO, G. 1999. The thermal evolution of sedimentary basins and its effect on the maturation of hydrocarbons. *Geophysical Journal International,* 139**,** 248-260.

RUTHERFORD, S. R. & WILLIAMS, R. H. 1989. Amplitude-versus-offset variations in gas sands. *Geophysics,* 54**,** 680-688.

SCHOWALTER, T. T. 1979. Mechanics of secondary hydrocarbon migration and entrapment. *AAPG bulletin,* 63**,** 723-760.

SHUEY, R. 1985. A simplification of the Zoeppritz equations. *Geophysics,* 50**,** 609-614.

SKEMPTON, A. 1960. Terzaghi's discovery of effective stress. *From Theory to Practice in Soil Mechanics: Selections from the Writings of Karl Terzaghi***,** 42-53.

SMITH, T. M., SONDERGELD, C. H. & RAI, C. S. 2003. Gassmann fluid substitutions: A tutorial. *GEOPHYSICS,* 68**,** 430-440.

STORVOLL, V., BJRLYKKE, K. & MONDOL, N. H. 2005. Velocity-depth trends in Mesozoic and Cenozoic sediments from the Norwegian Shelf. *AAPG bulletin,* 89**,** 359-381.

VERNIK, L. 2016. Seismic Petrophysics in Quantitative Interpretation. Society of Exploration Geophysicists.

VORREN, T. O., RICHARDSEN, G., KNUTSEN, S.-M. & HENRIKSEN, E. 1991. Cenozoic erosion and sedimentation in the western Barents Sea. *Marine and Petroleum Geology,* 8**,** 317-340.

WALDERHAUG, O. 1994. Temperatures of quartz cementation in Jurassic sandstones from the Norwegian continental shelf--evidence from fluid inclusions. *Journal of Sedimentary Research,* 64.

WALDERHAUG, O. 1996. Kinetic modeling of quartz cementation and porosity loss in deeply buried sandstone reservoirs. *AAPG bulletin,* 80**,** 731-745.

WIGGINS, R., KENNY, G. & MCCLURE, C. 1983. A method for determining and displaying the shear-velocity reflectivities of a geologic formation.

WORDEN, R. & BURLEY, S. 2003. Sandstone diagenesis: the evolution of sand to stone. *Sandstone Diagenesis: Recent and Ancient,* 4**,** 3-44.

YIN, H., NUR, A. & MAVKO, G. Critical porosity—A physical boundary in poroelasticity. International journal of rock mechanics and mining sciences & geomechanics abstracts, 1993. Elsevier, 805-808.

ZHANG, J. J. & BENTLEY, L. R. 2003. Pore geometry and elastic moduli in sandstones. *CREWES Res Rep***,** 1-15.

ZIĘBA, K. J. 2016. Towards understanding the glacial impact on sedimentary basins using numerical methods.

ZOEPPRITZ, K. 1919. Erdbebenwellen vii. *Nachrichten von der Gesellschaft der Wissenschaften zu Göttingen, Mathematisch-Physikalische Klasse,* 1919**,** 57-65.

ØDEGAARD, E. & AVSETH, P. Interpretation of elastic inversion results using rock physics templates. 65th EAGE Conference & Exhibition, 2003.

Appendix

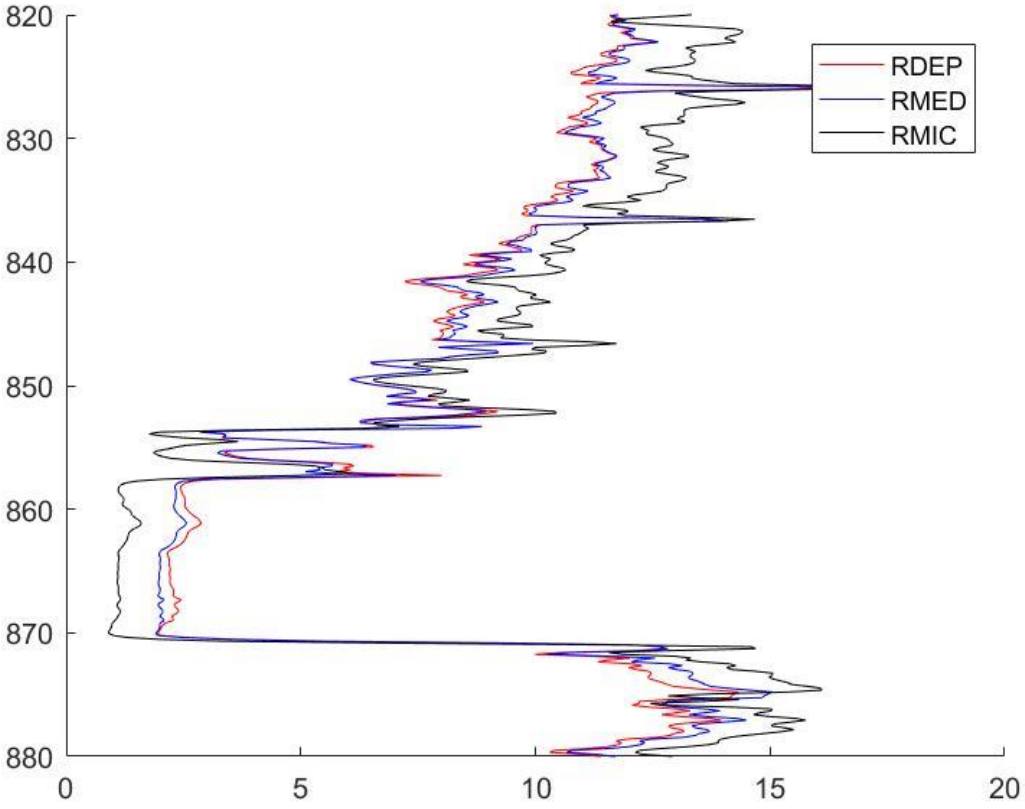

Figure Appendix 1 – The resistivity logs over the Stø Formation in well 7324/2-1. The anomalous low resistivity indicates no hydrocarbons.

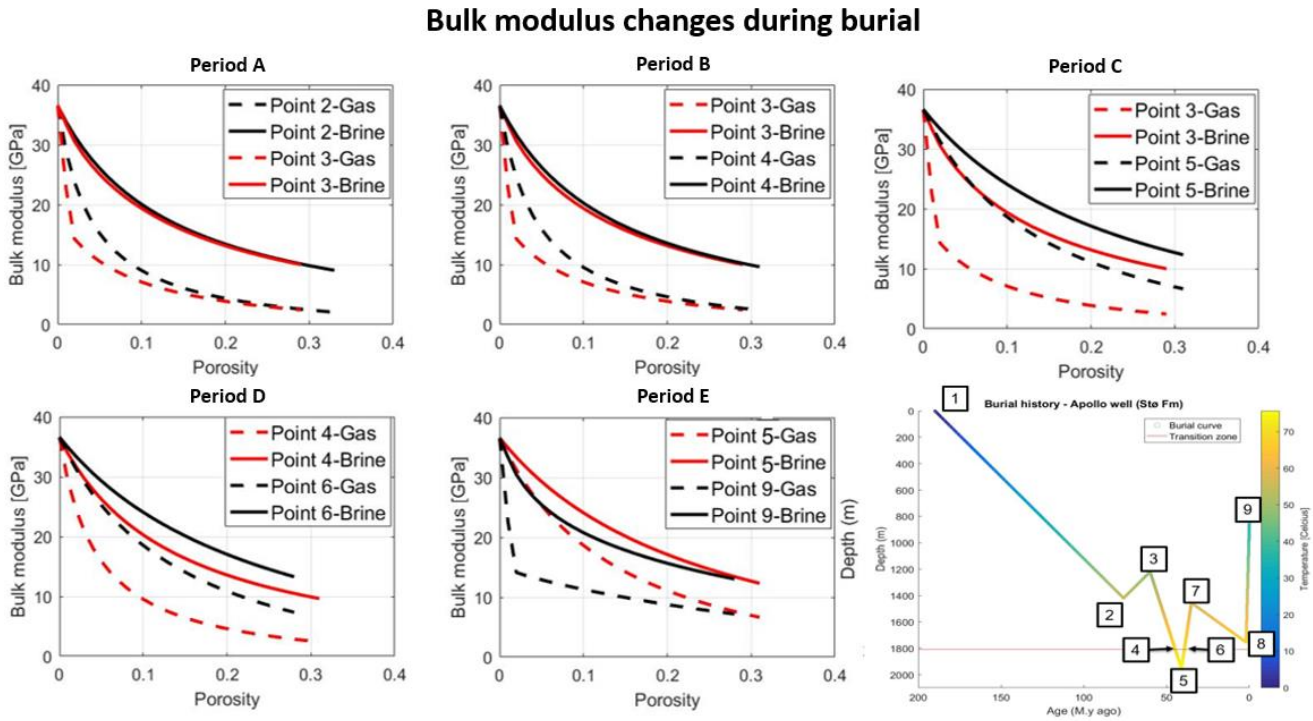

Figure Appendix 2 – Bulk modulus changes for the different periods (Period A, B, C, D and E). The solid lines represent the brine saturated sandstones, and the dashed lines represent the gas saturated sandstones. The burial history is shown in the figure as well, here the color coding represents the temperature.

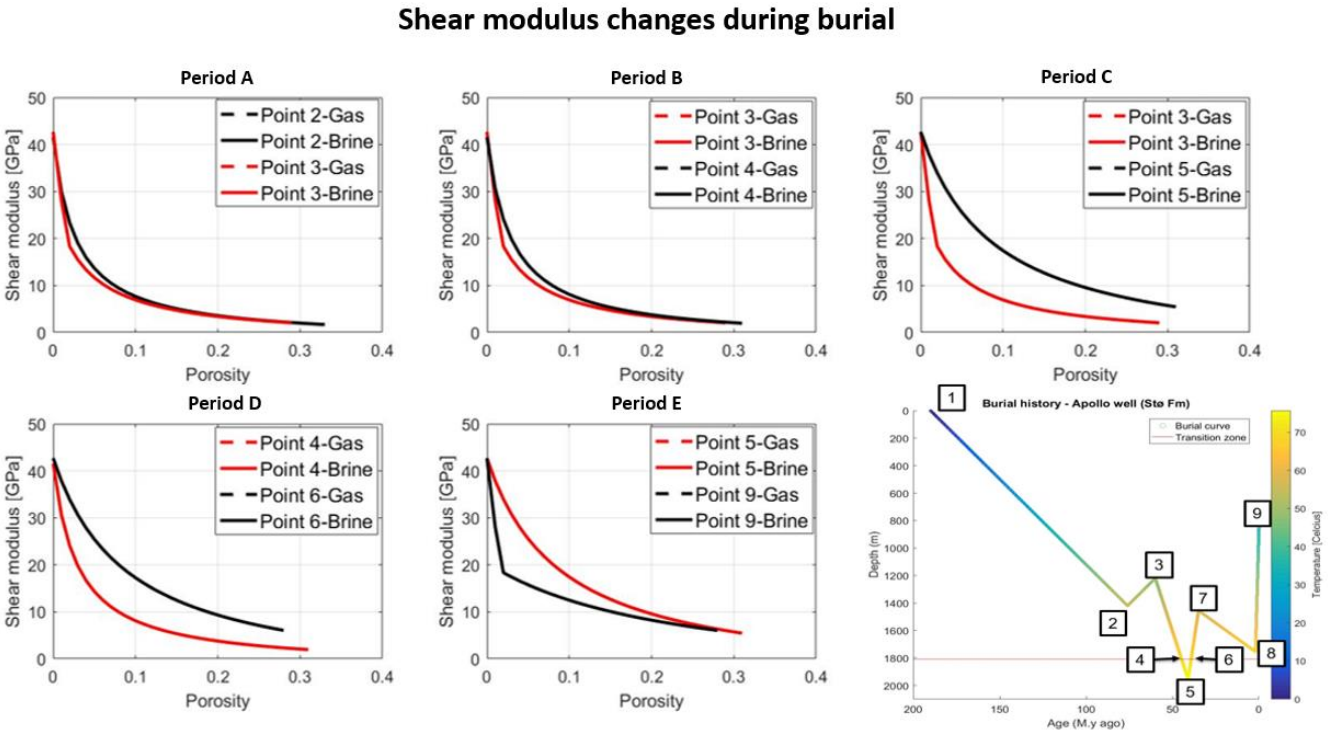

Figure Appendix 3 – Shear modulus changes for the different periods (Period A, B, C, D and E). The solid lines represent the brine saturated sandstones, and the dashed lines represent the gas saturated sandstones. The burial history is shown in the figure as well, here the color coding represents the temperature.